Where the red rise stops: JWST/MIRI reveals a near-infrared turnover in the Little Red Dot Abell 2744-QSO1

E. Iani[1]★, P. Rinaldi[2,3], A. Torralba[1], J. Matthee[1], F. D'Eugenio[4,5], A. Gupta[2,3], S. Mascia[1], C. Di Cesare[1], G. Östlin[6], G. Kotiwale[1], M. Catone[7,8], G. Rodighiero[7,8,9]

[1] *Institute of Science and Technology Austria (ISTA), Am Campus 1, 3400 Klosterneuburg, Austria*
[2] *Department of Astronomy, The University of Texas at Austin, Austin, TX 78712, USA*
[3] *Cosmic Frontier Center, The University of Texas at Austin, Austin, TX 78712, USA*
[4] *Kavli Institute for Cosmology, University of Cambridge, Madingley Road, Cambridge, CB3 0HA, United Kingdom*
[5] *Cavendish Laboratory - Astrophysics Group, University of Cambridge, 19 JJ Thomson Avenue, Cambridge, CB3 0HE, United Kingdom*
[6] *Department of Astronomy, Oskar Klein Centre, Stockholm University, AlbaNova University Center, 10691 Stockholm, Sweden*
[7] *Dipartimento di Fisica e Astronomia "G. Galilei", Università di Padova, Vicolo dell'Osservatorio 3, 35122 Padova, Italy*
[8] *INAF, Osservatorio Astronomico di Padova, Vicolo dell'Osservatorio 5, 35122 Padova, Italy*
[9] *Centro di Ateneo di Studi e Attività spaziali "Giuseppe Colombo" (CISAS), via Venezia 1, 35131 Padova, Italy*

arXiv:2611.09397v1 [astro-ph.GA] 6 Nov 2026

Accepted XXX. Received YYY; in original form ZZZ

ABSTRACT

Little Red Dots (LRDs) are compact sources with a blue rest-frame UV, a steep red optical continuum and, often, broad hydrogen lines. They have been interpreted as dense stellar systems, dust-reddened active galactic nuclei, or black holes embedded in dense, dust-poor gas, scenarios that are hard to tell apart in the rest-frame UV and optical. We present JWST/MIRI F770W and F1000W imaging of the triply lensed Abell 2744-QSO1 at $z = 7.04$, probing rest-frame 0.96 and 1.24μm. QSO1 is unresolved, and its steep optical rise stops near rest-frame 1μm. Up to 1.24μm, a $T \simeq 4450$ K blackbody, or a hotter one reddened by dust, describes the continuum, with no sign of the hot dust seen in most type-1 quasars. Our statistically preferred SED fits produce the red continuum with $(3\text{–}4) \times 10^9$ $M_\odot$ of stars, over 100 times the dynamical limit on the host mass, and are therefore disfavoured. An accretion disc in a dense gas cocoon respects this limit but over-predicts the 1.24μm flux by 5σ. Super-Eddington accretion models with a thermalising envelope reproduce the turnover, but only for a black hole ≈ 2.5 dex less massive than the dynamical estimate. For a dust-reddened accretion disc ($A_V \simeq 2$ mag), dust at ≥ 1200 K can re-emit at most $\simeq 2$ per cent of the absorbed luminosity, and most of it would have to emerge at $\simeq$ 70–600 K, unless the dust covers only a small fraction of the sky. The dynamics favour an accretion-powered source, but our data cannot distinguish dust reddening from processing by dense gas. MIRI imaging at $\gtrsim 18\mu$m could separate these scenarios.

Key words: galaxies: high-redshift – galaxies: active – quasars: supermassive black holes – infrared: galaxies – dust, extinction – gravitational lensing: strong

1 INTRODUCTION

Among the many discoveries enabled by JWST, Little Red Dots (LRDs; Matthee et al. 2024; Kocevski et al. 2023; Labbé et al. 2023) have emerged as one of the most debated populations at intermediate and high redshift (Harikane et al. 2023; Greene et al. 2024; Inayoshi 2025; Übler 2026). They are surprisingly common at $z \sim 5$–7 (Kokorev et al. 2024), and they combine properties with no clear precedent among known galaxies or active galactic nuclei (AGN). LRDs are compact and often unresolved in the rest-frame optical (Kocevski et al. 2025). Their spectral energy distributions (SEDs) are "V-shaped", with a faint blue UV continuum and a steep red optical rise (Furtak et al. 2024; Greene et al. 2024; Kocevski et al. 2025; Setton et al. 2025b). Their broad hydrogen lines, with a full width at half maximum (FWHM) above 1000 km s^{-1}, point to gas moving around a black hole (Matthee et al. 2024; Treiber et al. 2025; Hviding et al. 2025). Other properties, however, are unusual for an AGN. The broad lines often have large Balmer decrements and non-Gaussian, exponential-like wings (Nikopoulos et al. 2026; Rusakov et al. 2026; Torralba et al. 2026a; Chang et al. 2026; Brazzini et al. 2025; Scholtz et al. 2026; Sneppen et al. 2026). Many LRDs also show Balmer absorption on top of the broad emission (Juodžbalis et al. 2024; D'Eugenio et al. 2026a; Matthee et al. 2026; Torralba et al. 2026b), a feature seen in only a handful of quasars (e.g. Hall 2007; Zhang et al. 2015). Most LRDs are X-ray undetected (Ananna et al. 2024; Yue et al. 2024; Kokubo & Harikane 2025), faint in the mid- and far-infrared (Williams et al. 2024; Setton et al. 2025a; Akins et al. 2025; Casey et al. 2025) and show little or no variability (Kokubo & Harikane 2025; Tee et al. 2025; Secunda et al. 2026). Type-1 AGN, instead, are typically bright in X-rays (e.g. Steffen et al.

★ E-mail: edoardo.iani@ist.ac.at

© 2026 The Authors

2006; Just et al. 2007; Lusso & Risaliti 2016), show hot-dust emission in the near- and mid-infrared (e.g. Richards et al. 2006; Mor & Netzer 2012), and vary on time-scales of months to years (e.g. Vanden Berk et al. 2004; MacLeod et al. 2010).

This combination of observed physical properties makes the nature of LRDs hard to establish. Proposed interpretations have ranged from massive compact galaxies (Labbé et al. 2023; Baggen et al. 2024) and composite AGN–host systems (Barro et al. 2024; Greene et al. 2024), to dust-reddened AGN with high accretion rates or a large covering factor (Madau & Maiolino 2026), to accreting black holes embedded in dense, hydrogen-rich gas (Inayoshi & Maiolino 2025; Kido et al. 2025; Naidu et al. 2025; Yanagisawa et al. 2026; de Graaff et al. 2026). More exotic options include supermassive stars, quasi-stars within proto-globular clusters (Nandal & Loeb 2026; Begelman & Dexter 2026; Chisholm et al. 2026; Kokorev et al. 2026).

Whichever of these scenarios is confirmed, it would change our understanding of early black-hole and galaxy growth, and each would change it in a different way. If the light of LRDs were dominated by stars, the stars would have to have formed rapidly in extraordinarily dense systems (Labbé et al. 2023; Baggen et al. 2024). Given the number densities of LRDs, they would also have converted a large fraction of the available baryons into stars by $z \gtrsim 5$, possibly in tension with current cosmological models (e.g. Boylan-Kolchin 2023). If instead LRDs were AGN and their broad lines traced virial motions, they would host black holes of 10^6–10^9 $M_\odot$, up to 1.5–2 dex above the local relation for their host stellar masses. This would challenge even the most extreme models of black-hole growth (Maiolino et al. 2024; Juodžbalis et al. 2026; Pacucci et al. 2023; Harikane et al. 2023). Finally, if they were black holes embedded in dense, dust-poor gas, scattering could broaden the lines and modify their ratios, in which case virial masses would be overestimated thus easing the tension with black-hole growth models (Rusakov et al. 2026; Chang et al. 2026; Ji et al. 2025; Sneppen et al. 2026). At the same time, the dense gas should also produce the observed red optical continuum. This would happen in two ways: it could imprint a Balmer break and absorption on an intrinsically blue AGN continuum (Inayoshi & Maiolino 2025; Naidu et al. 2025; Torralba et al. 2026b; de Graaff et al. 2025b; Matthee et al. 2026); or, if it is optically thick, it could thermalise the accretion luminosity and emit a cool, nearly blackbody spectrum, a "pseudo-photosphere" (Kido et al. 2025; Liu et al. 2026; Begelman & Dexter 2026). Both scenarios would reproduce the V-shaped SEDs and make LRDs an early, possibly short-lived phase of black-hole growth inside dense gas, with black holes less massive than their virial estimates and an emission very different from that of standard AGNs (Inayoshi & Maiolino 2025; Kido et al. 2025; Naidu et al. 2025). The origin, lifetime and geometry of this dense gas, however, remain unclear.

In the rest-frame UV and optical, studies have shown that these scenarios are hard to tell apart, since stars, a dust-reddened AGN and dense gas around the black hole can all reproduce the red optical continuum of LRDs (e.g. Greene et al. 2024; Barro et al. 2024; Inayoshi & Maiolino 2025). This motivates observations in the rest-frame near-infrared. There, the light of a stellar population best traces its mass (e.g. Bell & de Jong 2001). A dust-reddened AGN should show hot dust re-emitting the absorbed luminosity, which in type-1 quasars often produces a rise beyond rest-frame $\approx 1\mu$m well described by a $T \approx 1200$–1300 K blackbody (Barvainis 1987; Richards et al. 2006; Glikman et al. 2006; Temple et al. 2021). A pseudo-photosphere, instead, emits a nearly thermal spectrum with $T_{\rm eff} \approx 4000$–6000 K, which turns over near rest-frame 1μm without hot dust (Kido et al. 2025; Liu et al. 2025, 2026; Begelman & Dexter 2026; Sneppen et al. 2026).

At $z \gtrsim 5$, the rest-frame near-infrared lies beyond observed 5μm and can only be reached with the Mid-Infrared Instrument (MIRI, Rieke et al. 2015; Wright et al. 2023) on board JWST. MIRI observations of LRDs in this regime so far give a mixed picture. Several bright LRDs show weak or absent hot-dust emission (Williams et al. 2024; Setton et al. 2025a), with mid-infrared colours bluer than those of AGN tori (Pérez-González et al. 2024). In contrast, the *Rosetta Stone* (Juodžbalis et al. 2024) and stacks of fainter LRDs (Delvecchio et al. 2025; Pérez-González et al. 2026; Barro et al. 2026) show an excess beyond rest-frame $\approx 2\mu$m, which could trace hot dust. At $z < 1$, LRD analogues selected from the Dark Energy Spectroscopic Instrument (DESI, Levi et al. 2019) survey show blackbody-like continua with $T \approx 2000$–4700 K, peaking at rest-frame 0.6–1.5μm (e.g. Lin et al. 2026; Park et al. 2026), as expected for a pseudo-photosphere. Some of them also show an excess at $\gtrsim 3\mu$m, attributed to warm dust at ≈ 500–700 K (Ashall et al. 2026). Individual faint LRDs at the highest redshifts, where the population is most abundant, remain largely unexplored at these wavelengths.

In this work, we present deep JWST/MIRI F770W and F1000W imaging of Abell 2744-QSO1 (hereafter QSO1), a triply-imaged lensed source at $z = 7.04$ (Section 2) and one of the best-studied LRDs to date (Furtak et al. 2023, 2024, 2025; Ji et al. 2025; Ma et al. 2025; Maiolino et al. 2026; D'Eugenio et al. 2026b; Ji et al. 2026a; Zhang et al. 2026b; Tang et al. 2026). At the redshift of QSO1, these filters probe rest-frame ≈ 0.96 and 1.24μm, the immediate continuation of the observed optical rise. We combine them with the existing UV-to-optical photometry and spectroscopy and with far-infrared and millimetre limits (Section 3) to address three open questions: (i) how the optical rise of QSO1 continues into the near-infrared, (ii) whether the red continuum comes from a massive stellar host or from dense gas around the black hole, and (iii) whether QSO1 shows the hot-dust emission expected for a dust-reddened AGN, and where the luminosity absorbed by dust is re-emitted.

Throughout this paper, we assume a flat Λ-CDM cosmology with $\Omega_{\rm M} = 0.3$, $\Omega_\Lambda = 0.7$, and $H_0 = 70$ km s^{-1} Mpc^{-1}. We adopt AB magnitudes (Oke & Gunn 1983) and a Chabrier (2003) initial mass function (IMF).

2 TARGET

QSO1 is an extremely red, compact source at $z_{\rm spec} = 7.0364$ (Tang et al. 2026), triply imaged by the galaxy cluster Abell 2744 (A2744, $z = 0.308$). Its three images are Ima-A (RA = 3.5798375, Dec = −30.4015733 deg), Ima-B (3.5835458, −30.3966828 deg) and Ima-C (3.5972125, −30.3943442 deg), with magnifications $\mu = 5.4 \pm 1.1$, 7.5 ± 1.5 and 2.7 ± 0.5, respectively (Furtak et al. 2025). Thanks to the lensing magnification, we can study an intrinsically faint source ($M_{\rm UV} \simeq -16.3$) at different moments of its history. In fact, since the light of each image follows a different path through the cluster, it reaches us with a different delay. Image B and image C arrive ≈ 2.3 and ≈ 19 yr after image A (Furtak et al. 2025), spanning up to ≈ 2.4 yr in the rest frame. Between these epochs, the equivalent widths of the broad Hα and Hβ lines have been found to change, revealing variability of the broad-line emission (Furtak et al. 2025).

Several observations point to an accreting black hole, with little room for a host galaxy. QSO1 is unresolved in JWST Near-Infrared Camera (NIRCam; Rieke et al. 2023) imaging, with $r_{\rm e} < 30$ pc (Furtak et al. 2024), and even its rest-frame UV shows AGN features, namely broad Lyα and far-UV Fe II emission (Tang et al. 2026). Its narrow-Hα velocity field indicates Keplerian rotation around a black hole of $\approx 5 \times 10^7$ $M_\odot$ (Juodžbalis et al. 2026), consistent

with the broad-line estimate (Furtak et al. 2024). This leaves at most $\approx 2\times10^7$ $M_\odot$ for the host stars, i.e. $M_{BH}/M_\star > 2$. The narrow-line widths also limit the total dynamical mass to $M_{dyn} < 4\times10^8$ $M_\odot$ (Ji et al. 2025).

Despite these constraints, what produces the continuum of QSO1 is still debated. It shows one of the strongest and smoothest Balmer breaks among LRDs, comparable to that of *the Cliff* (de Graaff et al. 2025b), followed by a steep optical rise. This shape has been reproduced by a massive, heavily attenuated stellar population (Ma et al. 2025), which however conflicts with the dynamical constraints above, by an accretion disc seen through nearly dust-free gas with $n_H \sim 10^{10}$ cm^{-3} and a large population of hydrogen in its $n = 2$ level (Ji et al. 2025; D'Eugenio et al. 2026b; Chang et al. 2026), or by a pseudo-photosphere (e.g. Naidu et al. 2026). If instead the broad Balmer decrement were due to dust, it would imply $A_V \approx 2$–3 mag (Ji et al. 2025; D'Eugenio et al. 2026b). QSO1 is undetected by the Atacama Large Millimeter/submillimeter Array (ALMA; Furtak et al. 2024; Labbe et al. 2025), which constrains only cold dust. It is also undetected in deep *Chandra* observations (Furtak et al. 2024), which at $z = 7$ probe rest-frame energies of $\approx$ 4–56 keV. This X-ray faintness suggests either an intrinsically X-ray-weak source or a large gas column ($N_H \gtrsim 10^{24}$ cm^{-2}; e.g. Lambrides et al. 2026; Maiolino et al. 2025). These constraints come from the rest-frame UV and optical and from far-infrared limits. The continuum beyond rest-frame $\approx 0.6\mu$m, where the scenarios differ, had not been observed before this work.

3 DATA

3.1 Dataset

The core of our dataset is the deep MIRI imaging at 7.7 and 10 μm from the *JWST* Cycle 3 program *MIRI in Clusters* (MIRIC, GO-5578, PIs: Iani & Rinaldi; Iani et al. in prep.), which covers ~5.9 arcmin^2 of the central region of A2744, including all three images of QSO1. The MIRI data were reduced with the same pipeline as in Rinaldi et al. (2025), with further details to be presented in Iani et al. *(in prep.)*.

We complemented the MIRI data with all the available *HST* imaging from the Advanced Camera for Surveys (ACS) and the Wide Field Camera 3 (WFC3), and with *JWST*/NIRCam imaging. We used the fully reduced, public mosaics of the UNCOVER DR3[1] (Bezanson et al. 2024; Suess et al. 2024). These combine the NIRCam imaging from ERS-1324 (GLASS; PI: Treu), GO-2561 (UNCOVER; PIs: Labbé & Bezanson), DD-2767 (PI: Kelly), GO-2883 (MAGNIF; PI: Sun), GO-3516 (ALT; PIs: Naidu & Matthee), GO-3538 (PI: Iani) and GO-4111 (MegaScience; PI: Suess) with the *HST* programs 11689 (PI: Dupke), 13386 (PI: Rodney), 13389 (PI: Siana), 13495 (HFF; PI: Lotz), 15117 (BUFFALO; PI: Steinhardt) and 17231 (PI: Treu).

We also used *JWST*/NIRSpec Multi-Shutter Assembly (MSA) spectroscopy from SPURS (GO-9214, PIs: Mason & Stark), obtained with the three medium-resolution ($R \simeq 1000$) grating/filter combinations G140M/F100LP, G235M/F170LP and G395M/F290LP, which together cover ~1–5.3 μm. We retrieved the reduced spectra (v4) from the DAWN JWST Archive (DJA)[2]. The NIRSpec spectra were reduced via MSAEXP[3] (Brammer 2023) following the data reduction described in Heintz et al. (2024); de Graaff et al. (2025a). All three gratings targeted Ima-B of QSO1.

To potentially constrain the dust emission, we also considered far-infrared and millimetre data. The region covering the three images of QSO1 was observed by *Spitzer*/MIPS at 24 μm and by *Herschel*/PACS (100 and 160 μm) and SPIRE (250, 350 and 500 μm) (Rawle et al. 2014, 2016). These observations reach average 3σ depths of 53 μJy, 2.6, 5.2, 16.8, 19.2 and 19.8 mJy, respectively, where for SPIRE we adopt the confusion-limited depths of Nguyen et al. (2010). QSO1 is not detected in any of these maps. We assumed uniform image-plane noise and adopt the same 3σ limit for each image.

QSO1 is also covered by ALMA Band 6 (1.2 mm) observations from DUALZ+ALCS+ALMA-HFF programs (Fujimoto et al. 2024, 2025; Muñoz Arancibia et al. 2023). We downloaded the fully-reduced ALMA mosaic maps from the UNCOVER webpage[4]. None of the three images is detected, with 3σ upper limits of 94.5, 90.9 and 84.0μJy beam^{-1} for Ima-A, B and C, respectively.

3.2 Photometry extraction

For each of the three multiple images of QSO1, we created $18''\times18''$ cutouts centred on the corresponding coordinates reported in Section 2. Ima-B is significantly contaminated by a foreground object located at a small projected separation from the target ($\approx 1''$). We modelled and removed this contaminating emission through an iterative deconvolution procedure based on the Richardson–Lucy algorithm (Richardson 1972; Lucy 1974), adopting filter-dependent model PSFs. We present more details and examples of the contaminant modelling and subtraction in Appendix A.

We extracted the photometry using SEP (Barbary 2016), a PYTHON implementation of SOURCEXTRACTOR (Bertin & Arnouts 1996). For each filter and multiple image, we adopted the circular aperture that maximised the signal from the target, imposing a minimum radius corresponding to the radius enclosing 70% of the PSF energy. The measured fluxes and their uncertainties were subsequently corrected for the flux falling outside the adopted apertures using the corresponding PSF encircled-energy (EE) curves. For MIRI, we adopted the in-flight EE curves of the JWST calibration reference files (CRDS `apcorr`, context `jwst_1298.pmap`), which include the detector scattering and the extended wings of the PSF. At our aperture radii (0.40–0.56$''$), they enclose 66–72% of the flux, $\approx$ 12% (F770W) and 4–6% (F1000W) less than an STPSF model without detector effects, and agree within 1.5% with the growth curve of a field star (Appendix D).

We estimated the photometric uncertainties empirically by placing 500 apertures, with the same area as that adopted for the target, at random positions within the surrounding sky region. Neighbouring sources were masked before placing the apertures, and the standard deviation of the resulting sky-aperture fluxes was taken as the 1σ uncertainty on our target flux measurement. To additionally account for systematic uncertainties in the absolute flux calibration of the *JWST* data, we adopted a conservative minimum relative uncertainty of 5% in all *JWST* bands.

Finally, we corrected the photometry for Galactic foreground extinction. We adopted $R_V = 3.1$ and the colour excess reported by the IRSA dust maps[5] at the position of QSO1, $E(B-V) = 0.0112\pm0.0004$ (Schlafly & Finkbeiner 2011). The correction in each passband was

[1] https://jwst-uncover.github.io/DR3.html
[2] https://dawn-cph.github.io/dja/
[3] https://github.com/gbrammer/msaexp
[4] https://jwst-uncover.github.io/DR2.html
[5] https://irsa.ipac.caltech.edu/applications/DUST/

calculated using the extinction curve of Gordon et al. (2023), as implemented in the `dust_extinction`[6] Python package (Gordon 2024). The adopted multiplicative corrections, $f_{\rm ext}$, are reported in Table B1, together with the photometry of the three multiple images. The individual-image measurements listed in the table are not corrected for gravitational-lensing magnification.

We then corrected the flux densities of the three multiple images for their magnification factors (Section 2; Furtak et al. 2025), propagating the magnification uncertainties, which include a 20% floor for lensing systematics, into the uncertainty of each band. Although lensing introduces time delays that allow us to observe our target at different intrinsic epochs, the resulting three SEDs show overall consistent colours in their broad-band photometry (Furtak et al. 2025), even in their new MIRI coverage, see Figure B1. The bands that show the largest discrepancies are those affected by strong emission lines. Despite their similar SEDs, Ima-A and Ima-B display approximately wavelength-independent offsets relative to Ima-C, with weighted mean flux-density ratios of $f_{\rm Ima-A}/f_{\rm Ima-C} = 1.87$ and $f_{\rm Ima-B}/f_{\rm Ima-C} = 1.22$. These factors were derived from all detected bands (Appendix B). Excluding the two MIRI bands changes them by $\lesssim 2\%$ (1.86 and 1.25), so the MIRI data do not drive the normalisation. In the medium bands closest to MIRI that are free of strong emission lines (F430M, F460M and F480M), the ratios are 1.92 ± 0.08 and 1.23 ± 0.05 (photometric uncertainties only). We use these values to test for chromatic variability in Section 4.1. These offsets likely reflect residual uncertainties in the relative magnification factors, residual photometric systematics, or a combination of both. We adopted Ima-C as the reference since it has the lowest magnification and is therefore expected to be less sensitive to uncertainties in the lens model. We corrected the de-magnified photometry of Ima-A and Ima-B for the single wavelength-independent multiplicative factor found to match the normalisation of Ima-C. We note that, because the combined SED is tied to the normalisation of Ima-C, the uncertainty on $\mu_{\rm Ima-C}$ acts as a common scaling of all bands, corresponding to a systematic uncertainty of ±0.08 dex on all luminosities and masses derived in this work.

The final photometry of QSO1 was then obtained as the inverse-variance-weighted mean of the three rescaled measurements. To account for any remaining differences between the multiple images, the uncertainty in each band was increased by adding in quadrature a systematic term derived from the inter-image scatter. Further details of this procedure are provided in Appendix B. The resulting combined SED is shown in Figure B1. Following the relative rescaling, the measurements obtained from the three multiple images are mutually consistent within 3σ across the available passbands. The magnification uncertainties included in these errors scale all bands of an image together and do not affect the shape of the SED. For the analysis of the continuum shape (Section 4.2) we therefore combined the images with their photometric uncertainties only, keeping the inter-image systematic term and a 5% calibration floor on the stack. The SED fits use the total uncertainties, which is conservative.

3.3 NIRSpec spectrum

We constructed a continuous NIRSpec spectrum of QSO1 by combining the observations obtained with the G140M/F100LP, G235M/F170LP and G395M/F290LP grating–filter configurations (Section 3.1). The individual spectra were resampled onto a common wavelength grid extending from 0.8 to 5.6 μm, with a sampling of $\Delta\lambda = 0.005$ μm, using the flux-conserving `spectres` algorithm (Carnall 2017). In the wavelength regions covered by more than one configuration, the spectra were combined using inverse-variance weighting. The corresponding wavelength-dependent spectral-resolution curves were derived following the parameterisation of the instrumental line-spread-function (Shajib et al. 2025) and combined using the same weights. We subsequently corrected for the overall normalisation and residual wavelength-dependent path losses by matching the spectrum to the combined imaging photometry derived in Section 3.2. To this end, we calculated synthetic NIRCam photometry by convolving the spectrum with the corresponding filter-transmission curves retrieved from the Spanish Virtual Observatory Filter Profile Service (SVO FPS; Rodrigo et al. 2012; Rodrigo & Solano 2020). The uncertainties in the synthetic photometry were propagated from the errors on the individual spectral elements. For each filter covered by the spectrum, we measured the ratio between the observed and synthetic photometry. Both the imaging and synthetic-photometry uncertainties were included in the corresponding error. We modelled the wavelength dependence of these ratios using a second-order polynomial in logarithmic wavelength and flux-ratio space, and multiplied the spectrum by the resulting correction curve. The uncertainty associated with the path-loss correction was estimated using 1000 Monte Carlo realisations of the photometric-to-synthetic flux-density ratios. This uncertainty was propagated into the final spectral error together with the original uncertainty of the NIRSpec spectrum. The comparison between the combined photometry and the spectrum before and after the path-loss correction is shown in Figure B2, while further details of the procedure are presented in Appendix C.

4 RESULTS

4.1 MIRI morphology and variability

We fitted each image in the contaminant-removed F770W and F1000W mosaics with a point source and with a circular Gaussian convolved with the PSF, accounting for the correlated noise of the drizzled mosaics, with SOCCA (Di Mascolo 2026). To bracket the systematic uncertainty on the PSF, we repeated every fit with two effective PSFs: a model PSF built by resampling per-exposure STPSF models in the same way as the mosaics ("ad-hoc" PSF), and the same PSF broadened to match the core of a field star ("broadened" PSF; Appendices D and E). The broadened PSF is calibrated empirically, but on a star much brighter than QSO1, whose core may be broadened by brightness-dependent detector effects, so the true PSF of QSO1 should lie between the two.

With the broadened PSF, all six fits (three images, two filters) are best described by a point source (Figure 1). With the ad-hoc PSF, some fits prefer a small extension ($\sigma \simeq 0.025$–$0.035''$), but this has nearly the same angular size in all three images, despite their different magnifications, and is smaller than the core excess measured on the field star. It reflects a PSF systematic rather than intrinsic structure, and QSO1 is unresolved in MIRI in all three images. We nevertheless derive the size limits with the ad-hoc PSF, since any mismatch then appears as extension and the limits are conservative. The narrow Hα and Lyα emission of QSO1 extends over a few hundred parsecs (Maiolino et al. 2026; Ji et al. 2026a), but the emission lines contribute only $\approx$ 3–7% of the MIRI flux densities, almost entirely from the broad component (Section 4.2), so an extended narrow-line region is not expected to be detectable in MIRI. Converted to the source plane (Appendix E), the 95% upper

[6] https://dust-extinction.readthedocs.io/en/latest/

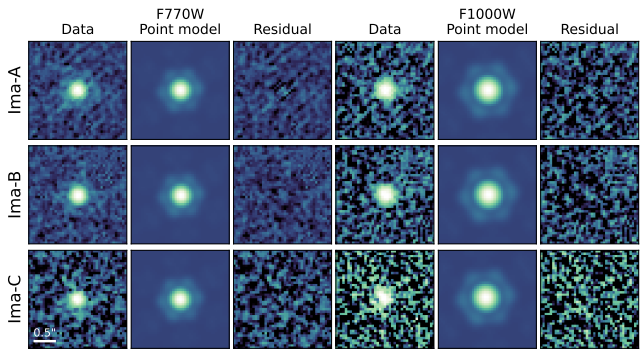


Figure 1. *QSO1 is unresolved in both MIRI bands in all three images.* MIRI morphology of the three images of QSO1 (rows: Ima-A, Ima-B, Ima-C). For F770W and F1000W, the panels show the data, the best-fit point-source model (broadened PSF) and the residuals, on 2.5″ stamps. All images are consistent with a point source. The size limits quoted in the text are derived with the narrower ad-hoc PSF (Appendix E).

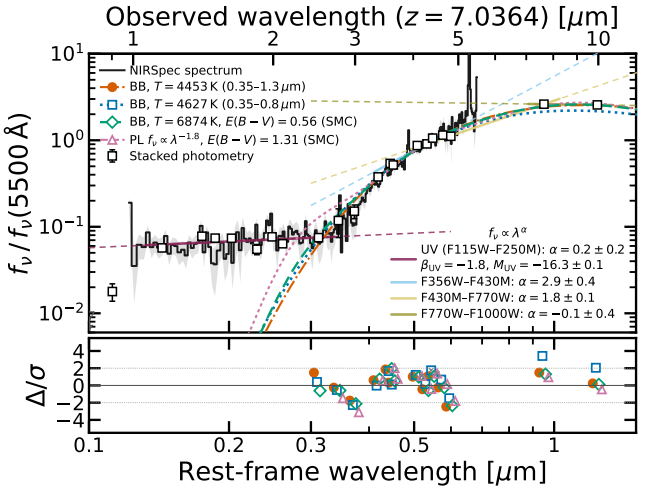


Figure 2. *The steep optical rise of QSO1 flattens between the two MIRI bands, and a single $T \approx 4450$ K blackbody describes the continuum from rest-frame 0.35 to 1.24μm. A hotter blackbody reddened by dust fits equally well.* Rest-frame SED of QSO1 normalised at 5500Å: path-loss-corrected NIRSpec combined spectrum (black) and stacked photometry (white squares). Lines show the blackbodies fitted to the photometry at rest-frame 0.35–1.3μm ($T_{BB} = 4453$ K, including MIRI; purple dash-dotted) and 0.35–0.8μm ($T_{BB} = 4627$ K, optical only; blue dotted), the green dashed line the $T_{BB} = 6874$ K blackbody attenuated by an SMC screen with $E(B-V) = 0.56$ ($A_V \approx 1.5$ mag), and the pink densely dotted line the reddened power law $f_\nu \propto \lambda^{-1.84}$ with $E(B-V) = 1.31$ ($A_V \approx 3.6$ mag; see Section 4.2). Error bars and fits use the photometric uncertainties only (Section 3.2). The coloured segments show the local power-law slopes $f_\nu \propto \lambda^\alpha$ between F356W and F430M, F430M and F770W, and F770W and F1000W, and in the rest-frame UV (F115W–F250M), with their values in the legend. Bottom: residuals of the four continuum models, $(f_{obs} - f_{model})/\sigma$, at the bands between rest-frame 0.3 and 1.3μm, with the markers shown next to each model in the legend (crosses: F410M and F444W, excluded from the fits).

limits on the effective radius in F770W are $r_e < 64$, 70 and 173 pc for Ima-A, B and C. These limits are conservative. The tightest, $r_e <$ 64 pc for Ima-A (< 51 pc dividing by the tangential magnification alone, as in Furtak et al. 2024), is a factor of ≈ 2 weaker than the NIRCam limit of $r_e < 30$ pc, as expected from the broader MIRI PSF.

Ima-A and Ima-C sample epochs ≈ 19 yr apart in the observed frame (≈ 2.4 yr in the rest frame; Section 2). Since the magnification uncertainties are common to all bands of an image, we compared the MIRI image ratios with those of the line-free NIRCam continuum (Section 3.2), using the photometric uncertainties only. For Ima-A, the cleanest image, the ratios relative to Ima-C (1.89 ± 0.13 in F770W and 1.85 ± 0.15 in F1000W) are 0.98 ± 0.08 and 0.96 ± 0.09 times the NIRCam value. For Ima-B they are 12–16% lower, within the scatter of its own NIRCam continuum ratios (1.13–1.43 in F430M–F480M), most likely because of residual contamination from the foreground object (Appendix A). Point-source photometry and different NIRCam reference bands change these ratios by at most $\approx 15\%$, and no combination deviates from the NIRCam value by more than 3σ. We find no evidence for wavelength-dependent variability above $\approx 15\%$, as expected if the optical and near-infrared continua come from the same component. Smaller variations, such as those of a hot-dust component lagging the optical by ~ 0.7 yr, the light-crossing time of the sublimation radius (Section 5.3), cannot be excluded. The broad lines, instead, have been reported to vary. Their equivalent widths differ between the images by up to $\approx 20\%$ (Furtak et al. 2025), and those of Hβ and Hα in Ima-C are about twice those of Ima-A and Ima-B (Ji et al. 2025), consistent with the $\approx 10\%$ lower image ratios we measure in the line-dominated NIRCam bands. Paschen lines twice as strong in Ima-C would raise its MIRI flux densities by only $\approx 3\%$ and $\approx 7\%$ (Section 4.2), within our uncertainties.

4.2 The near-infrared turnover

Between rest-frame 0.44 and 0.53 μm (F356W and F430M), the flux density rises as $f_\nu \propto \lambda^\alpha$ with $\alpha = 2.9 \pm 0.4$, and the rise continues with $\alpha = 1.83 \pm 0.13$ between 0.53 and 0.95 μm (F430M and F770W). Between the two MIRI filters (0.95–1.24 μm), the continuum is instead flat in f_ν, with $\alpha = -0.07 \pm 0.36$. Since $\nu f_\nu \propto \lambda^{\alpha-1}$, νf_ν peaks between rest-frame 0.95 and 1.24μm and declines at longer wavelengths. Both MIRI filters contain hydrogen and helium recombination lines (the Paschen series and He I λ10830 in F770W, Paβ in F1000W). Scaling the broad and narrow Hα fluxes of D'Eugenio et al. (2026b) with Case-B line ratios and the broad-line attenuation (Appendix F), lines contribute at most $\approx 3\%$ and $\approx 7\%$ of the F770W and F1000W flux densities, so the flattening is a property of the continuum.

A single blackbody fitted to the combined photometry at rest-frame wavelengths longer than 0.35 μm (excluding F410M and F444W, which are contaminated by Hβ) has $T_{BB} = 4450 \pm 60$ K and $\chi^2_{red} = \chi^2_{min}/(N_{bands} - N_{par}) = 2.2$ (nine filters, two free parameters), and reproduces both MIRI points within 1.3σ (Figure 2). The largest residuals are in two NIRCam bands (F356W and F480M, ≈ 2–2.5σ), not in MIRI. Fitting only the rest-frame optical filters (F300M to F480M) gives $T_{BB} = 4630 \pm 110$ K, which under-predicts the F770W and F1000W flux densities by 18% and 15% (3.3σ and 2.0σ), whereas a power law fitted to the same filters ($\alpha = 3.3$) over-predicts them by factors of 2.2 and 5.3. The MIRI bands therefore trace the turnover of the same thermal component that produces the red optical continuum, and no additional component is needed up to 1.24μm. The blackbody temperature is, however, degenerate with dust attenuation: a hotter, reddened blackbody ($T_{BB} = 6874$ K

with $A_V \simeq 1.5$ mag, $\chi^2_{\rm red} = 2.4$) describes the data equally well (Appendix F).

Figure 3 compares QSO1 with empirical templates of type-1 quasars and LRDs, all normalised at rest-frame 5500Å. Relative to the quasar templates (Vanden Berk et al. 2001; Glikman et al. 2006; Kim et al. 2026; Bosman et al. 2025), QSO1 is 10–20 times fainter in the UV, but its steep optical rise brings it close to the quasar composite at $\approx 1\mu$m. Only at 1.24μm does the composite become brighter, as the hot-dust emission of type-1 quasars sets in. Among LRDs, the stacks of Delvecchio et al. (2025) and Pérez-González et al. (2026) and the *Rosetta Stone* (Juodžbalis et al. 2024) closely reproduce the optical rise and the MIRI photometry of QSO1, although they are brighter in the UV. The closest match over the whole range is JADES-1180-12402 ($z = 3.19$; Williams et al. 2024; Setton et al. 2025a). With $L_\nu(5100\ \text{Å})/L_\nu(2500\ \text{Å}) \approx 9$–$11$, QSO1 falls among the extreme LRDs (xLRDs, with a ratio above 6.3) of Pérez-González et al. (2026), whose stack agrees well with it. Up to 1.24μm, QSO1 is therefore a typical LRD with the UV continuum of the most extreme ones. The local LRD *the Egg* ($z = 0.10$; Lin et al. 2025; Ji et al. 2026b) and *the Cliff* ($z = 3.55$; de Graaff et al. 2025b), whose extreme Balmer break is due to absorption in dense gas, have a similar optical rise and bracket QSO1 at 0.95–1.24μm, with *the Egg* slightly above and *the Cliff* slightly below. Beyond 1.24μm, where our data stop, LRDs diverge. The LRD stacks keep rising, whereas the *the Egg* and *the Cliff* stay nearly flat in f_ν up to rest-frame ≈ 3–4μm. *The Egg* rises again only at longer wavelengths, where its WISE photometry traces warm dust, and *the Cliff* shows no evidence of hot dust (de Graaff et al. 2025b).

4.3 What produces the red continuum

We compared the SED with three sets of models of increasing physical detail: the continuum models of Ma et al. (2025) and the accretion-flow envelopes of Liu et al. (2025) (Section 4.3.1), and our own models with the nebular emission of dense gas, fitted to the photometry and the spectrum (Section 4.3.2).

4.3.1 Continuum models

Ma et al. (2025) modelled the rest-frame UV–optical continuum of QSO1 (up to 0.66μm) with an attenuated, ~ 100 Myr-old stellar population (galaxy-only), a reddened quasar continuum with a small scattered fraction (AGN-only) and a combination of the two (AGN+galaxy). All three described the data comparably well, but the solutions with a stellar component require a very steep attenuation curve (Ji et al. 2025). We first rebuilt their published best fits and extended them to the MIRI bands without refitting (Appendix H, Figure H1, Table H1). We found that those with a stellar component over-predict F1000W by 48–60% (79% with the hot dust of the quasar template). We then refitted the same families to our photometry, with and without MIRI (Table H2, Figure 4).

Constrained by NIRCam alone, the models over-predict the MIRI flux densities by 27–76% when a stellar component is present and by 18–43% for the AGN-only model, over the whole posterior volume, because the attenuated continuum keeps rising beyond 1μm. With MIRI, the galaxy-only model needs less attenuation than when fitted to NIRCam alone, and a surviving stellar mass of $\log_{10}(M_\star\ [\mathrm{M}_\odot]) = 9.33^{+0.10}_{-0.09}$, still in tension with the upper limit on the host stellar mass (Section 2). The AGN+galaxy posterior splits into two modes, one close to this galaxy-only solution and one dominated by the reddened AGN with a minor stellar component ($\log_{10}(M_\star\ [\mathrm{M}_\odot]) \approx 7.5$–$8$). The galaxy-only and AGN+galaxy models fit the data equally well ($\chi^2_{\rm red} = 0.94$ and 1.20) and have indistinguishable Bayesian evidence[7] ($\Delta\ln(\mathcal{Z}) = -0.7$ for AGN+galaxy relative to galaxy-only). The AGN-only model is disfavoured ($\Delta\ln(\mathcal{Z}) = -5.4$, $\chi^2_{\rm red} = 1.70$), and adding the hot-dust component of the Temple et al. (2021) quasar template disfavours it further ($\Delta\ln(\mathcal{Z}) = -19.5$). In the AGN+galaxy model the hot dust instead suppresses the AGN, and the fit reverts to the galaxy-only solution (Appendix H).

The spherical accretion-flow models of Liu et al. (2025), in which the emission of an accreting black hole thermalises in a dense envelope, behave differently (Appendix H1). With a power law added for the UV continuum, a single envelope spectrum reproduces the photometry from the Balmer break to F1000W ($\chi^2 = 14.3$ in the nine bands of Section 4.2, against 15.4 for the 4450 K blackbody), with both MIRI bands within 1σ (Figure 5), whereas the fit without MIRI under-predicts them by 3–4σ. In this picture the Balmer break, the turnover and the flat MIRI bands arise in the same thermalised gas, without hot dust or an evolved population. Two discrepancies remain. The model break is a sharp step at 3646 Å, whereas the observed one is smoother, as expected if bulk or turbulent motions broaden the Balmer edge (Ji et al. 2025; Naidu et al. 2025) or if the photosphere spans a range of densities and temperatures. The solution that matches the observed luminosity without rescaling has $L \approx 2\times10^{43}$ erg s^{-1}, i.e. $\log(M_{\rm BH}/\mathrm{M}_\odot) \approx 5.2$, and at the dynamical black-hole mass (Juodžbalis et al. 2026) these near-Eddington models would over-predict the observed luminosity by ≈ 2.5 dex (Section 5.1).

4.3.2 SED modelling with dense gas

Except for the envelopes, the models of Section 4.3.1 include neither emission lines nor the dense gas that may shape the Balmer break and the broad lines of QSO1 (Ji et al. 2025) and of LRDs in general (Sun et al. 2026). We therefore fitted the NIRSpec spectrum, emission lines included, and the photometry jointly with a Bayesian forward-modelling code based on the nested sampler Nautilus (Lange 2023), using models with the nebular emission of stellar- and AGN-ionised gas over a wide range of densities (Appendix I). The spectrum targets Ima-B and is flux-calibrated to the stacked photometry (Section 3.3), so the two data sets are not fully independent and its line equivalent widths may differ from those of the stack (Furtak et al. 2025).

All families contain bpass binary stellar populations (Eldridge et al. 2017; Stanway & Eldridge 2018), with a Chabrier (2003)-like IMF extending to 300 $\mathrm{M}_\odot$, metallicities of 0.05% (`zem5`), 0.5% (`zem4`), 5% (`z001`) and 10% $Z_\odot$ (`z002`) and nebular emission computed with Cloudy (v25; Gunasekera et al. 2025). We considered three classes of models for the UV and red optical continuum: (i) two stellar populations in gas of ordinary density ($n_{\rm H} < 10^{6.0}$ cm^{-3}); (ii) an ordinary-density population plus a population coupled to dense photoionised gas ($n_{\rm H} = 10^{6.5-12.0}$ cm^{-3}), with a free covering fraction and lines with their own velocity dispersion; (iii) an ordinary-density population plus an accretion disc embedded in a dense ($n_{\rm H} = 10^{8.0-12.0}$ cm^{-3}), dust-free cocoon[8], with a free covering fraction C (Appendix I3). The UV and optical components were

[7] The Bayesian evidence, $\mathcal{Z} = \int \mathcal{L}(\theta)\,\pi(\theta)\,\mathrm{d}\theta$, is the likelihood $\mathcal{L}$ averaged over the prior π, and therefore penalises models with more parameters or wider priors. Differences $|\Delta\ln(\mathcal{Z})| > 5$ are commonly regarded as strong evidence (Trotta 2008).

[8] The Cloudy cocoon is an approximation in the regime favoured by the fits, because Cloudy solves the gas structure only along the radial direction of a spherically symmetric shell and does not follow scattering as a transfer process (Appendix I3).

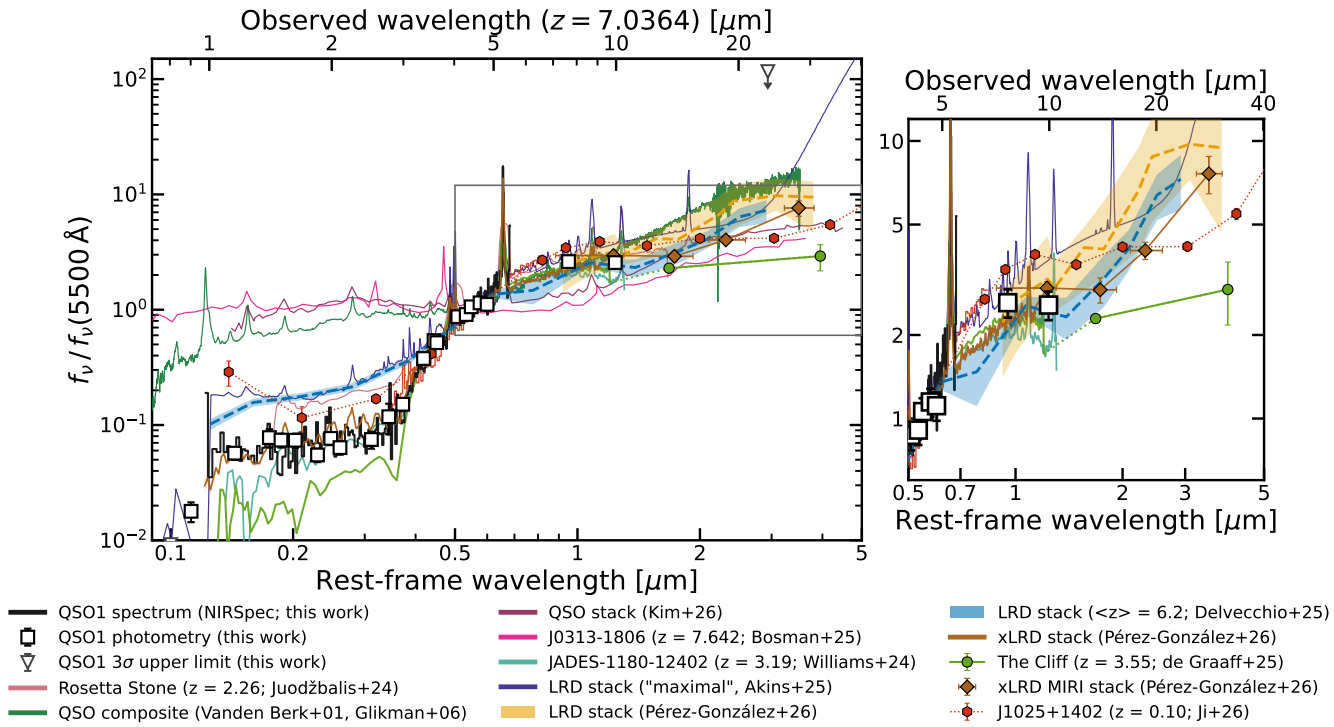


Figure 3. *Up to rest-frame 1.24μm the SED of QSO1 resembles those of other LRDs, and lacks the hot-dust rise of type-1 quasars. Beyond this wavelength, where our data stop, LRDs diverge.* Rest-frame SED of QSO1 (stacked photometry: white squares and 3σ upper limits; path-loss-corrected NIRSpec spectrum: black) compared with type-1 quasar templates (Vanden Berk et al. 2001; Glikman et al. 2006; Kim et al. 2026), the $z \approx 7.6$ quasar J0313−1806 (Bosman et al. 2025), the LRDs GN-28074 (the *Rosetta Stone*; Juodžbalis et al. 2024) and JADES-1180-12402 (Williams et al. 2024; Setton et al. 2025a), *the Cliff* (RUBIES-UDS-154183, $z = 3.55$; de Graaff et al. 2025b; PRISM spectrum and NIRCam+MIRI photometry, circles), the local LRD J1025+1402 (*the Egg*, $z = 0.10$; Lin et al. 2025; Ji et al. 2026b), the "maximal" LRD template of Akins et al. (2025), the LRD stacks of Delvecchio et al. (2025) and Pérez-González et al. (2026) (shaded: their uncertainties), and the stack of extreme LRDs (xLRDs) of Pérez-González et al. (2026) with its MIRI photometric stack (dark orange line and diamonds). All curves are normalised to their flux density at rest-frame 5500Å. The right panel zooms on the rest-frame 0.5–5μm range (grey box in the left panel) and shows only QSO1, the LRD and xLRD stacks of Pérez-González et al. (2026), the Cliff, the stacks of Delvecchio et al. (2025) and Akins et al. (2025), JADES-1180-12402 and *the Egg*. The QSO1 spectrum and photometry are from this work. The spectra of the *Rosetta Stone* and JADES-1180-12402 are smoothed for readability.

attenuated either independently or by a single shared foreground screen with a Noll et al. (2009) law, and all families include dust emission tied to the absorbed luminosity (Section 5.3). Each family was fitted separately at each metallicity and compared through its Bayesian evidence (Tables I2 and I3). We also repeated class (iii) with the formed stellar mass limited to $\log_{10}(M_\star\ [\mathrm{M}_\odot]) \leq 7.5$, i.e. a surviving mass of $\approx 2 \times 10^7\ \mathrm{M}_\odot$, the upper limit on the host stellar mass derived from the dynamics by Juodžbalis et al. (2026) ("stellar-mass limit" in the following).

Figure 6 shows the highest-evidence maximum-likelihood solution of each class, Table 1 their properties and Figure I2 their posteriors. A single foreground screen cannot reproduce the V-shaped SED: with a shared screen, the dense-gas stellar solutions lose $\Delta \ln(\mathcal{Z}) \simeq 81$–$274$ and the cocoon solutions $\simeq 94$–125, so the UV and the red continuum must come from regions with different effective attenuation.

Two ordinary-density stellar populations. A young, almost unobscured population produces the UV and a massive, attenuated ~ 20 Myr population the red continuum (formed $\log_{10}(M_\star\ [\mathrm{M}_\odot]) \simeq 9.61$). This is the analogue of the galaxy-only model of Ma et al. (2025), with a similar mass and the same steepest attenuation curve allowed ($\delta \simeq -0.95$), but a younger age (~ 20 against ~ 100 Myr), favoured by the nebular emission and the Balmer region of the spectrum. It has by far the lowest evidence of the four.

Stellar populations with dense gas. Coupling the red-continuum population to dense photoionised gas significantly improves the Bayesian evidence ($\Delta \ln(\mathcal{Z}) \simeq 127$). A ~ 16 Myr population with $\log_{10}(M_\star\ [\mathrm{M}_\odot]) \simeq 9.62$ produces the red continuum, ≈ 140–200 times the upper limit on the host stellar mass, and its lines need $\sigma_v \simeq 800$ km s^{-1}, difficult to reconcile with a stellar H II region.

Accretion disc in a dense cocoon. The highest-evidence run of all does not use the disc for the red continuum. The disc, seen directly and through a cocoon with $C \simeq 0.26$, produces the UV, while a ~ 20 Myr stellar population with $\log_{10}(M_\star\ [\mathrm{M}_\odot]) \simeq 9.57$ produces 75–85% of the light at rest-frame 0.5–1.2μm, with the same tension with the dynamical mass.

Cocoon with the stellar-mass limit. With the stellar-mass limit the roles are reversed. A young population ($\log_{10}(M_\star\ [\mathrm{M}_\odot]) \simeq 6.96$) produces the UV, and the disc ($L_{\mathrm{AGN}} \approx 2.4 \times 10^{44}$ erg s^{-1}) and the cocoon ($C \simeq 0.22$, $n_{\mathrm{H}} = 10^{11}$ cm^{-3}, $U = 10^{-3}$ and $N_{\mathrm{H}} = 10^{25.5}$ cm^{-2}, the largest column of the grid) more than 90% of the light beyond rest-frame 0.5μm, behind a screen with $A_V \simeq 1.3$ mag and the steepest attenuation slope allowed. The same solution is found at all four metallicities. Its continuum keeps rising beyond rest-frame 1μm and over-predicts F1000W by 5σ, whereas the solutions with a massive stellar population are within 1σ (stellar models) and 2.3σ (unconstrained cocoon).

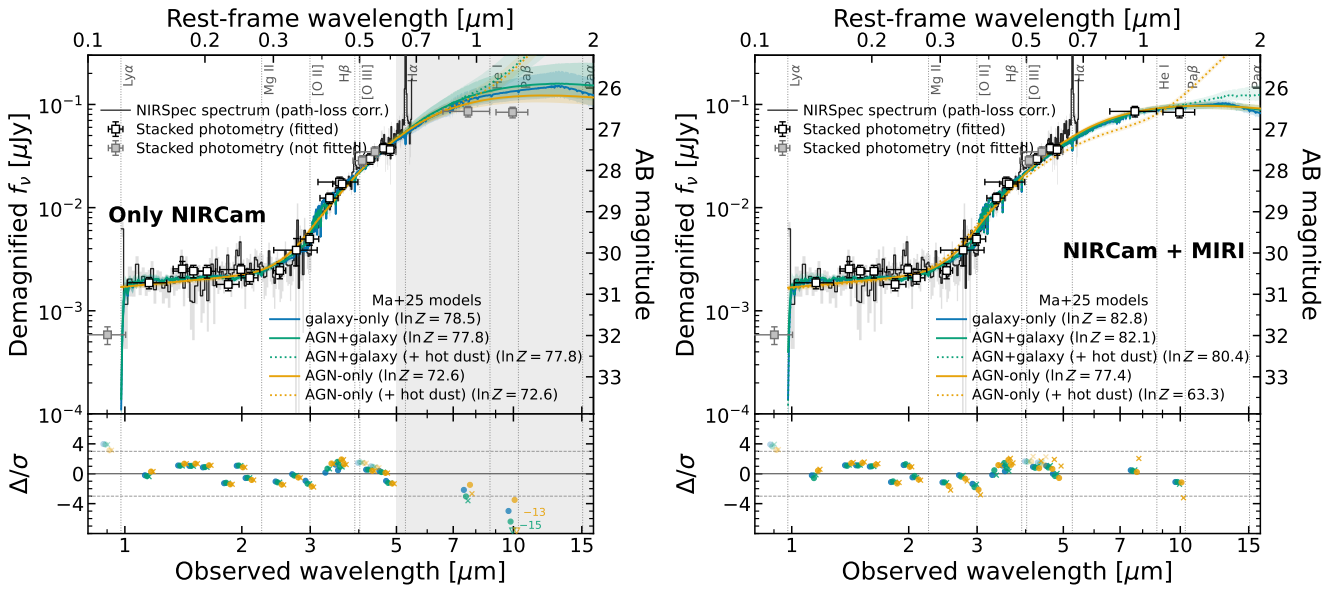


Figure 4. *MIRI reveals that the continuum models of Ma et al. (2025), constrained by NIRCam alone, over-predict the near-infrared, and that quasar-like hot dust is disfavoured.* Posterior fits of the model families of Ma et al. (2025) to the stacked photometry of QSO1, fitted to the NIRCam bands only (left) and to NIRCam and MIRI (right). White squares are the fitted bands. Grey squares are bands not used in the fit (F090W, affected by the Lyα break, and F410M and F444W, dominated by Hβ). Horizontal bars show the filter coverage. In the left panel, the grey shaded region marks the MIRI range ($\lambda_{\rm obs} > 5\mu$m), which is not fitted. The NIRSpec spectrum (path-loss corrected, black) is shown for reference only and is not fitted. Coloured lines and shaded regions show the posterior median and 16th–84th percentile range of each model family. Dotted lines include the hot-dust component of the Temple et al. (2021) quasar template. The log-evidence of each fit is given in the legend. Bottom panel: residuals, $(f_{\rm obs} - f_{\rm model})/\sigma$, of the synthetic photometry of each model.

Within the model families explored, the spectrum requires a dense, strongly reprocessing component, in line with the broad Balmer lines with a large decrement (D'Eugenio et al. 2026b) and the broad Lyα and far-UV Fe II emission of QSO1 (Tang et al. 2026). The highest-evidence solutions produce the red continuum with $\approx 4\times10^9$ M$_\odot$ of stars, two orders of magnitude above the stellar-mass limit, and the solution within this limit has an evidence lower by $\Delta\ln(\mathcal{Z}) \simeq 20$–$33$. We regard this difference as indicative given the systematics of our modelling (Appendix I), but it does not depend on how the images are combined (it holds for the photometry of each lensed image, with $\Delta\chi^2 = 31$–107; Appendix I5) or on metallicity (Table I3).

Two test models clarify the role of the stars (Appendix I4). In the first, there is no stellar population, and the disc and cocoon must also produce the UV. This model misses the Balmer break by $\approx 3\sigma$ and over-predicts F1000W by $\approx 5\sigma$ (Figure I1). In the second, the stars are unattenuated and their mass is not limited. They then produce only the UV, and the fit converges to the solution with the stellar-mass limit. Within our grid, a separate UV component seems to be required, and the massive solutions rely on heavily attenuated stars. The UV may nevertheless be partly AGN light, as suggested by its far-UV Fe II emission (Tang et al. 2026), and radiative-transfer effects not included in our grid could produce the blue UV and the red continuum in the same gas (e.g. Mascia et al. 2026).

The SED alone thus prefers a massive stellar population, whereas the dynamics, the broad lines and the UV features point to an accretion-powered source in dense gas.

5 DISCUSSION

5.1 A pseudo-photosphere?

The steep optical rise of QSO1 does not continue into the near-infrared, and its SED up to 1.24μm is typical of LRDs (Section 4.2). With $\nu L_\nu(1\ \mu{\rm m}) \approx 1.8\times10^{43}$ erg s^{-1} and $M_{\rm UV} \simeq -16.3$, QSO1 extends this shape to one of the faintest and most distant LRDs observed at these wavelengths.

Two kinds of source can produce this shape. In the first, the engine (e.g. an accreting black hole) is enshrouded in dense gas that is optically thick enough to thermalise its emission, so that it radiates from a pseudo-photosphere with $T_{\rm eff} \approx 4000$–6000 K, close to a blackbody (Liu et al. 2026). A single component then produces both the optical rise and the turnover, without the need of dust. Thermalisation is what makes this model work. In fact, gas that only absorbs the disc light can produce a Balmer break and can partially redden the optical continuum (Inayoshi & Maiolino 2025), but it cannot produce the steep optical rise and the turnover observed. In a pseudo-photosphere, these come from the thermal emission of the gas itself. Among our models, only the accretion-flow envelopes of Liu et al. (2025) are of this kind (Section 4.3.1). However, while these envelope models reproduce the shape of the turnover, their luminosity is in tension with the dynamical black-hole mass (Section 4.3.1). These models, in fact, are powered by supercritical accretion, and photon trapping and outflows regulate their emergent luminosity to $\sim$ 1–10 $L_{\rm Edd}$ (Kido et al. 2025; Liu et al. 2025; Jiang et al. 2014). For the dynamical mass, $\log(M_{\rm BH}/{\rm M}_\odot) = 7.7\pm0.3$ (Juodžbalis et al. 2026), $L_{\rm Edd} \approx 6\times10^{45}$ erg s^{-1} (3–12 $\times10^{45}$ erg s^{-1}). QSO1 is far below this value, whichever bolometric luminosity is adopted. Integrating its observed SED gives $L_{\rm bol} \approx 3\times10^{43}$ erg s^{-1} (Section 5.4), i.e. $\lambda_{\rm Edd} \approx 0.005$. The type-1 bolometric correction applied to Hα gives $\approx 2\times10^{44}$ erg s^{-1}, i.e. $\lambda_{\rm Edd} \approx 0.03$. Even the intrinsic luminosity

Table 1. Physical properties of the four representative solutions, each at the metallicity of its highest evidence (Figure 6): posterior medians with 16th–84th percentile ranges. Ages are $\log_{10}(t\ [\mathrm{yr}])$, stellar masses are formed masses $\log_{10}(M_\star\ [\mathrm{M}_\odot])$, de-magnified. The surviving masses are at most 0.15 dex lower at these ages. "UV" and "opt." denote the stellar populations dominating the rest-frame UV and optical continua. δ is the slope offset of the attenuation curve (prior $[-1, 0.4]$). $T_{\mathrm{dust},0}$ is the intrinsic dust temperature, before CMB heating. C is the covering fraction of the photoionised gas of each stellar population, or of the cocoon.

	Two ordinary-density stellar populations `zem4`	Stellar populations with dense gas `zem5`	Accretion disc in a dense cocoon `zem4`	Cocoon with the stellar-mass limit `zem4`
$\ln(\mathcal{Z})$ ($\Delta\ln(\mathcal{Z})$)	3747.4 (−139.8)	3874.5 (−12.7)	3887.2 (0)	3854.4 (−32.8)
Optical continuum from	stars	stars (dense gas)	stars	disc + cocoon
UV-emitting stellar population				
Age	$6.8^{+0.2}_{-0.1}$	$6.8^{+0.1}_{-0.2}$	–	$6.9^{+0.1}_{-0.2}$
$\log_{10} M_\star$	$6.69^{+0.19}_{-0.22}$	$6.48^{+0.19}_{-0.18}$	–	$6.96^{+0.32}_{-0.35}$
$E(B-V)$	$0.022^{+0.003}_{-0.004}$	$0.019^{+0.004}_{-0.003}$	–	$0.25^{+0.12}_{-0.13}$
C	$0.54^{+0.27}_{-0.16}$	$0.44^{+0.23}_{-0.15}$	–	$0.63^{+0.26}_{-0.25}$
$\log_{10}(n_{\mathrm{H}}\ [\mathrm{cm}^{-3}])$, $\log_{10} U$	5.5, −2.5	6.0, −1.0	–	6.0, −1.0
Optical-continuum stellar population				
Age	$7.3^{+0.1}_{-0.1}$	7.2	$7.3^{+0.1}_{-0.1}$	–
$\log_{10} M_\star$	$9.61^{+0.08}_{-0.09}$	$9.62^{+0.03}_{-0.03}$	$9.57^{+0.10}_{-0.07}$	–
$E(B-V)$	$0.663^{+0.025}_{-0.019}$	$0.650^{+0.018}_{-0.016}$	$0.694^{+0.017}_{-0.016}$	–
C	$0.18^{+0.12}_{-0.06}$	$0.38^{+0.03}_{-0.02}$	$0.49^{+0.29}_{-0.23}$	–
$\log_{10}(n_{\mathrm{H}}\ [\mathrm{cm}^{-3}])$, $\log_{10} U$	6.0, −1.5	7.5, −3.0	3.0, −1.5	–
σ_v of dense-gas lines [km s^{-1}]	–	798^{+53}_{-51}	–	–
Accretion disc and cocoon				
$\log_{10}(L_{\mathrm{AGN}}\ [L_\odot])$	–	–	$9.97^{+0.21}_{-0.16}$	$10.79^{+0.04}_{-0.04}$
C	–	–	$0.26^{+0.04}_{-0.03}$	$0.22^{+0.03}_{-0.02}$
$\log_{10}(n_{\mathrm{H}}\ [\mathrm{cm}^{-3}])$, $\log_{10} U$	–	–	9.0, −2.0	11.0, −3.0
$\log_{10}(N_{\mathrm{H}}\ [\mathrm{cm}^{-2}])$	–	–	25.0	25.5
σ_v of cocoon lines [km s^{-1}]	–	–	855^{+74}_{-67}	906^{+64}_{-64}
$E(B-V)$	–	–	$0.13^{+0.11}_{-0.07}$	$0.315^{+0.012}_{-0.012}$
δ	–	–	$0.07^{+0.21}_{-0.38}$	$-0.985^{+0.023}_{-0.011}$
$\log_{10}(M_{\star,\mathrm{tot}}\ [\mathrm{M}_\odot])$	9.61	9.62	9.57	6.96
δ (stellar)	$-0.95^{+0.06}_{-0.04}$	$-0.95^{+0.04}_{-0.03}$	$-0.98^{+0.03}_{-0.02}$	$0.30^{+0.07}_{-0.21}$
$T_{\mathrm{dust},0}$ [K]	228^{+168}_{-104}	234^{+162}_{-95}	226^{+175}_{-103}	171^{+193}_{-101}
$\log_{10}(L_{\mathrm{dust}}\ [L_\odot])$	$11.50^{+0.26}_{-0.29}$	$11.62^{+0.23}_{-0.24}$	$11.44^{+0.29}_{-0.28}$	$10.29^{+0.29}_{-0.26}$

of a reddened accretion disc, $(0.4\text{–}1.2) \times 10^{45}$ erg s^{-1}, would give only $\lambda_{\mathrm{Edd}} \approx 0.06\text{–}0.2$. This tension would only ease if the black-hole mass were overestimated, the bolometric luminosity underestimated, or the emission strongly anisotropic, as expected for super-Eddington flows (Jiang et al. 2014; Pacucci & Narayan 2024).

In the second kind, a hotter source is reddened by dust, and the continuum turns over where the attenuation becomes small. The hotter the source, the more luminosity the dust must absorb. A 6900 K blackbody behind $A_V \approx 1.5$ mag has $L_{\mathrm{bol}} \approx 8{\times}10^{43}$ erg s^{-1}, of which the dust absorbs $L_{\mathrm{abs}} \approx 5 \times 10^{43}$ erg s^{-1}. A 3×10^4 K blackbody behind $A_V \approx 3.3$ mag would instead have $L_{\mathrm{bol}} \approx 5 \times 10^{45}$ erg s^{-1}, nearly all of it absorbed. This is close to the Eddington luminosity for the dynamical black-hole mass. All our other models are of this kind: the reddened accretion disc ($A_V \approx 2.2$ mag), the reddened blackbody ($A_V \approx 1.5$ mag), the massive stellar populations ($A_V \approx 2.6\text{–}2.8$ mag) and, despite its dense gas envelope, the cocoon with the stellar-mass limit ($A_V \approx 1.3$ mag, Section 4.3). In fact, while this cocoon reproduces the UV, the Balmer break and the broad lines with a black hole in dense gas, it does not reproduce the turnover, because its gas does not thermalise. The gas is optically thick in the Balmer continuum ($\tau \approx 30$ below 3646 Å), which produces the break, but only marginally in the Paschen continuum ($\tau \approx 2$ below 8204 Å) and nearly transparent beyond. Its near-infrared continuum is therefore the transmitted disc light and the nebular emission of the gas, roughly flat in f_ν. The steep rise comes instead from its dust screen and the directly seen disc, which keep rising beyond 1μm and over-predict F1000W. The same mostly neutral gas also scatters little. In dense-gas models of LRDs, scattering by free electrons has been proposed to produce the broad wings of the Balmer lines (e.g. Chang et al. 2026). In our cocoon, however, the fully ionised layer is thin and most free electrons come from the residual ionisation ($x_e \approx 0.6$ %) of the neutral gas. The electron-scattering optical depth is therefore only $\tau_{\mathrm{es}} \approx 0.13$, ≈ 4–20 times below what is needed to produce the observed wings, and the line widths are set by the fitted velocity dispersion. So, for the cocoon model with stellar-mass limit, we attribute the MIRI mismatch mainly to the lack of thermalisation, although the single geometry, fixed illuminating spectrum and grid-edge column of our cocoon may also contribute (Appendix I3).

Although our cocoons do not reproduce the turnover, they still constrain how the dense gas is distributed around the black hole. Both cocoon solutions, with and without the stellar-mass limit, cover the disc only partially with dense gas ($C \simeq 0.22\text{–}0.26$; Section 4.3.2), which points to a clumpy or anisotropic medium. This is in line with the broad Lyα of QSO1, since high-column gas shapes the Balmer break while lower-opacity paths let Lyα and ionising photons escape (Ji et al. 2026a; Tang et al. 2026). So does its UV Fe II emission, which needs dense, partially ionised gas exposed to the central continuum (Tang et al. 2026). The fitted covering fraction is therefore an effective quantity, which may trace openings in the cocoon, anisotropic escape or sightlines of different optical depth. We highlight that this covering fraction refers to the gas, and is distinct from the one of the dust discussed in Section 5.3.

Except for our cocoon, which misses the turnover, both kinds of source reproduce the observed SED shape, so the photometry

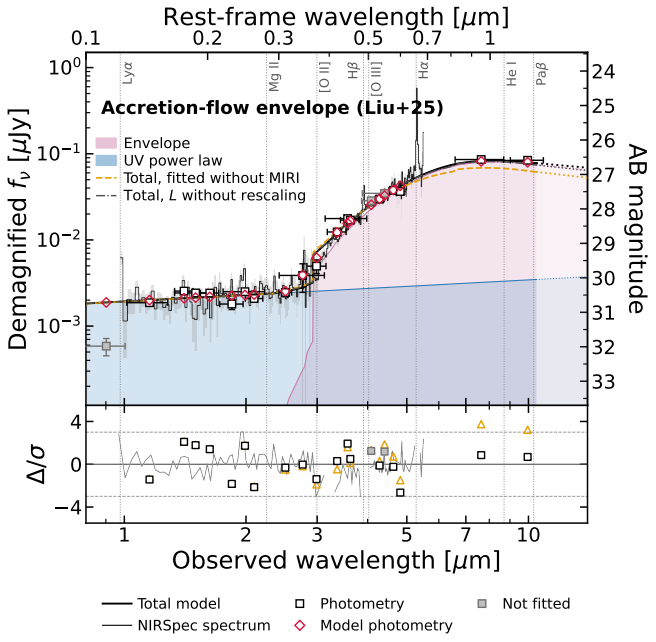


Figure 5. *A single accretion-flow envelope reproduces the continuum of QSO1 from the Balmer break to F1000W, but its luminosity matches the data only for a black-hole mass* ≈ 2.5 *dex below the dynamical estimate.* QSO1 compared with the accretion-flow envelope models of Liu et al. (2025) (Appendix H1). Top: photometry (white squares; grey: bands not fitted) and NIRSpec spectrum, with the fit to all bands (black), its envelope (pink) and UV power-law (blue) components and its synthetic photometry (diamonds), the fit without MIRI (dashed) and the solution whose luminosity matches the data without rescaling (dash-dotted). The model curves are dotted beyond rest-frame 1.3μm, where the envelope spectra are extrapolated. Bottom: residuals, $(f_{\rm obs} - f_{\rm model})/\sigma$, of the photometry for the fits with (squares) and without MIRI (triangles), and of the spectrum for the fit to all bands (grey, averaged over six pixels, with emission lines masked since the models do not include them).

alone cannot decide between them. They, however, rest on different physical requirements. The pseudo-photosphere models we tested need a luminosity close to Eddington, which is in tension with the dynamical black-hole mass. A reddened source instead requires dust that absorbs part of the intrinsic luminosity and re-emits it in the infrared. Among the reddened solutions, those dominated by stars must satisfy the dynamical limit on the host mass (Section 5.2), and all must hide the re-emitted luminosity below our infrared limits (Section 5.3).

5.2 A massive host?

MIRI probes the rest-frame near-infrared, where the light of an evolved host best traces its mass (Bell & de Jong 2001), but in QSO1 this emission is unresolved ($r_{\rm e} < 64$ pc) and follows the same thermal component as the optical. A surviving stellar mass of $\gtrsim 3\times10^9$ M$_\odot$ within $r_{\rm e} < 30$–64 pc (Furtak et al. 2024) would imply $\Sigma_\star = M_\star/(2\pi r_{\rm e}^2) \gtrsim 1$–$5\times10^5$ M$_\odot$ pc^{-2}, at or above the maximum observed in dense stellar systems (Hopkins et al. 2010). Such densities are extreme but not impossible, so they cannot exclude a stellar solution on their own. The dynamics can provide an additional test. Our inferred stellar mass is ≈ 140–200 times the dynamical upper limit on the host stellar mass (Juodžbalis et al. 2026, see also Ji et al. 2025), and even the galaxy-only model of Ma et al. (2025), refitted with MIRI, still requires $\approx 2\times10^9$ M$_\odot$ (Section 4.3.1). One way to reconcile the inferred stellar mass and the dynamical upper limit would be if the dynamical mass were underestimated. In fact, since only the line-of-sight component of the rotation is measured, $v_{\rm obs} = v\sin i$, a nearly face-on disc would hide most of the true velocity thus biasing the estimated enclosed mass by a factor of $1/\sin^2 i$. However, Juodžbalis et al. (2026) fit the inclination together with the mass and found $i = 52° \pm 2°$, and $\approx 45° \pm 10°$ with a non-parametric method. Hiding a factor of ≈ 140–200 would require the true inclination to be only ≈ 3–4°, inconsistent with both estimates. Moreover, similar mass deficits have been found in many LRDs with measured line widths (Ji et al. 2026b; D'Eugenio et al. 2026a; Wang et al. 2025; Torralba et al. 2026a), which are unlikely to all be seen face-on. If LRDs in general contained ~ 10^9–10^{10} M$_\odot$ of stars within a few tens of parsecs, their high number densities (Kokorev et al. 2024) would reintroduce the baryon-budget tension raised by the first massive-galaxy interpretations of these sources (Labbé et al. 2023; Boylan-Kolchin 2023). The stellar solution faces a further problem. It needs dense gas moving at ~ 800 km s^{-1}, as expected near an accreting black hole rather than in H II regions.

A strong Balmer break does not necessarily require evolved stars but can arise from absorption in dense gas rather than from evolved stars (e.g. de Graaff et al. 2025b). In our modelling, however, even when a black hole in dense gas is available, the fit tends to prefer a solution with a strong contribution by stars. The highest-evidence cocoon produces the red continuum with $\approx 4\times10^9$ M$_\odot$ of stars and uses the disc only for the UV. Limiting the stellar mass to maximum values consistent with the dynamical mass disfavours the model ($\Delta\ln(\mathcal{Z}) \simeq 20$–33, see Section 4.3.2). This preference does not come from the Balmer break or the optical continuum. It mainly comes from the MIRI bands, where the cocoon lacks a pseudo-photosphere (Section 5.1), and from the emission lines fit: the Balmer-line profiles and ratios, the high-order Balmer lines just redward of the break, and the UV lines. These are exactly the features our cocoon models describe least well, since they assume a single density, ionisation parameter and column, a single Gaussian line width, and escape-probability line transfer (Appendix I3). Models combining a range of densities and columns, or radiative-transfer models that follow line scattering and the thermalisation of the continuum (e.g. Matthews et al. 2025; Sneppen et al. 2026; Liu et al. 2025), may close the gap.

We therefore regard the massive stellar solutions as unlikely, and the preference of the SED for them as a limitation of our dense-gas models rather than as evidence for a massive host.

5.3 Where is the dust?

The dynamical mass mainly tests the models with stellar populations (Section 5.2). The other reddened models, including the reddened accretion disc, can instead be tested through the amount of dust they require. In the dense-gas picture, the red optical continuum arises without any reddening (Section 5.1). In addition to the SED fits, two independent tracers can help establish whether QSO1 is reddened at all: the emission lines and the gas metallicity. The Balmer decrement of the broad component is large and would imply $A_V \approx$ 2–3 mag if caused by dust (Section 2). However, dense gas near the black hole, inside the sublimation radius ($R_{\rm sub} \approx 0.2$ pc for $L_{\rm bol} \approx 2\times10^{44}$ erg s^{-1}; Barvainis 1987) and therefore dust-free, can also produce large decrements without dust (Ji et al. 2025; Chang et al. 2026; Torralba et al. 2026b; Matthee et al. 2026). The Balmer decrement of the narrow component is instead consistent with Case B (D'Eugenio et al. 2026b), suggesting little dust in the narrow-line gas. This gas, however, extends over a few hundred parsecs (Maiolino et al.

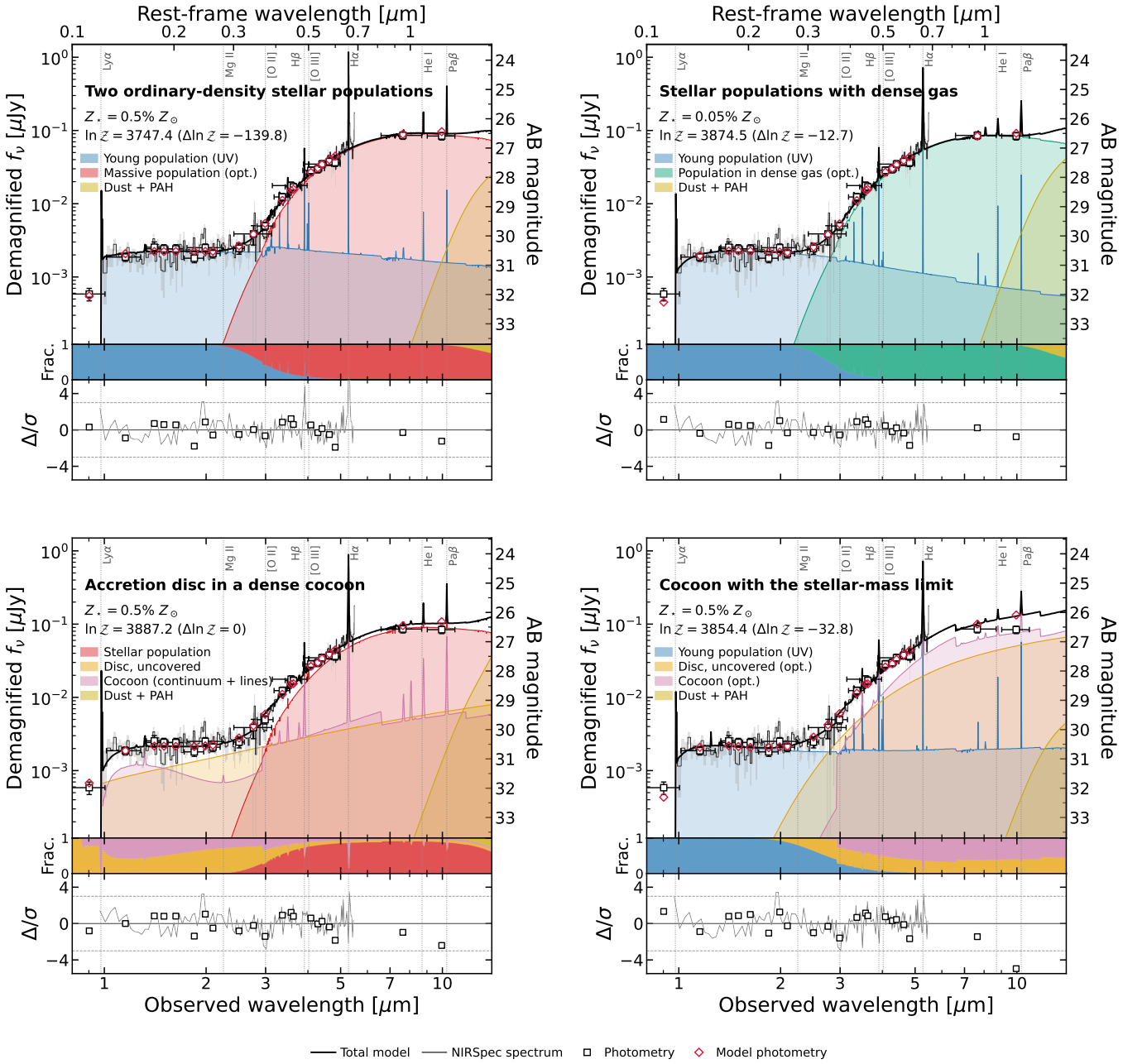


Figure 6. *In our models, the highest-evidence solutions produce the red continuum with* $\approx 4\times10^9$ $M_\odot$ *of stars. With the stellar mass limited by the dynamics, the disc and dense cocoon produce it instead, but over-predict F1000W.* Maximum-likelihood solutions of the representative model families, each at the metallicity of its highest evidence, compared with the NIRSpec spectrum and the photometry: two ordinary-density stellar populations (`zem4`, top left), the highest-evidence stellar model including a dense photoionised component (`zem5`, top right), the highest-evidence accretion-disc cocoon model (`zem4`, bottom left) and the same model with the stellar mass limited to the upper limit on the host stellar mass, $M_\star \leq 10^{7.5}$ $M_\odot$ (`zem4`, bottom right). For each model, the upper panel shows the individual components (coloured), the total model (black), the photometry (squares, with horizontal bars showing the filter widths, and the model photometry as diamonds) and the NIRSpec spectrum (dark grey, with its uncertainty shaded). Dotted vertical lines mark the main emission lines. The middle panel gives the fractional contribution of each component, and the lower panel the residuals, $(f_{\rm obs} - f_{\rm model})/\sigma$, with the spectrum averaged over six pixels and its uncertainty propagated accordingly. Dashed lines mark $\pm3\sigma$.

2026; Ji et al. 2026a) and does not necessarily probe dust in front of the broad-line region. The very low metallicity of QSO1 implies little dust per unit gas, but does not exclude $A_V \approx 2$ mag. For the Galactic ratio, $N_{\rm H}/A_V = 2.2\times10^{21}$ cm^{-2} mag^{-1} (Güver & Özel 2009), scaled linearly to the gas-phase metallicity of QSO1 ($\approx 0.005\ Z_\odot$; Maiolino et al. 2026), $A_V \approx 2$ mag requires $N_{\rm H} \approx 10^{24}$ cm^{-2} outside the sublimation radius[9]. A column of this size is consistent with the X-ray faintness of QSO1 (Section 2). Neither tracer can therefore

[9] We note that $N_{\rm H} \approx 10^{24}$ cm^{-2} is a lower limit if the dust-to-gas ratio falls faster than linearly at low metallicity (Rémy-Ruyer et al. 2014), and an upper limit if the nuclear gas is more enriched than the narrow-line gas.

confirm or rule out dust reddening on its own. The energy budget offers a more direct test.

If QSO1 is reddened, the dust is substantial. Our best-fit reddened solutions have $A_V \approx 2.6$–2.8 mag for the massive stellar populations, ≈ 2.2 mag for the reddened accretion disc and ≈ 1.3 mag for the screen of the cocoon with the stellar-mass limit (Section 4.3). The energy absorbed by this dust must be re-emitted in the infrared, and our limits constrain how much of it can be hidden, and at which temperatures.

For the SED models of Section 4.3.2 the absorbed luminosity is a fitted quantity. Conversely, for the reddened accretion disc it has to be derived from the AGN-only fit to NIRCam and MIRI (Appendix G), whose intrinsic disc has $\log_{10}(\lambda L_{3000}\ [\mathrm{erg\ s^{-1}}]) = 44.22 \pm 0.04$. Between 912 Å and 2.9$\mu$m dust absorbs $L_{\rm abs} = (3.9 \pm 0.3) \times 10^{44}$ erg s^{-1}, 94% of the intrinsic emission in this range. The template does not include the ionising continuum, and extending it below 912 Å with the disc continuum of our cocoon models (Appendix I3) gives $L_{\rm AGN} \approx 1.2 \times 10^{45}$ erg s^{-1}, ≈ 2 times the value from the bolometric correction of Runnoe et al. (2012). Below 912 Å, the energy is absorbed first by the gas, but it is largely re-emitted as lines and recombination continua that the dust can then absorb. We therefore adopt $L_{\rm abs} \approx (0.4$–$1.2) \times 10^{45}$ erg s^{-1} for the reddened accretion disc. The lower value counts only the non-ionising continuum, which the dust must absorb in any case, and the upper value assumes that all the ionising luminosity is eventually reprocessed by dust. The energy budget for the three model families spans a factor of ≈ 30: $(1.3$–$2.3) \times 10^{45}$ erg s^{-1} for the solutions with a massive stellar population, $(0.4$–$1.2) \times 10^{45}$ erg s^{-1} for the reddened accretion disc, and $(0.7$–$1.0) \times 10^{44}$ erg s^{-1} for the cocoon with the stellar-mass limit.

Where this energy emerges depends on the dust temperature (Figure 7). Hot dust ($\gtrsim 1000$ K) emits mostly near rest-frame 3μm, warm dust (100–600 K) at 6–40μm and cold dust ($\lesssim 50$ K) near 100μm. Only hot dust is constrained directly by NIRCam and MIRI, through its Wien tail. Such temperatures are reached mainly when an AGN heats the dust, since dust heated by stars stays cooler. In the cocoon with the stellar-mass limit, which already over-predicts F1000W by 5σ (Section 4.3.2), hot dust would only increase the tension. We therefore test hot dust for the reddened accretion disc only. The fits of Section 4.3.1 already disfavour quasar-like hot dust. To quantify how much is allowed, we fitted a single-temperature greybody ($L_\nu \propto \nu^\beta B_\nu(T_{\rm d})$, $\beta = 0$–2) jointly with the reddened accretion disc to the NIRCam and MIRI photometry, and integrated it over all frequencies to obtain its luminosity (Appendix G). Based on this model, dust at 1200 K can re-emit at most 2% of the lower value of $L_{\rm abs}$, and dust at 1000 K at most $\approx 7\%$ (Table G1)[10]. The 1200 K limit corresponds to $L_{\rm hot}/L_{\rm AGN} \lesssim 0.007$, a geometry-dependent proxy for the covering factor of the hot dust. This is more than ten times below the typical values of luminous quasars (≈ 0.1) and Seyfert 1 galaxies (≈ 0.15–0.35; Mor & Trakhtenbrot 2011; Mor & Netzer 2012), although these values vary widely between objects, down to quasars with no detectable hot dust (Hao et al. 2010; Jiang et al. 2010; Lyu & Rieke 2017). This comparison should be taken with care though. We convert the hot-dust flux into a luminosity assuming isotropic emission, whereas the near-infrared emission of a clumpy torus depends on the viewing angle by up to a factor of a few (Nenkova et al. 2008; Hönig & Kishimoto 2010). For a reddened accretion disc, our sightline crosses the dusty medium, so the hot inner face of the torus may be partly hidden and its intrinsic luminosity a few times higher than we infer. The limit also rests on a single band on the Wien tail (F1000W, rest-frame 1.24μm), so it is sensitive to the calibration of this band, to its $\approx 7\%$ line contribution (see Section 4.2) and to the slope of the disc template beyond 1μm. With these caveats, QSO1 lies towards the hot-dust-poor end of type-1 AGN, but only up to rest-frame 1.24μm. A torus whose emission rises only at longer wavelengths, as in the LRD stacks (Pérez-González et al. 2026; Delvecchio et al. 2025), is not constrained by our data (see Section 5.5).

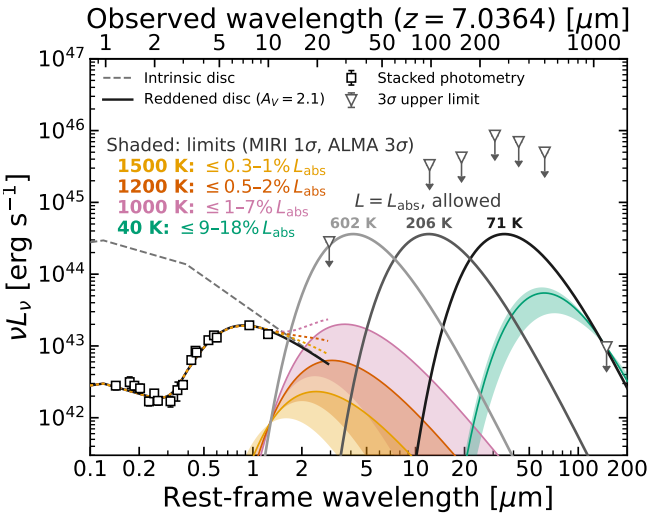


Figure 7. *For a reddened accretion disc, hot dust ($\gtrsim 1000$ K) can re-emit at most a few per cent of the absorbed luminosity, and cold dust (≈ 40 K) at most 15 per cent, whereas warm dust at ≈ 70–600 K could re-emit all of it without exceeding any limit.* Dust energy budget of QSO1 under the reddened-disc hypothesis (Appendix G): stacked NIRCam and MIRI photometry, 3σ upper limits from MIPS, *Herschel* and ALMA, and the intrinsic and attenuated disc of the reddened-AGN model. Shaded bands show single-temperature dust components at their limits, labelled with the fraction of the absorbed luminosity $L_{\rm abs}$ they can re-emit. These limits are 1σ for the 1000, 1200 and 1500 K components, which are fitted jointly with the disc to the NIRCam and MIRI detections ($\beta = 0$–2; line: blackbody), and 3σ for the 40 K component, which is set by ALMA ($\beta = 1$–2; line: $\beta = 1.8$). Dotted lines show the total of the re-fitted disc and each hot component. Solid grey curves show greybodies ($\beta = 1.8$) that re-emit all of $L_{\rm abs}$ without violating any limit, at the lowest (71 K) and highest (602 K) such temperatures and at their logarithmic midpoint (206 K). All dust emission is shown as observed, including the CMB contrast.

The hot-dust limit weakens quickly towards cooler grains, from 2% of $L_{\rm abs}$ at 1200 K to $\approx 7\%$ at 1000 K and ≈ 6–50% at 800 K (depending on β, see Table G1). Still, in the reddened accretion disc case, most of the absorbed energy must therefore emerge from cooler dust, which is loosely constrained only by the far-infrared and millimetre limits. Normalising a greybody with $\beta = 1.8$ to these limits (Appendix G), the full absorbed luminosity of the reddened accretion disc can be hidden at ≈ 70–600 K, while ALMA limits dust at 40 K to at most 15% of it (Figure 7). For the massive stellar solutions, the larger absorbed luminosity can be hidden only at ≈ 100–440 K. Dust can reach such temperatures in compact, low-metallicity starbursts, much warmer than in typical star-forming galaxies, and produce a steep mid-infrared rise without an AGN (e.g. Hainline et al. 2016; Sturm et al. 2025; Rieke et al. 2025). For the cocoon with the stellar-

[10] Both values are for $\beta = 0$, the least restrictive case. This case also approximates optically thick dust, whose surface emits close to a blackbody, as expected for the clouds of a clumpy AGN torus (Nenkova et al. 2008; Hönig & Kishimoto 2010; Hönig 2019).

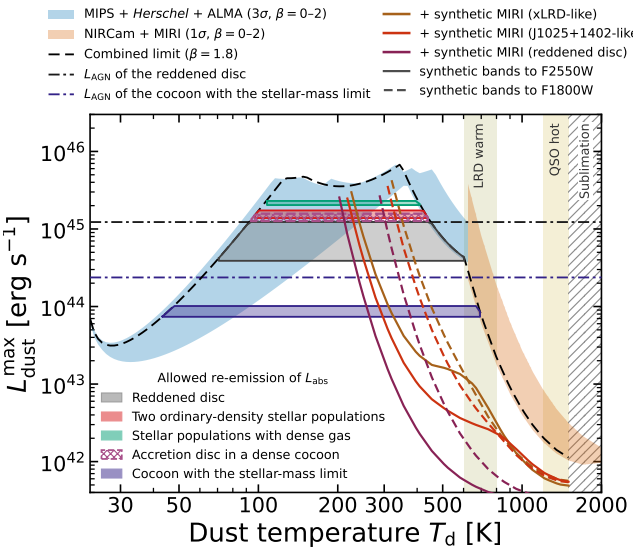


Figure 8. *No solution is excluded by energy balance, but the absorbed luminosity of the most attenuated solutions can be hidden only in a limited range of dust temperatures, which deeper MIRI imaging at longer wavelengths can test.* Maximum luminosity of dust emission at a single temperature allowed by the NIRCam and MIRI photometry (orange; fitted jointly with the reddened-disc model) and by the MIPS, *Herschel* and ALMA limits (blue; including the CMB contrast), for $\beta = 0$–2. Each limit is shown only where it is the tighter of the two. The dashed black curve is the combined limit for $\beta = 1.8$. Shaded regions show the luminosity absorbed by dust in each model, plotted over the temperatures at which the combined limit allows it to be re-emitted in full as a single (modified) blackbody. For the reddened accretion disc (Section 5.3) the region extends from the absorption between 912 Å and 2.9μm to the full intrinsic luminosity, and for the solutions of Section 4.3.2 it spans the 16th–84th percentiles of the absorbed luminosity. Dash-dotted lines mark the intrinsic disc luminosity of the reddened accretion disc and of the cocoon with the stellar-mass limit, both computed with the disc continuum of Appendix I3. The cocoon region lies below its $L_{\rm AGN}$ because most of the disc luminosity is emitted below 912 Å and is absorbed by gas or escapes, not by dust. Vertical bands mark the temperatures of hot dust in type-1 quasars and of the warm-dust excess in low-redshift LRDs (Ashall et al. 2026), and the hatched band the sublimation range of silicate and graphite grains ($\approx$ 1500–2000 K; e.g. Barvainis 1987). Brown, red and purple curves show the combined limit on additional dust if QSO1 were also detected with S/N = 10 in F1280W, F1500W and F1800W (dashed) or in F1280W–F2550W (solid), with an SED that follows beyond F1000W the xLRD stack of Pérez-González et al. (2026), *the Egg* (Lin et al. 2025; Ji et al. 2026b) or the reddened-disc model, normalised to QSO1 at rest-frame 1.24μm. Temperatures are those at $z = 7.04$, including CMB heating, which is negligible at $T_{\rm d} \gtrsim 40$ K.

mass limit, the absorbed luminosity can be hidden at $\approx$ 40–700 K, almost any temperature allowed by our limits (Figure 8). No solution is therefore excluded on energy-balance grounds, but the dust of the reddened accretion disc and of the stellar solutions must lie, at least in part, at temperatures that longer-wavelength MIRI imaging can test (Section 5.5).

Since grains in radiative equilibrium cool with distance from their heating source (Barvainis 1987), the estimated dust temperature constraints can also set where the dust can be. For the massive stellar solutions, dust at $\lesssim$ 400 K lies at $R \gtrsim 25$ pc (applying the same scaling as an approximation), i.e. at or beyond the size limit of QSO1. For the cocoon with the stellar-mass limit, the small budget leaves the dust location unconstrained. For the reddened accretion disc, dust at $\lesssim$ 600 K lies at $R \gtrsim 6$ pc for $L_{\rm AGN} \approx 1.2 \times 10^{45}$ erg s^{-1}, $\approx$ 13 times the sublimation radius at this luminosity. A shell at this distance, covering the whole sky with the column needed for $A_V \approx 2$ mag at the metallicity of QSO1 ($N_{\rm H} \approx 10^{24}$ cm^{-2}), contains $M_{\rm gas} \approx 3 \times 10^7\ (R/14\ {\rm pc})^2\ {\rm M}_\odot$. At $R \approx 50$ pc ($T_{\rm d} \approx 280$ K), this approaches the dynamical mass ($< 4 \times 10^8$ M$_\odot$; Ji et al. 2025). Both the large cavity and the large mass follow from assuming a single temperature. A torus with a range of temperatures can instead extend to the sublimation radius, provided its hottest ($\gtrsim$ 1000 K) dust carries no more than a few per cent of $L_{\rm abs}$, as in hot-dust-poor quasars (Hao et al. 2010; Lyu & Rieke 2017), and most of the luminosity is re-emitted by cooler dust further out. We note that $L_{\rm abs}$ assumes that the dust covers all sightlines, like ours. If the dust of the reddened accretion disc covers only a fraction C_f of the sky, it absorbs and re-emits only $C_f\ L_{\rm abs}$, and its gas mass is lower by the same factor. The rest of the disc light escapes unattenuated along the uncovered sightlines, towards other observers. For $C_f = 0.3$ (0.1), the absorbed luminosity can then be hidden at $\approx$ 50–670 K ($\approx$ 35–750 K), with dust at 1200 K carrying at most $\approx$ 7% (22%) of it. Such covering factors are at the low end of those of AGN. For the obscuring gas, typical values are ≈ 0.85 at $\lambda_{\rm Edd} \lesssim 0.03$ and ≈ 0.4 above (Ricci et al. 2017), a range that includes QSO1 ($\lambda_{\rm Edd} \approx 0.005$–0.2; Section 5.1). For the infrared-emitting dust, the covering factor decreases with luminosity, from about unity in low-luminosity AGN to ≈ 0.1 in luminous quasars (Maiolino et al. 2007), with a median of ≈ 0.6 in X-ray-selected type-1 AGN (Lusso et al. 2013). Madau & Maiolino (2026) adopt $C_f \approx 0.15$ in a model in which LRDs are blue broad-line AGN seen through dust at high inclination.

The covering factor also links QSO1 to the LRD population. In the reddened accretion disc interpretation, the fraction of systems seen through their dust, and hence selected as LRDs, equals the covering factor. For $C_f = 0.3$ (0.1), each LRD would have $\approx$ 2 (9) counterparts seen without dust, as blue broad-line AGN of similar intrinsic luminosity. At $z \sim 5$, LRDs are $\approx$ 100 times more abundant than UV-selected AGN of similar dust-corrected luminosity (Kokorev et al. 2024), which would require dust covering most of the sky. Among the broad-line AGN identified spectroscopically with JWST, however, LRDs make up $\approx$ 30 per cent, a fraction that rises with luminosity and drops below 15 per cent under $L_{\rm bol} \approx 1.5 \times 10^{44}$ erg s^{-1} (Hainline et al. 2025). At the intrinsic luminosity of QSO1, these small samples suggest $C_f \gtrsim 0.3$, which disfavours the lowest covering factors but not the case $C_f \approx 0.3$. The energy budget derived above for full covering is therefore the most demanding case.

The broad Lyα of QSO1 (Tang et al. 2026) constrains the geometry further. A uniform dust screen would suppress it by $\approx$ 27 mag for the reddened accretion disc ($A_V \approx 2.2$ mag) and by $\approx$ 17 mag in the cocoon with the stellar-mass limit ($A_V \approx 1.3$ mag). In such scenarios, the dust must therefore be clumpy, as typically found in AGN tori (e.g. Tristram et al. 2007; GRAVITY Collaboration et al. 2020; Hönig 2019). It can then cover most sightlines, as required above, while a small fraction of the light leaks through gaps between the clumps. In the reddened-disc fit this unattenuated fraction is $\approx$ 1% (Appendix G), and it also produces the blue UV continuum. With Case-B or typical broad-line Lyα/Hα ratios and the broad-line attenuation, this fraction predicts a broad Lyα luminosity within a factor of a few of the observed one, before any absorption by the intergalactic medium. In the cocoon, the screen may instead partly stand in for reddening by the dense gas itself, in which case its dust emission is an upper limit.

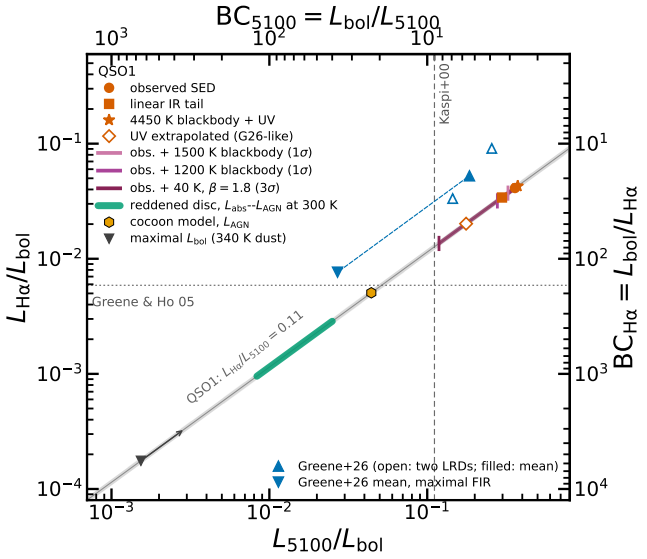


Figure 9. *Without warm dust, the bolometric corrections of QSO1 are comparable to those of other LRDs and well below those of type-1 AGN. They would exceed the type-1 values only if a reddened accretion disc re-emitted its absorbed luminosity as warm dust.* Hα and 5100Å luminosities of QSO1 relative to its bolometric luminosity, for the luminosity integrated over the observed SED (orange symbols, a lower limit on $L_{\rm bol}$), for the observed SED plus the dust components of Figure 7 at their limits (segments: allowed range), for a reddened accretion disc whose absorbed luminosity, from $L_{\rm abs}$ to $L_{\rm AGN}$, is re-emitted at 300 K (green), for the intrinsic disc luminosity of the cocoon model with the stellar-mass limit (hexagon), and for the maximal luminosity allowed by the MIRI and far-infrared limits (triangle, upper limit on $L_{\rm bol}$). All QSO1 points lie on the line set by its $L_{\rm H\alpha}/L_{5100}$. Blue triangles: the two LRDs of Greene et al. (2026), their mean and the mean with their maximal far-infrared emission. Dashed and dotted lines: bolometric corrections of type-1 AGN (Kaspi et al. 2000; Greene & Ho 2005). The top and right axes give the bolometric corrections.

5.4 Bolometric luminosity

The dust budget also sets the bolometric luminosity of QSO1. Integrating the de-magnified SED from Lyα to 1 mm, with a Rayleigh–Jeans tail beyond F1000W, gives $L_{\rm obs} = 2.9\times10^{43}$ erg s^{-1} (3.5×10^{43} erg s^{-1} with a linear decline to the ALMA band as in Greene et al. 2026), a lower limit on $L_{\rm bol}$ since it omits the ionising and X-ray emission. With $L_{5100} = 1.05\times10^{43}$ erg s^{-1} and $L_{\rm H\alpha} = (1.20\pm0.07)\times10^{42}$ erg s^{-1} (measured on the Ima-B spectrum, whose broad-line equivalent widths are about half those of Ima-C; Ji et al. 2025), the bolometric corrections are $\rm BC_{5100}\approx2.8$–3.4 and $\rm BC_{H\alpha}\approx24$–29 (Figure 9). They are comparable to those of the two LRDs of Greene et al. (2026) (5.4 and 19) and well below those of type-1 AGN (9 and 170; Kaspi et al. 2000; Greene & Ho 2005), whose Hα correction would give $L_{\rm bol}\approx2\times10^{44}$ erg s^{-1} (Juodžbalis et al. 2026), ≈ 6 times the observed luminosity. Hot dust within our limits raises these corrections only slightly, to at most $\rm BC_{5100}\approx3.6$ and $\rm BC_{H\alpha}\approx31$ (≥ 1200 K), and cold dust by at most a factor of ≈ 2.5, to ≈ 8 and ≈ 75 (≈ 40 K). Warm dust can raise them much further. A reddened accretion disc re-emitting its absorbed luminosity at ≈ 300 K would have $L_{\rm bol}\approx(0.4$–$1.3)\times10^{45}$ erg s^{-1}, $\rm BC_{5100}\approx40$–120 and $\rm BC_{H\alpha}\approx350$–1050, above even the maximal values of Greene et al. (2026), and the disc of the cocoon with the stellar-mass limit falls in between (2.4×10^{44} erg s^{-1}, $\rm BC_{5100}\approx23$, $\rm BC_{H\alpha}\approx200$). The largest luminosity compatible with all our limits, for dust at ≈ 340 K, is $L_{\rm bol} < 6.8\times10^{45}$ erg s^{-1}.

Table 2. Expected flux densities of Ima-A (image plane, i.e. not corrected for magnification) in the MIRI bands beyond F1000W, if the SED of QSO1 continued like the xLRD stack of Pérez-González et al. (2026), like *the Egg* (Lin et al. 2025; Ji et al. 2026b) or like the reddened accretion disc model of Section 4.3.1, each normalised to QSO1 at rest-frame 1.24μm. For reference, Ima-A has 0.91 and 0.90 μJy (24.00 and 24.02 AB) in F770W and F1000W.

Filter (rest-frame μm)	xLRD stack [μJy] (AB)	*the Egg* [μJy] (AB)	reddened disc [μJy] (AB)
F1280W (1.59)	0.89 (24.03)	0.88 (24.04)	0.90 (24.02)
F1500W (1.86)	0.96 (23.94)	0.95 (23.96)	0.86 (24.06)
F1800W (2.24)	1.18 (23.72)	0.98 (23.92)	0.81 (24.13)
F2100W (2.61)	1.47 (23.48)	0.99 (23.92)	0.76 (24.20)
F2550W (3.17)	1.99 (23.15)	1.02 (23.87)	0.69 (24.31)

5.5 Predictions for longer-wavelength MIRI imaging

Our data stop at rest-frame 1.24μm, while the LRD stacks and local LRDs depart most from a single thermal component at 2–3μm (Section 4.2). We therefore predict what MIRI imaging beyond F1000W would see in QSO1 for three continuations of its SED: the xLRD stack of Pérez-González et al. (2026), *the Egg* (Lin et al. 2025; Ji et al. 2026b) and the reddened-disc model of Section 4.3.1, each normalised to QSO1 at rest-frame 1.24μm (Table 2). The xLRD and *the Egg* continuations would exceed the 4450 K blackbody by factors of ≈ 2–5 at rest-frame 2–3μm. The excess would carry $L_{\rm d}\approx(1$–$2)\times10^{43}$ erg s^{-1} up to rest-frame ≈ 20μm, consistent with the warm dust inferred for low-redshift LRDs (≈ 500–700 K; Ashall et al. 2026). This emission is allowed by our limits, as it lies ≈ 20–40 times below the MIPS limit. It would raise $L_{\rm obs}$ by ≈ 40–80%, i.e. to $\rm BC_{5100}\approx4$–5, comparable to the values of Greene et al. (2026). However, it would amount to only a few per cent of the absorbed luminosity of the reddened accretion disc or of the massive stellar solutions, so the bulk of that luminosity would still have to be re-emitted by cooler dust.

In the image plane of Ima-A, the three continuations give the same F1280W flux density, ≈ 0.9 μJy (≈ 24.0 AB). They separate at longer wavelengths. F1800W ranges from 0.81 μJy (24.1 AB) for the reddened accretion disc to 1.18 μJy (23.7 AB) for the xLRD stack, and F2550W from 0.69 μJy (24.3 AB) to 1.99 μJy (23.2 AB), with *the Egg* in between (0.98 and 1.02 μJy, i.e. 23.9 AB, in both bands). *The Cliff* (de Graaff et al. 2025b) predicts flux densities within 5% of those of *the Egg* in all five bands. If QSO1 followed the xLRD or *the Egg* SED and were detected at S/N = 10 in F1280W–F2550W, the excess up to rest-frame 3.2μm would be measured as dust at ≈ 600–650 K with $L_{\rm d}\approx(0.2$–$1)\times10^{43}$ erg s^{-1}. The temperature at which the near- and far-infrared limits cross would drop from ≈ 620 to ≈ 220 K, and the absorbed luminosity of a reddened accretion disc could be hidden only at ≈ 70–250 K, compared with 70–600 K today (Figure 8). Imaging up to F1800W alone would already restrict it to ≲ 300–380 K.

6 CONCLUSIONS

We have presented the first rest-frame near-infrared observations of the lensed LRD QSO1 at $z = 7.04$, obtained with MIRI in F770W and F1000W. Our main results are:

(i) All three images are unresolved, with a conservative source-plane 95% upper limit of $r_e < 64$ pc for Ima-A. The MIRI-to-NIRCam continuum ratios of Ima-A and Ima-C agree within $\approx 5\%$, with no evidence for wavelength-dependent variability above $\approx 15\%$ over the observer-frame ≈ 19 yr (≈ 2.4 yr rest-frame) delay between Ima-A and Ima-C, whereas the broad lines have been reported to vary (Furtak et al. 2025; Ji et al. 2025).

(ii) The steep optical rise turns over between 0.96 and 1.24μm. A single $T \simeq 4450$ K blackbody describes the optical continuum and both MIRI bands, and a hotter, reddened thermal continuum fits equally well. Up to 1.24μm, the SED of QSO1 is typical of LRDs, and its UV-to-optical ratio places it among the extreme LRDs of Pérez-González et al. (2026). Without MIRI, models constrained by the UV-to-optical data mispredict the 1μm continuum by 15–76%.

(iii) Within the model families explored, the spectrum requires a dense, strongly reprocessing component and differential attenuation ($\Delta \ln(\mathcal{Z}) \gtrsim 80$ against a shared screen). The highest-evidence solutions produce the red continuum with $\gtrsim 3 \times 10^9$ $M_\odot$ of stars, $\approx$ 140–200 times the upper limit on the host stellar mass. Within this limit, the disc and cocoon produce the red continuum but over-predict F1000W, with an evidence lower by $\Delta \ln(\mathcal{Z}) \simeq 20$–33 that comes from the MIRI bands and the emission lines, the features our cocoon models describe least well. Accretion-flow envelope models reproduce the shape of the turnover, but their luminosity matches QSO1 only for a black-hole mass ≈ 2.5 dex below the dynamical one, which implies $\lambda_{\rm Edd} \approx 0.005$–0.03 rather than the near-Eddington accretion these models assume.

(iv) There is no evidence for the standard quasar hot-dust upturn up to 1.24μm. For a disc reddened by $A_V \approx 2$ mag, which would absorb $L_{\rm abs} \approx (0.4\text{–}1.2) \times 10^{45}$ erg s^{-1}, at most $\approx 2\%$ can be re-emitted by hot dust ($T_{\rm d} \geq 1200$ K) and at most $\approx 15\%$ by cold dust ($T_{\rm d} \approx 40$ K). The remainder could be emitted undetected by warm dust at $\approx$ 70–600 K, and the larger budget of the massive stellar solutions only at $\approx$ 100–400 K. The cocoon with the stellar-mass limit absorbs ≈ 20 times less and is unconstrained. A reddened accretion disc therefore remains allowed, provided that most of its absorbed luminosity emerges at $\approx$ 70–600 K and dust hotter than ≈ 1000 K carries at most a few per cent of it, as in hot-dust-poor quasars. Without dust, the observed luminosity gives $\mathrm{BC}_{5100} \approx 3$ and $\mathrm{BC}_{\mathrm{H}\alpha} \approx 25$, comparable to other LRDs and well below type-1 AGN. If a reddened accretion disc re-emitted its absorbed luminosity as warm dust, these would rise to $\approx$ 40–120 and $\approx$ 350–1050.

If the upper limit on the host stellar mass holds, the stellar solutions explored here are excluded, and our results favour an accretion-powered origin of the red continuum, either reddened by dust or processed by dense gas, which our data cannot yet distinguish. An accretion-powered source is also suggested by the broad Lyα and far-UV Fe II emission of QSO1. Our Cloudy cocoons do not form a pseudo-photosphere and miss the turnover, whereas envelope models that do form one miss the luminosity expected for the dynamical black-hole mass. Reconciling the two, and exploring non-isotropic dust geometries that would relax the energy-balance constraints derived here, are needed before QSO1 can be modelled self-consistently.

Even with MIRI, our description of the continuum of QSO1 stops at rest-frame 1.24μm, short of the range where LRDs depart most from a single thermal component. QSO1 belongs to the extreme LRDs of Pérez-González et al. (2026), the subtype whose stack rises again beyond rest-frame $\approx 2\mu$m, by factors of $\approx$ 2–5 over the 4450 K blackbody at 2–3μm. For the most extreme LRDs, near-infrared data up to $\approx 1.2\mu$m are therefore not sufficient to constrain the dust budget or the nature of the red continuum. At $z \gtrsim 7$ this range lies beyond observed 16μm and can be reached only with deep MIRI imaging at $\gtrsim 18\mu$m (F1800W, F2100W and F2550W). For Ima-A, the xLRD stack, *the Egg* and a reddened accretion disc predict 0.8–1.2 μJy (23.7–24.1 AB) in F1800W and 0.7–2.0 μJy (23.2–24.3 AB) in F2550W (Section 5.5). Detections at S/N = 10 up to F2550W would measure any warm-dust excess and confine the dust of a reddened accretion disc to $\approx$ 70–250 K, and F1800W alone would restrict it to $\lesssim$ 300–380 K. Such data would tighten the energy budget of every solution considered here and distinguish a true pseudo-photosphere from a reddened, hotter continuum.

ACKNOWLEDGEMENTS

The authors thank R. Maiolino, K. Caputi, S. Finkelstein and A. Sneppen for the useful discussion. The authors thank X. Ji for sharing the data of J1025+1402 (the Egg). This research is based in part on observations made with the NASA/ESA Hubble Space Telescope obtained from the Space Telescope Science Institute, which is operated by the Association of Universities for Research in Astronomy, Inc., under NASA contract NAS 5–26555. This work is based in part on observations made with the NASA/ESA/CSA James Webb Space Telescope. The data were obtained from the Mikulski Archive for Space Telescopes at the Space Telescope Science Institute, which is operated by the Association of Universities for Research in Astronomy, Inc., under NASA contract NAS 5-03127 for JWST. These observations are associated with programs 1324, 2561, 2767, 2883, 3516, 3538, 4111, 5578 and 9214. The authors acknowledge the team led by PIs F. Sun (#2883) and E. Iani (#3538) for developing their observing programs with a zero-exclusive-access period. Some of the data products presented herein were retrieved from the Dawn JWST Archive (DJA). DJA is an initiative of the Cosmic Dawn Center (DAWN), which is funded by the Danish National Research Foundation under grant DNRF140. PR acknowledges support from the University of Texas at Austin Cosmic Frontier Center. FDE acknowledges support by the Science and Technology Facilities Council (STFC), by the ERC through Advanced Grant 695671 "QUENCH", and by the UKRI Frontier Research grant RISEandFALL. Funded by the European Union (ERC, AGENTS, 101076224). Views and opinions expressed are however those of the author(s) only and do not necessarily reflect those of the European Union or the European Research Council. Neither the European Union nor the granting authority can be held responsible for them. Generative artificial-intelligence tools (Anthropic - Claude Opus 5.5) were used to assist with language polishing, improve the readability and presentation of the figures, and support the software implementation of the models described in Section 4.3.2 and Appendix I. All scientific choices, model validation, analyses, interpretations, and final presentation were reviewed and verified by the authors.

DATA AVAILABILITY

The JWST and HST data used in this work are available from the Mikulski Archive for Space Telescopes (MAST). The NIRSpec spectra are available from the DAWN JWST Archive. The derived data underlying this article will be shared on reasonable request to the corresponding author.

REFERENCES

Akins H. B., et al., 2025, ApJ, 991, 37
Ananna T. T., Bogdán Á., Kovács O. E., Natarajan P., Hickox R. C., 2024, ApJ, 969, L18
Ashall C., et al., 2026, arXiv e-prints, p. arXiv:2608.29011
Baggen J. F. W., et al., 2024, ApJ, 977, L13
Barbary K., 2016, The Journal of Open Source Software, 1, 58
Barro G., et al., 2024, ApJ, 963, 128
Barro G., et al., 2026, ApJ, 1003, 96
Barvainis R., 1987, ApJ, 320, 537
Begelman M. C., Dexter J., 2026, ApJ, 996, 48
Bell E. F., de Jong R. S., 2001, ApJ, 550, 212
Bertin E., Arnouts S., 1996, A&AS, 117, 393
Bezanson R., et al., 2024, ApJ, 974, 92
Bosman S. E. I., et al., 2025, arXiv e-prints, p. arXiv:2511.02902
Boylan-Kolchin M., 2023, Nature Astronomy, 7, 731
Brammer G., 2023, msaexp: NIRSpec analysis tools, doi:10.5281/zenodo.8233475
Brazzini M., D'Eugenio F., Maiolino R., Juodžbalis I., Ji X., Scholtz J., Chang S.-J., 2025, MNRAS, 544, L167
Calzetti D., Armus L., Bohlin R. C., Kinney A. L., Koornneef J., Storchi-Bergmann T., 2000, ApJ, 533, 682
Carnall A. C., 2017, arXiv e-prints, p. arXiv:1705.05165
Casey C. M., et al., 2025, ApJ, 990, L61
Chabrier G., 2003, PASP, 115, 763
Chang S.-J., Gronke M., Matthee J., Mason C., 2026, MNRAS, 545, staf2131
Chisholm J., et al., 2026, ApJ, 1004, L4
Choi J., Dotter A., Conroy C., Cantiello M., Paxton B., Johnson B. D., 2016, ApJ, 823, 102
Conroy C., Gunn J. E., White M., 2009, ApJ, 699, 486
D'Eugenio F., et al., 2026a, MNRAS, 545, staf2117
D'Eugenio F., et al., 2026b, MNRAS, 547, stag401
Delvecchio I., et al., 2025, A&A, 704, A313
Di Mascolo L., 2026, socca: Source Characterization using a Composable Analysis, Astrophysics Source Code Library, record ascl:2602.005 (ascl:2602.005)
Dong X., Wang T., Wang J., Yuan W., Zhou H., Dai H., Zhang K., 2008, MNRAS, 383, 581
Dotter A., 2016, ApJS, 222, 8
Eldridge J. J., Stanway E. R., Xiao L., McClelland L. A. S., Taylor G., Ng M., Greis S. M. L., Bray J. C., 2017, Publ. Astron. Soc. Australia, 34, e058
Foreman-Mackey D., Hogg D. W., Lang D., Goodman J., 2013, PASP, 125, 306
Fujimoto S., et al., 2024, ApJS, 275, 36
Fujimoto S., et al., 2025, ApJS, 278, 45
Furtak L. J., et al., 2023, ApJ, 952, 142
Furtak L. J., et al., 2024, Nature, 628, 57
Furtak L. J., et al., 2025, A&A, 698, A227
GRAVITY Collaboration et al., 2020, A&A, 634, A1
Glikman E., Helfand D. J., White R. L., 2006, ApJ, 640, 579
Gordon K., 2024, The Journal of Open Source Software, 9, 7023
Gordon K. D., Clayton G. C., Misselt K. A., Landolt A. U., Wolff M. J., 2003, ApJ, 594, 279
Gordon K. D., Clayton G. C., Decleir M., Fitzpatrick E. L., Massa D., Misselt K. A., Tollerud E. J., 2023, ApJ, 950, 86
Greene J. E., Ho L. C., 2005, ApJ, 630, 122
Greene J. E., et al., 2024, ApJ, 964, 39
Greene J. E., et al., 2026, ApJ, 996, 129
Gunasekera C. M., et al., 2025, Rev. Mex. Astron. Astrofis., 61, 120
Güver T., Özel F., 2009, MNRAS, 400, 2050
Hainline K. N., Reines A. E., Greene J. E., Stern D., 2016, ApJ, 832, 119
Hainline K. N., et al., 2025, ApJ, 979, 138
Hall P. B., 2007, AJ, 133, 1271
Hao H., et al., 2010, ApJ, 724, L59
Harikane Y., et al., 2023, ApJ, 959, 39
Heintz K. E., et al., 2024, Science, 384, 890
Hönig S. F., 2019, ApJ, 884, 171
Hönig S. F., Kishimoto M., 2010, A&A, 523, A27
Hopkins P. F., Murray N., Quataert E., Thompson T. A., 2010, MNRAS, 401, L19
Hviding R. E., et al., 2025, A&A, 702, A57
Inayoshi K., 2025, ApJ, 988, L22
Inayoshi K., Maiolino R., 2025, ApJ, 980, L27
Inoue A. K., Shimizu I., Iwata I., Tanaka M., 2014, MNRAS, 442, 1805
Ji X., et al., 2025, MNRAS, 544, 3900
Ji X., et al., 2026a, arXiv e-prints, p. arXiv:2604.03370
Ji X., et al., 2026b, MNRAS, 545, staf2235
Jiang L., et al., 2010, Nature, 464, 380
Jiang Y.-F., Stone J. M., Davis S. W., 2014, ApJ, 796, 106
Juodžbalis I., et al., 2024, MNRAS, 535, 853
Juodžbalis I., et al., 2026, Nature, 653, 1017
Just D. W., Brandt W. N., Shemmer O., Steffen A. T., Schneider D. P., Chartas G., Garmire G. P., 2007, ApJ, 665, 1004
Kapoor S., et al., 2026, arXiv e-prints, p. arXiv:2607.00084
Kaspi S., Smith P. S., Netzer H., Maoz D., Jannuzi B. T., Giveon U., 2000, ApJ, 533, 631
Kido D., Ioka K., Hotokezaka K., Inayoshi K., Irwin C. M., 2025, MNRAS, 544, 3407
Kim M., et al., 2026, arXiv e-prints, p. arXiv:2607.10282
Kocevski D. D., et al., 2023, ApJ, 954, L4
Kocevski D. D., et al., 2025, ApJ, 986, 126
Kokorev V., et al., 2024, ApJ, 968, 38
Kokorev V., et al., 2026, arXiv e-prints, p. arXiv:2609.09271
Kokubo M., Harikane Y., 2025, ApJ, 995, 24
Labbé I., et al., 2023, Nature, 616, 266
Labbe I., et al., 2025, ApJ, 978, 92
Lambrides E., et al., 2026, Nature Astronomy, 10, 868
Lange J. U., 2023, MNRAS, 525, 3181
Leitherer C., Li I.-H., Calzetti D., Heckman T. M., 2002, ApJS, 140, 303
Levi M., et al., 2019, in Bulletin of the American Astronomical Society. AIP, p. 57 (arXiv:1907.10688), doi:10.48550/arXiv.1907.10688
Lin R., et al., 2025, ApJ, 980, L34
Lin X., et al., 2026, arXiv e-prints, p. arXiv:2605.21574
Liu H., Jiang Y.-F., Quataert E., Greene J. E., Ma Y., 2025, ApJ, 994, 113
Liu H., Jiang Y.-F., Quataert E., Greene J. E., Ma Y., Lin X., 2026, arXiv e-prints, p. arXiv:2603.02317
Lucy L. B., 1974, AJ, 79, 745
Lusso E., Risaliti G., 2016, ApJ, 819, 154
Lusso E., et al., 2013, ApJ, 777, 86
Lyu J., Rieke G. H., 2017, ApJ, 841, 76
Ma Y., et al., 2025, ApJ, 981, 191
MacLeod C. L., et al., 2010, ApJ, 721, 1014
Madau P., Maiolino R., 2026, A&A, 714, A276
Maiolino R., Shemmer O., Imanishi M., Netzer H., Oliva E., Lutz D., Sturm E., 2007, A&A, 468, 979
Maiolino R., et al., 2024, Nature, 627, 59
Maiolino R., et al., 2025, MNRAS, 538, 1921
Maiolino R., et al., 2026, MNRAS, 548, staf2109
Mascia S., Matthee J., Torralba A., Greene J. E., Eilers A.-C., Iani E., Naidu R. P., 2026, arXiv e-prints, p. arXiv:2608.25021
Matthee J., et al., 2024, ApJ, 963, 129
Matthee J., et al., 2026, arXiv e-prints, p. arXiv:2603.17667
Matthews J. H., et al., 2025, MNRAS, 536, 879
Mor R., Netzer H., 2012, MNRAS, 420, 526
Mor R., Trakhtenbrot B., 2011, ApJ, 737, L36
Muñoz Arancibia A. M., et al., 2023, A&A, 675, A85
Naidu R. P., et al., 2025, arXiv e-prints, p. arXiv:2503.16596
Naidu R. P., et al., 2026, arXiv e-prints, p. arXiv:2606.30711
Nandal D., Loeb A., 2026, ApJ, 998, 124
Nenkova M., Sirocky M. M., Nikutta R., Ivezić Ž., Elitzur M., 2008, ApJ, 685, 160
Nguyen H. T., et al., 2010, A&A, 518, L5
Nicholls D. C., Sutherland R. S., Dopita M. A., Kewley L. J., Groves B. A., 2017, MNRAS, 466, 4403

Nikopoulos G. P., Watson D., Sneppen A., Rusakov V., Heintz K. E., Witstok J., Brammer G., 2026, A&A, 710, A136
Noll S., Burgarella D., Giovannoli E., Buat V., Marcillac D., Muñoz-Mateos J. C., 2009, A&A, 507, 1793
Oke J. B., Gunn J. E., 1983, ApJ, 266, 713
Pacucci F., Narayan R., 2024, ApJ, 976, 96
Pacucci F., Nguyen B., Carniani S., Maiolino R., Fan X., 2023, ApJ, 957, L3
Park K., Torralba A., Matthee J., Mascia S., Haiman Z., Naidu R. P., de Graaff A., 2026, arXiv e-prints, p. arXiv:2605.14233
Pérez-González P. G., et al., 2024, ApJ, 968, 4
Pérez-González P. G., et al., 2026, arXiv e-prints, p. arXiv:2602.20247
Perrin M. D., Sivaramakrishnan A., Lajoie C.-P., Elliott E., Pueyo L., Ravindranath S., Albert L., 2014, in Oschmann Jr. J. M., Clampin M., Fazio G. G., MacEwen H. A., eds, Society of Photo-Optical Instrumentation Engineers (SPIE) Conference Series Vol. 9143, Space Telescopes and Instrumentation 2014: Optical, Infrared, and Millimeter Wave. p. 91433X, doi:10.1117/12.2056689
Rawle T. D., et al., 2014, MNRAS, 442, 196
Rawle T. D., et al., 2016, MNRAS, 459, 1626
Rémy-Ruyer A., et al., 2014, A&A, 563, A31
Ricci C., et al., 2017, Nature, 549, 488
Richards G. T., et al., 2006, ApJS, 166, 470
Richardson W. H., 1972, Journal of the Optical Society of America (1917-1983), 62, 55
Rieke G. H., et al., 2015, PASP, 127, 584
Rieke M. J., et al., 2023, PASP, 135, 028001
Rieke G. H., et al., 2025, ApJ, 994, 35
Rinaldi P., et al., 2025, ApJ, 994, 86
Rodrigo C., Solano E., 2020, in XIV.0 Scientific Meeting (virtual) of the Spanish Astronomical Society. p. 182
Rodrigo C., Solano E., Bayo A., 2012, SVO Filter Profile Service Version 1.0, IVOA Working Draft 15 October 2012, doi:10.5479/ADS/bib/2012ivoa.rept.1015R
Runnoe J. C., Brotherton M. S., Shang Z., 2012, MNRAS, 426, 2677
Rusakov V., et al., 2026, Nature, 649, 574
Sánchez-Blázquez P., et al., 2006, MNRAS, 371, 703
Schlafly E. F., Finkbeiner D. P., 2011, ApJ, 737, 103
Scholtz J., et al., 2026, arXiv e-prints, p. arXiv:2603.22277
Secunda A., Somerville R. S., Jiang Y.-F., Greene J. E., Furtak L. J., Zitrin A., 2026, ApJ, 996, 6
Setton D. J., et al., 2025a, ApJ, 991, L10
Setton D. J., et al., 2025b, ApJ, 995, 118
Shajib A. J., Treu T., Melo A., Roberts-Borsani G., Knabel S., Cappellari M., Frieman J. A., 2025, A&A, 702, L12
Shakura N. I., Sunyaev R. A., 1973, A&A, 24, 337
Sneppen A., et al., 2026, arXiv e-prints, p. arXiv:2601.18864
Stalevski M., Fritz J., Baes M., Nakos T., Popović L. Č., 2012, MNRAS, 420, 2756
Stalevski M., Ricci C., Ueda Y., Lira P., Fritz J., Baes M., 2016, MNRAS, 458, 2288
Stanway E. R., Eldridge J. J., 2018, MNRAS, 479, 75
Steffen A. T., Strateva I., Brandt W. N., Alexander D. M., Koekemoer A. M., Lehmer B. D., Schneider D. P., Vignali C., 2006, AJ, 131, 2826
Storey P. J., Hummer D. G., 1995, MNRAS, 272, 41
Sturm M. R., Hayes B., Reines A. E., 2025, arXiv e-prints, p. arXiv:2501.09791
Suess K. A., et al., 2024, ApJ, 976, 101
Sun W. Q., et al., 2026, The Open Journal of Astrophysics, 9, 62505
Tananbaum H., et al., 1979, ApJ, 234, L9
Tang M., et al., 2026, arXiv e-prints, p. arXiv:2604.03563
Tee W. L., Fan X., Wang F., Yang J., 2025, ApJ, 983, L26
Temple M. J., Hewett P. C., Banerji M., 2021, MNRAS, 508, 737
Torralba A., et al., 2026a, A&A, 707, A75
Torralba A., et al., 2026b, ApJ, 1005, L37
Treiber H., et al., 2025, ApJ, 984, 93
Tristram K. R. W., et al., 2007, A&A, 474, 837
Trotta R., 2008, Contemporary Physics, 49, 71
Übler H., 2026, Nature Astronomy, 10, 1273
Vanden Berk D. E., et al., 2001, AJ, 122, 549
Vanden Berk D. E., et al., 2004, ApJ, 601, 692
Wang B., et al., 2025, ApJ, 984, 121
Williams C. C., et al., 2024, ApJ, 968, 34
Wright G. S., et al., 2023, PASP, 135, 048003
Yanagisawa H., et al., 2026, arXiv e-prints, p. arXiv:2601.06015
Yang G., et al., 2020, MNRAS, 491, 740
Yue M., Eilers A.-C., Ananna T. T., Panagiotou C., Kara E., Miyaji T., 2024, ApJ, 974, L26
Zhang S., et al., 2015, ApJ, 815, 113
Zhang H., Theule P., Buat V., Burgarella D., Pons E., Boquien M., 2026a, arXiv e-prints, p. arXiv:2606.14643
Zhang S., Liu B., Bromm V., Kühnel F., 2026b, ApJ, 1000, L19
da Cunha E., et al., 2013, ApJ, 766, 13
de Graaff A., et al., 2025a, A&A, 697, A189
de Graaff A., et al., 2025b, A&A, 701, A168
de Graaff A., et al., 2026, MNRAS, 551, stag1567

APPENDIX A: REMOVAL OF CONTAMINATING SOURCES

As discussed in Section 3.2, Ima-B is significantly contaminated by a foreground object located at a small projected separation from QSO1 ($\approx 1''$). We therefore developed a procedure to model and remove the contaminating emission before performing the photometric extraction. For consistency, the same procedure was applied to the cutouts of all three multiple images.

For each cutout, we first constructed a preliminary segmentation map using SEP (Barbary 2016) and estimated the local background after masking the detected sources. The background-subtracted image was then deconvolved using the Richardson–Lucy algorithm (Richardson 1972; Lucy 1974). We adopted filter-dependent PSFs generated with STPSF (Perrin et al. 2014) for the NIRCam and MIRI observations.

Before constructing the contaminant model, the pixels associated with QSO1 were identified from the segmentation map and replaced in the deconvolved image with values randomly drawn from source-free regions of the same cutout. This prevented emission from QSO1 from being included in the model of the contaminating sources. The resulting image was smoothed and reconvolved to obtain a model of the surrounding contaminating emission, which was then subtracted from the original background-subtracted cutout.

Figure A1 presents representative examples of this procedure. For each selected filter, we show the original background-subtracted cutout and the residual image.

APPENDIX B: COMBINATION OF THE MULTIPLE-IMAGE PHOTOMETRY

After correcting the photometry of each multiple image for its corresponding lensing magnification, we found approximately wavelength-independent normalisation offsets between the three reconstructed SEDs. As discussed in Section 3.2, we adopted Ima-C as the reference because it has the lowest magnification and is therefore expected to be less sensitive to uncertainties in the lens model.

For Ima-A and Ima-B, we determined a single multiplicative scaling factor, s_i, by minimising

$$\chi^2(s_i) = \sum_j \frac{\left(s_i f_{i,j} - f_{C,j}\right)^2}{s_i^2 \sigma_{i,j}^2 + \sigma_{C,j}^2}, \tag{B1}$$

where i denotes Ima-A or Ima-B, j identifies the photometric band,

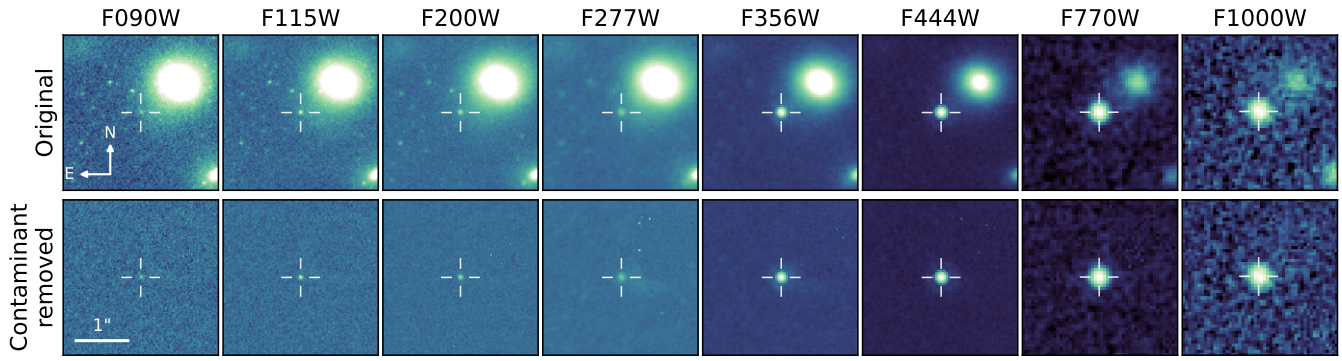


Figure A1. Examples of the contaminant-removal procedure applied to Ima-B of QSO1. The top panels show the original image cutouts for all NIRCam and MIRI wide bands available while the bottom panels show the corresponding residual images after the subtraction of all the models of nearby objects. The colourmap stretch and limits are kept consistent between top and bottom panels for each filter.

and $f_{i,j} = f_{i,j}^{\rm obs}/\mu_i$ and $\sigma_{i,j}$ are the de-magnified flux density and its uncertainty, respectively. The latter includes the uncertainty on the magnification, $\sigma_{i,j}^2 = (\sigma_{i,j}^{\rm obs}/\mu_i)^2 + (f_{i,j}\sigma_{\mu_i}/\mu_i)^2$, with $\mu_i \pm \sigma_{\mu_i}$ from the UNCOVER lens model v2 (Furtak et al. 2025). The same definition applies to Ima-C. Both the flux densities and their uncertainties were multiplied by the resulting scaling factors, while Ima-C was left unchanged. The scaling factors were constrained to be positive and were assumed to be independent of wavelength.

The final flux density in each band was calculated as the inverse-variance-weighted mean of the three rescaled measurements:

$$\overline{f}_{\nu,j} = \frac{\sum_i w_{i,j} f_{i,j}}{\sum_i w_{i,j}}, \qquad w_{i,j} = \frac{1}{\sigma_{i,j}^2}. \tag{B2}$$

The corresponding statistical uncertainty is

$$\sigma_{{\rm stat},j} = \left(\sum_i w_{i,j}\right)^{-1/2}. \tag{B3}$$

To account for any residual dispersion between the three multiple-image measurements, we additionally estimated a band-dependent systematic uncertainty. We first calculated the weighted inter-image variance,

$$S_j^2 = \frac{\sum_i w_{i,j}\left(f_{i,j} - \overline{f}_{\nu,j}\right)^2}{\sum_i w_{i,j}}. \tag{B4}$$

Part of this scatter is already expected from the statistical uncertainties of the individual measurements. We therefore defined the residual systematic variance as

$$\sigma_{{\rm sys},j}^2 = \max\left[0,\ S_j^2 - \frac{N-1}{\sum_i w_{i,j}}\right], \tag{B5}$$

where $N = 3$ is the number of multiple images. The final uncertainty associated with the combined photometry was then obtained by adding the statistical and systematic contributions in quadrature:

$$\sigma_{{\rm final},j} = \sqrt{\sigma_{{\rm stat},j}^2 + \sigma_{{\rm sys},j}^2}. \tag{B6}$$

Figure B1 shows the de-magnified photometry of the three images before and after applying the relative rescaling. The lack of a clear wavelength dependence in the original offsets supports the use of a single multiplicative factor for each multiple image. Following the rescaling, the individual measurements are consistent with the combined photometry within 3σ across the available passbands.

We report the observed photometry for the three individual multiple images of QSO1 and the magnification-corrected final stacked photometry in Table B1.

APPENDIX C: CONSTRUCTION AND PATH-LOSS CORRECTION OF THE NIRSPEC SPECTRUM

We combined the NIRSpec spectra obtained with the G140M/F100LP, G235M/F170LP, and G395M/F290LP configurations. Each spectrum was resampled onto a common wavelength grid extending from 0.8 to 5.6 μm, with a sampling of $\Delta\lambda = 0.005$ μm, using the flux-conserving `spectres` algorithm (Carnall 2017). At wavelengths covered by more than one configuration, the combined flux density was calculated as

$$f_\nu(\lambda) = \frac{\sum_k f_{\nu,k}(\lambda) w_k(\lambda)}{\sum_k w_k(\lambda)}, \qquad w_k(\lambda) = \frac{1}{\sigma_k^2(\lambda)}, \tag{C1}$$

where k denotes the grating–filter configuration. The corresponding uncertainty is

$$\sigma_{\rm spec}(\lambda) = \left[\sum_k w_k(\lambda)\right]^{-1/2}. \tag{C2}$$

Only spectral elements with finite and positive uncertainties were included in the combination.

For each configuration, we also calculated the wavelength-dependent resolving power using the instrumental line-spread-function parameterisation presented by Shajib et al. (2025). The resulting resolution curves were interpolated onto the common wavelength grid and combined according to the relative inverse-variance contribution of the individual spectra. This provided an effective spectral-resolution curve that accounts for the transitions and overlaps between the three configurations.

We corrected for residual wavelength-dependent path losses by comparing the combined NIRSpec spectrum with the photometry derived in Section 3.2. We retrieved the NIRCam filter-transmission

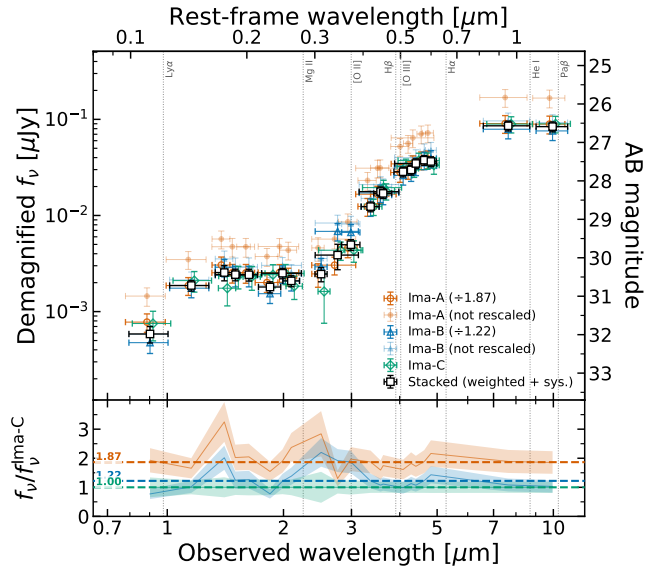


Figure B1. Comparison of the de-magnified photometry obtained from the three multiple images of QSO1 Ima-A (orange), Ima-B (blue) and Ima-C (green). For Ima-A and Ima-B we show the photometry before and after rescaling it for the wavelength-independent ratios $f_{\rm Ima-A}/f_{\rm Ima-C} = 1.87$ and $f_{\rm Ima-B}/f_{\rm Ima-C} = 1.22$. We also show the final inverse-variance-weighted photometry (white squares).

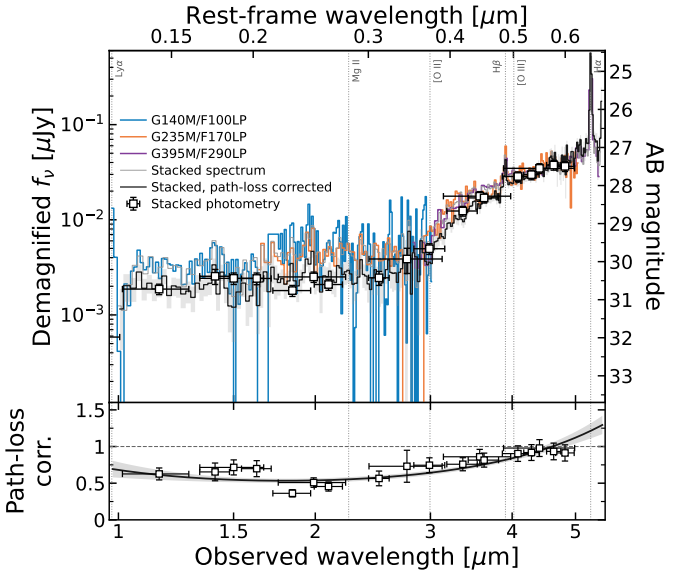


Figure B2. Spectrophotometric correction of the combined NIRSpec spectrum. Top: comparison between the combined photometry, the individual grating spectra, the stacked NIRSpec spectrum and the spectrum after applying the wavelength-dependent correction. Bottom: ratio between the imaging and synthetic photometry as a function of observed wavelength. The solid line shows the best-fitting second-order polynomial, while the shaded region represents the 1σ uncertainty derived from the Monte Carlo realisations.

curves from the SVO FPS (Rodrigo et al. 2012; Rodrigo & Solano 2020). For a spectrum expressed in terms of f_ν, we calculated the synthetic flux density in each passband as

$$f_{\nu,{\rm syn},j} = \frac{\int f_\nu(\lambda) T_j(\lambda) \frac{{\rm d}\lambda}{\lambda}}{\int T_j(\lambda) \frac{{\rm d}\lambda}{\lambda}}, \tag{C3}$$

where $T_j(\lambda)$ is the transmission curve of filter j. Only filters sufficiently covered by the NIRSpec spectrum were included.

The uncertainty on the synthetic photometry was propagated from the uncertainties of the spectral elements contributing to the convolution. We then calculated the ratio

$$C_j = \frac{f_{\nu,{\rm phot},j}}{f_{\nu,{\rm syn},j}}, \tag{C4}$$

where $f_{\nu,{\rm phot},j}$ is the combined imaging photometry. The uncertainty on this ratio includes both the photometric and spectroscopic contributions:

$$\sigma_{C,j} = C_j \sqrt{\left(\frac{\sigma_{{\rm phot},j}}{f_{\nu,{\rm phot},j}}\right)^2 + \left(\frac{\sigma_{{\rm syn},j}}{f_{\nu,{\rm syn},j}}\right)^2}. \tag{C5}$$

We modelled the wavelength dependence of the photometric-to-synthetic flux-density ratios with a second-order polynomial in logarithmic space:

$$\log_{10} C(\lambda) = a_0 + a_1 \log_{10}\lambda + a_2 \left(\log_{10}\lambda\right)^2. \tag{C6}$$

The fit was weighted using the uncertainties given by Eq. (C5). The corrected spectrum was then obtained as

$$f_{\nu,{\rm corr}}(\lambda) = C(\lambda) f_{\nu,{\rm spec}}(\lambda). \tag{C7}$$

Because the constant coefficient a_0 sets the absolute normalisation of the correction, the procedure simultaneously corrects for a wavelength-independent offset between the normalisation of the input spectrum and that of the de-magnified photometry. Consequently, the final spectrum is tied directly to the absolute normalisation of the combined photometric SED, whereas the higher-order terms describe the wavelength-dependent component of the path losses.

We estimated the uncertainty associated with the correction through 1000 Monte Carlo realisations. For each realisation, the values of $\log_{10} C_j$ were perturbed according to their uncertainties and the second-order polynomial was refitted. The standard deviation of the resulting correction curves was adopted as the wavelength-dependent uncertainty $\sigma_C(\lambda)$. The final uncertainty on the corrected spectrum was calculated as

$$\sigma_{\rm corr}(\lambda) = \sqrt{\left[C(\lambda)\sigma_{\rm spec}(\lambda)\right]^2 + \left[f_{\nu,{\rm spec}}(\lambda)\sigma_C(\lambda)\right]^2}. \tag{C8}$$

Figure B2 shows the photometric-to-synthetic flux-density ratios and the best-fitting correction curve. The comparison between the corrected synthetic photometry and the observed imaging measurements provides a direct assessment of the consistency of the final spectrophotometric calibration.

APPENDIX D: POINT-SPREAD FUNCTIONS

Testing whether QSO1 is resolved in MIRI requires a PSF accurate on the scale of the core ($r \lesssim 0.3''$). A default STPSF model is inadequate, as it is computed for a single pointing and field position, sampled on native detector pixels and oriented along the detector axes, and therefore ignores how the dithered exposures were combined into our mosaics. We built an "ad-hoc" effective PSF for each lensed image (A, B, C) and filter (F770W, F1000W), reproducing the construction of the mosaics: 20 exposures per filter combined with the JWST pipeline `resample` step (v1.20; `ivm` weighting, square

Table B1. Photometry of QSO1. All flux densities are corrected for Galactic extinction using $f_{\rm ext}$ ($E(B-V) = 0.0112$, Gordon et al. 2023 curve). Ima-A, Ima-B and Ima-C fluxes are not corrected for lensing magnification. The MIRI aperture corrections use the in-flight encircled-energy curves of the CRDS reference files (Section 3.2). The stacked photometry is de-magnified with the magnifications of the UNCOVER lens model v2 (Furtak et al. 2025), including their uncertainties, and normalised to Ima-C (Section 3.2 and Appendix B). The HST and ALMA reported upper-limits correspond to a 3σ limit. The MIPS and PACS limits are the mean 3σ depths of the Abell 2744 imaging, while the SPIRE values take into account confusion limits (Rawle et al. 2014; Nguyen et al. 2010). For both Spitzer and Herschel's upper-limits, we assumed independent and uniform image-plane noise. The stacked upper limits were obtained by taking one third of each 3σ depth as the 1σ uncertainty, de-magnifying and rescaling it to Ima-C as for the detections, and combining the three in inverse variance. For SPIRE, confusion noise is correlated over the beam, so the stacked limits are approximate.

Instrument	Filter	$f_{\rm ext}$	Ima-A		Ima-B		Ima-C		Stacked	
			$\mu \cdot f_\nu$ [μJy]	$\mu \cdot \mathrm{err}_{f_\nu}$ [μJy]	$\mu \cdot f_\nu$ [μJy]	$\mu \cdot \mathrm{err}_{f_\nu}$ [μJy]	$\mu \cdot f_\nu$ [μJy]	$\mu \cdot \mathrm{err}_{f_\nu}$ [μJy]	f_ν [μJy]	err_{f_ν} [μJy]
HST/WFC3_UVIS	F225W	1.091	< 0.041	–	< 0.045	–	< 0.034	–	< 0.00304	–
HST/WFC3_UVIS	F275W	1.070	< 0.027	–	< 0.029	–	< 0.024	–	< 0.00197	–
HST/WFC3_UVIS	F336W	1.054	< 0.012	–	< 0.013	–	< 0.012	–	< 0.00092	–
HST/ACS_WFC	F435W	1.043	< 0.005	–	< 0.006	–	< 0.005	–	< 0.00042	–
HST/ACS_WFC	F606W	1.031	< 0.005	–	< 0.006	–	< 0.005	–	< 0.00036	–
JWST/NIRCam	F070W	1.023	< 0.004	–	< 0.004	–	< 0.004	–	< 0.00027	–
HST/ACS_WFC	F814W	1.019	< 0.004	–	< 0.005	–	< 0.004	–	< 0.00030	–
JWST/NIRCam	F090W	1.016	0.008	0.001	0.004	0.0005	0.002	0.001	0.00059	0.00011
JWST/NIRCam	F115W	1.010	0.019	0.001	0.016	0.001	0.006	0.001	0.00187	0.00023
JWST/NIRCam	F140M	1.007	0.031	0.002	0.026	0.001	0.005	0.001	0.00255	0.00046
JWST/NIRCam	F150W	1.006	0.026	0.002	0.022	0.003	0.006	0.001	0.00242	0.00034
JWST/NIRCam	F162M	1.005	0.025	0.002	0.022	0.003	0.006	0.001	0.00242	0.00034
JWST/NIRCam	F182M	1.004	0.020	0.001	0.014	0.001	0.007	0.001	0.00180	0.00024
JWST/NIRCam	F200W	1.004	0.026	0.001	0.023	0.001	0.007	0.001	0.00251	0.00031
JWST/NIRCam	F210M	1.004	0.024	0.001	0.019	0.001	0.005	0.001	0.00209	0.00028
JWST/NIRCam	F250M	1.003	0.025	0.005	0.027	0.003	0.004	0.002	0.00246	0.00041
JWST/NIRCam	F277W	1.002	0.031	0.001	0.063	0.003	0.012	0.001	0.00387	0.00114
JWST/NIRCam	F300M	1.002	0.046	0.002	0.061	0.003	0.012	0.002	0.00496	0.00064
JWST/NIRCam	F335M	1.002	0.125	0.006	0.113	0.006	0.033	0.002	0.01237	0.00144
JWST/NIRCam	F356W	1.001	0.168	0.008	0.157	0.008	0.053	0.003	0.01770	0.00207
JWST/NIRCam	F360M	1.001	0.169	0.008	0.149	0.007	0.048	0.002	0.01698	0.00198
JWST/NIRCam	F410M	1.001	0.282	0.014	0.239	0.012	0.087	0.004	0.02851	0.00334
JWST/NIRCam	F430M	1.001	0.303	0.015	0.261	0.013	0.083	0.004	0.02979	0.00348
JWST/NIRCam	F444W	1.001	0.347	0.017	0.300	0.015	0.101	0.005	0.03474	0.00406
JWST/NIRCam	F460M	1.001	0.381	0.019	0.345	0.017	0.101	0.005	0.03761	0.00439
JWST/NIRCam	F480M	1.001	0.390	0.019	0.358	0.018	0.090	0.005	0.03647	0.00429
JWST/MIRI	F770W	1.001	0.911	0.046	0.723	0.036	0.241	0.012	0.08570	0.01002
JWST/MIRI	F1000W	1.002	0.899	0.045	0.694	0.035	0.243	0.015	0.08404	0.00991
Spitzer/MIPS	24μm	-	< 53	-	< 53	-	< 53	-	< 3.82	-
Herschel/PACS	100μm	-	< 2600	-	< 2600	-	< 2600	-	< 187	-
Herschel/PACS	160μm	-	< 5200	-	< 5200	-	< 5200	-	< 374	-
Herschel/SPIRE	250μm	-	< 16800	-	< 16800	-	< 16800	-	< 1209	-
Herschel/SPIRE	350μm	-	< 19200	-	< 19200	-	< 19200	-	< 1382	-
Herschel/SPIRE	500μm	-	< 19800	-	< 19800	-	< 19800	-	< 1425	-
ALMA	Band 6	-	< 94.5	-	< 90.9	-	< 84.0	-	< 6.7	-

kernel, `pixfrac` = 1, 0.06″ pixels), then reprojected onto a north-up grid aligned to NIRCam.

For every exposure covering the source with valid pixels (10, 13 and 11 exposures for images A, B and C), we computed an STPSF (v2.0.0) model at the detector position of the source, including the sub-pixel phase, geometric distortion and MIRI detector effects (`DET_DIST` product), for a blackbody spectrum of $T = 4470\ \mathrm{K}/(1+z) = 556$ K (see Figure 2). Each model was inserted into a copy of its exposure, preserving the original masks and variance, and all copies were resampled with the mosaic parameters onto a 0.06″ grid centred on the source and normalised to unit flux. Weights are thus those of the real data (effectively exposure-time weights, as all exposures are identical).

We validated the procedure on an unsaturated field star (RA = 3.56893 deg, Dec = −30.40279 deg; 10 exposures per filter), rebuilding its PSF in the same way (Figure D1). As a reference, we also considered a default STPSF model including detector effects (`DET_DIST`), computed at the centre of the field and resampled onto the same grid. Both models reproduce the azimuthally averaged profile of the star, including the diffraction rings and the wings, but the ad-hoc PSF also matches its two-dimensional structure, i.e. the orientation of the hexagonal pattern and the centroid ($< 0.005''$), with residuals 5.4 (F770W) and 5.0 (F1000W) times smaller (χ^2) than the default model, whose single-pointing, native-pixel sampling leaves strong residuals in the core. The stellar core is nevertheless slightly broader than the ad-hoc PSF: convolving the latter with a Gaussian of $\sigma = 0.04''$ (F770W) and $0.05''$ (F1000W) reduces χ^2 by a further factor of ∼3. About one third of this excess is due to the final reprojection of the mosaic. We ascribe the rest to unmodelled detector effects (charge diffusion and possibly the brighter-fatter effect, which may affect the bright star more than QSO1). The input spectrum is irrelevant (FWHM changes ≤ 1% between 556 and 5000 K). As the true PSF of QSO1 should lie between the ad-hoc PSF and its broadened version, we performed all morphological fits with both

and regard a source extent as robust only if required in both cases (see Section 4.1).

For aperture photometry, the core broadening is negligible, but the encircled energy at the adopted radii (0.40–0.56″) depends on the PSF wings. We measured the growth curve of the field star out to 3″ and corrected it to infinite radius with the STPSF `DET_DIST` model (20″ field of view). At the adopted radii, the star encloses 65–73% of its flux, in agreement within 1.5% with the in-flight EE curves of the CRDS `apcorr` reference file (`jwst_miri_apcorr_0014`), which we adopted (Section 3.2). The STPSF `DET_DIST` model encloses 4–5% (F770W) and 3–4% (F1000W) more flux, and the STPSF model without detector effects ≈ 12% and 4–6% more, mostly because it lacks the detector scattering that moves light from the core to the wings, which is strongest at short wavelengths.

APPENDIX E: MIRI MORPHOLOGY

We modelled the three lensed images in the contaminant-removed F770W and F1000W mosaics with SOCCA[11] (Di Mascolo 2026), fitting 2.5″ × 2.5″ stamps centred on each image. The drizzled MIRI mosaics have correlated noise (the rms of 2 × 2-binned blank regions is ∼1.4 times the value expected for independent pixels). We therefore used a correlated Gaussian likelihood, with the pixel covariance taken from the empirical noise autocorrelation of each stamp, measured in pixels more than 1.5″ from QSO1. Each image and filter was fitted with its own ad-hoc PSF (Appendix D) and with the same PSF convolved with the Gaussian that best reproduces the field star (σ = 0.04″ and 0.05″ in F770W and F1000W; "broadened" PSF), the two bracketing the true PSF. We quantified any extension with a profile likelihood: for each image, filter and PSF we fitted a model of the PSF convolved with a circular Gaussian of width σ, optimising flux and centroid on a grid of σ = 0–0.10″, and derived 95% upper limits from $\Delta\chi^2 = 3.84$ relative to the best fit. As a cross-check, we computed Bayesian evidences ($\ln(\mathcal{B})$) for a point-source and a Gaussian model with NAUTILUS (Lange 2023). With the broadened PSF, all fits have $\sigma_{\rm best} = 0$ and residuals consistent with noise. With the ad-hoc PSF, the F770W fits of all three images and the F1000W fit of Ima-A prefer $\sigma \simeq 0.025$–0.035″ ($\Delta\chi^2$ = 18–72; $\ln(\mathcal{B}) \simeq$ 7–9 in favour of the Gaussian), an excess consistent with the PSF systematic discussed in Section 4.1.

We converted angular to physical sizes with the adopted cosmology (5.21 kpc arcsec^{-1} at z = 7.0364) and magnifications (Furtak et al. 2025), taking $r_{\rm e} \simeq$ FWHM/2 (Furtak et al. 2023). For Ima-A, Ma et al. (2025) provided the tangential magnification from the same lens model, $\mu_{\rm t}$ = 3.21, implying a radial magnification $\mu_{\rm r} = \mu_{\rm A}/\mu_{\rm t} \simeq 1.68$. A circular source of radius r is thus imaged into an ellipse with semi-axes $\mu_{\rm t} r$ and $\mu_{\rm r} r$. Since our circular model is sensitive to the root mean square of the two axes, we converted the image-plane limits of Ima-A as $r_{\rm src} = r_{\rm img}/[(\mu_{\rm t}^2 + \mu_{\rm r}^2)/2]^{1/2} = r_{\rm img}/2.56$. For Ima-B and Ima-C, for which no shear information was available, we assumed isotropic magnification ($r_{\rm src} = r_{\rm img}/\sqrt{\mu}$).

A first, model-independent bound follows from the angular resolution alone: with effective PSFs of FWHM ≃ 0.28″ (F770W) and 0.36″ (F1000W), an unresolved source must have $r_{\rm e} \lesssim 0.14''$ in F770W, i.e. ≲ 285, 270 and 445 pc in the source plane for Ima-A, B and C. The profile-likelihood fits improve on this by a factor of ∼4: with the ad-hoc PSF, the 95% limits on the intrinsic F770W FWHM are < 0.063″, < 0.073″ and < 0.11″ for Ima-A, B and C (F1000W gives weaker but consistent limits), corresponding to the radii quoted in Section 4.1. With the broadened PSF the best-fit width is $\sigma = 0$ in all fits and $\Delta\chi^2$ rises steeply from this boundary. The resulting limits ($r_{\rm e}$ < 18, 18 and 88 pc) reflect the mismatch between the broadened and the true PSF rather than a measurement, and we do not use them. Since the PSF uncertainty ($\sigma \approx$ 0.03–0.04″) exceeds the statistical one, the ad-hoc-PSF limits should be regarded as the effective resolution floor of these data. Dividing the image-plane size by $\mu_{\rm t}$ alone, as done by Furtak et al. (2024), would give $r_{\rm e}$ < 51 pc for Ima-A.

[11] https://github.com/lucadimascolo/socca

APPENDIX F: LINE CONTAMINATION AND CONTINUUM FITS

F1 Emission-line contribution to the MIRI bands

Both MIRI filters contain hydrogen and helium recombination lines: F770W covers the Paschen lines from Paδ to Pa10 (Paγ and HeI λ10830 fall at its red edge, where the throughput is ≈ 3% and ≈ 33% of the peak, respectively), while F1000W covers Paβ. To estimate their contribution, we adopted the broad and narrow Hα fluxes measured by D'Eugenio et al. (2026b) for Ima-A, rescaled to our combined photometry. For the narrow component, we assumed Case-B line ratios for $T = 10^4$ K (Storey & Hummer 1995) and no attenuation, consistent with the narrow-line Balmer decrement (D'Eugenio et al. 2026b). For the broad component, we applied the same Paschen-to-Hβ ratios to the Hα flux corrected for the attenuation inferred from the broad-line Balmer decrement ($A_{V,\rm b}$ = 2.9 ± 0.2 mag), adopting, as D'Eugenio et al. (2026b), the SMC-Bar extinction curve of Gordon et al. (2003) and an intrinsic broad-line Hα/Hβ = 3.1 (Dong et al. 2008), and re-attenuated each Paschen line accordingly. Folding each line through the filter transmission curves, the hydrogen lines contribute 1.9 ± 0.2% and $6.9^{+1.0}_{-0.8}$% of the F770W and F1000W flux densities, respectively, almost entirely from the broad component. For HeI λ10830, we used the HeI/Paγ ratios measured in LRDs by Kapoor et al. (2026), which are systematically lower (≈ 1.0–1.6) than those of normal type-1 AGN (> 2.3) and tentatively anti-correlate with the strength of the Balmer break, likely because of HeI self-absorption in high-column-density gas. With a Balmer break $f_\nu(4050\text{Å})/f_\nu(3650\text{Å}) \approx 2.5$, comparable to the strongest breaks in their sample, QSO1 is expected to have HeI/Pa$\gamma \approx$ 1.0–1.3, implying a further contribution of ≈ 0.8% to F770W (≲ 1.5% even for HeI/Paγ = 2.3). Possible HeI absorption would only lower it. In total, line emission accounts for ≈ 3% and ≈ 7% of the F770W and F1000W flux densities. These estimates are conservative: if the line contribution is instead scaled using the Hα equivalent width reported by D'Eugenio et al. (2026b), it decreases by a factor of ≈ 2.7. If the broad Balmer decrement is not due to dust, Case-B Paschen-to-Balmer ratios would lower it by a factor of ≈ 3–4. However, the Paschen lines of LRDs are boosted relative to Case B (Juodžbalis et al. 2024; Lin et al. 2026), as expected for dense gas in which the Balmer lines are optically thick. Our adopted ratios correspond to a broad Paβ/H$\alpha \approx 0.25$, about four times the Case-B value and comparable to the ratios observed in LRDs, so we adopt them independently of the origin of the decrement. After correcting for the line emission, the slope between the two MIRI filters becomes $\alpha = -0.2 \pm 0.4$.

F2 Degeneracies of the continuum fits

The blackbody temperature is degenerate with dust attenuation. A hotter, reddened blackbody provides a comparable description, e.g. $T_{\rm BB}$ = 6874 K with $A_V \simeq 1.5$ mag ($\chi^2_{\rm red} = 2.4$), assuming the

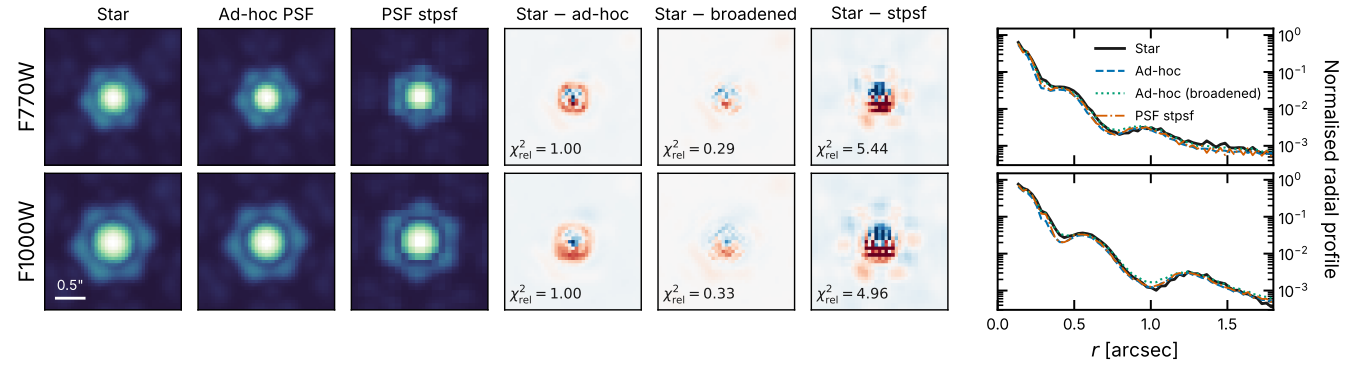


Figure D1. Validation of the MIRI ad-hoc PSFs on an unsaturated field star (top: F770W; bottom: F1000W). From left to right: the star in the mosaic, the ad-hoc PSF, the default STPSF PSF including detector effects (field centre, detector orientation, single pointing) and the residuals after fitting each model (and the ad-hoc PSF convolved with a Gaussian of $\sigma = 0.042''$ and $0.054''$, "broadened") to the star within $r < 1''$, shown within ±10% of the stellar peak. $\chi^2_{\rm rel}$ is relative to the ad-hoc PSF. Panels are $2.5''$ wide. Right: azimuthally averaged profiles normalised to the peak.

SMC-Bar extinction curve ($R_V = 2.74$, Gordon et al. 2003). The photometry alone cannot break this degeneracy: $\chi^2_{\rm red}$ increases only from 2.2 for an unreddened 4450 K blackbody to 2.4 and 2.7 for $T = 7000$ and 30000 K, with $A_V \approx 1.6$ and 3.3 mag, respectively. Similarly, a dust-reddened power law ($f_\nu \propto \lambda^\alpha 10^{-0.4A_\lambda}$) fitted to the same filters requires a steep intrinsic slope ($\alpha = -1.8$) and a large attenuation ($A_V \approx 3.6$ mag; $\chi^2_{\rm red} = 3.2$), whereas intrinsic slopes typical of type-1 AGN or of a standard accretion disc ($f_\nu \propto \nu^{-0.44}$ or $\nu^{1/3}$; Vanden Berk et al. 2001; Shakura & Sunyaev 1973, respectively) provide poor fits ($\chi^2_{\rm red} = 10.2$ and 5.9, respectively), as they cannot reproduce the turnover at $\approx 1\,\mu$m.

APPENDIX G: DUST ENERGY BUDGET

Absorbed luminosity. We refitted the AGN-only model of Section 4.3.1 (the Temple et al. 2021 continuum without emission lines and hot dust, attenuated with the Noll et al. 2009 curve with free A_V and δ, plus a free unattenuated scattered fraction) to the 18 NIRCam and MIRI bands, using the filter transmission curves. The fit recovers the parameters of Table H2 ($\log_{10}(\lambda L_{3000}\ [\mathrm{erg\ s^{-1}}]) = 44.22 \pm 0.04$, $A_V = 2.17^{+0.10}_{-0.08}$ mag, $\delta = -0.96^{+0.06}_{-0.03}$, scattered fraction $f_{\rm scat} = 0.010 \pm 0.001$, $\chi^2_{\rm red} = 1.70$). We sampled its posterior with EMCEE (Foreman-Mackey et al. 2013) and, for each sample, integrated the difference between the intrinsic and attenuated continuum between 912 Å and 2.9μm, obtaining $L_{\rm abs} = (3.9 \pm 0.3) \times 10^{44}$ erg s^{-1}. The ionising continuum is not included in the template. We extended it with the incident continuum of the accretion disc used in our cocoon models (Appendix I3), in which the range 912 Å–2.9μm carries 33.7% of the luminosity, giving $L_{\rm AGN} = (1.23^{+0.11}_{-0.10}) \times 10^{45}$ erg s^{-1}. Ionising photons are absorbed mainly by gas, especially at low metallicity, but are largely re-emitted as lines and recombination continua that are in turn absorbed by the dust. The upper value of $L_{\rm abs}$ therefore assumes complete reprocessing, while the lower value is independent of it. The bolometric correction of Runnoe et al. (2012), $L_{\rm bol} = 0.75 \times 5.15\ \lambda L_{3000}$, gives 6.4×10^{44} erg s^{-1}, and would give 9.6×10^{43} erg s^{-1} instead of 2.4×10^{44} erg s^{-1} for the disc of the cocoon with the stellar-mass limit. The ionising continuum of LRDs is not constrained by observations, so this factor of $\approx$ 2–2.5 is a systematic uncertainty on all intrinsic luminosities.

Hot dust (NIRCam and MIRI). We added to the AGN model an optically thin greybody, $L_\nu \propto \nu^\beta B_\nu(T_{\rm d})$ with $\beta = 0$, 1 and 2, at fixed $T_{\rm d}$, and computed the profile likelihood of its normalisation, re-optimising all AGN parameters at each step. Since F770W and F1000W are detections, we quote these limits at $\Delta\chi^2 = 1$ (1σ) relative to the fit without dust, whereas the far-infrared and millimetre limits are the 3σ upper limits of the non-detections. The limits are converted to luminosities by integrating the greybody over all frequencies.

Cold and warm dust (far-infrared and millimetre). For the MIPS, PACS, SPIRE and ALMA bands, we normalised a greybody with $\beta = 1.8$ to the stacked 3σ limit of each band (Table B1), dividing by the CMB contrast factor $1 - B_\nu(T_{\rm CMB}(z))/B_\nu(T_{\rm d})$ (da Cunha et al. 2013), and adopted the most constraining band at each temperature. Here $T_{\rm d}$ is the dust temperature at $z = 7.04$, including any CMB heating. ALMA dominates below $T_{\rm d} \approx 120$ K, *Herschel*/PACS between ≈ 130 and 350 K and MIPS above.

Table G1. Upper limits on the luminosity of dust emission at a single temperature, in units of 10^{43} erg s^{-1}: 1σ for the NIRCam and MIRI detections and 3σ for the far-infrared and millimetre non-detections.

$T_{\rm d}$ [K]	$\beta = 0$	$\beta = 1$	$\beta = 1.8$	$\beta = 2$
NIRCam+MIRI, joint fit with the reddened-disc model (1σ)				
500	1.3×10^4	2200	640	480
600	640	130	44	35
700	82	20	7.5	6.0
800	19	5.1	2.2	1.8
900	6.3	1.9	0.89	0.75
1000	2.7	0.92	0.46	0.40
1200	0.86	0.35	0.20	0.18
1500	0.31	0.16	0.11	0.10
2000	0.15	0.10	0.096	0.097
MIPS, *Herschel* and ALMA (3σ)				
30	2.0	2.4	3.3	3.6
40	2.1	3.4	5.9	6.9
50	2.9	5.7	12	14
80	7.1	23	68	92
100	12	48	170	240
150	33	200	480	440
200	72	420	360	350
300	220	440	510	540
400	500	510	240	210
500	350	140	77	68
600	140	66	44	40
800	58	36	30	29

APPENDIX H: COMPARISON WITH PREVIOUS CONTINUUM MODELS

We reproduced the three model families of Ma et al. (2025) with their ingredients: FSPS (Conroy et al. 2009) stellar populations (MIST, Choi et al. 2016; Dotter 2016; MILES, Sánchez-Blázquez et al. (2006); Chabrier 2003 IMF $\log_{10}(Z\ [Z_\odot]) = -1$; delayed-$\tau$ history; nebular continuum), the line-free Temple et al. (2021) quasar continuum with or without its hot-dust component, and the Noll et al. (2009) attenuation law, with unattenuated fractions $f_{\rm nodust}$ (stars) and $f_{\rm scat}$ (AGN-only). In the AGN+galaxy model, the AGN is attenuated by $A_V^{\rm gal} + A_V^{\rm AGN}$.

We first rebuilt their best-fitting models from their Table 2, with $\delta = -1$. They reproduce the quoted A_{1500}/A_V (9.4; effective 2.1) and the broad-line Balmer decrement (11.4) and their components within ≈ 0.05 dex. Each model was rescaled by a single factor fitted to the NIRCam continuum (F115W–F480M, excluding F410M and F444W), which removes the 0.27 dex offset between their normalisation ($\mu_{\rm A} = 5.4$, Ima-A) and ours. The galaxy-only and AGN+galaxy models over-predict both MIRI bands by 23–60% (Table H1, Figure H1). The AGN-only model is within 8% without hot dust, but over-predicts F1000W by a factor of ≈ 1.9 with hot dust. As Ma et al. (2025) fitted only up to rest-frame 0.66μm, these are predictions of their models, not failures of their fits.

We then refitted the same families to our stacked photometry with NAUTILUS (Lange 2023), using 1000 live points and an effective sample size of 10^4. The fits use the 16 NIRCam bands from F115W to F480M (excluding F410M and F444W), with or without F770W and F1000W, and uniform priors as in Ma et al. (2025) (Table H2, Figures 4 and H2). Fitted to NIRCam alone, the posteriors recover their solutions. For example, $A_V = 2.21^{+0.49}_{-0.29}$ mag (galaxy-only) and $2.41^{+0.25}_{-0.18}$ mag (AGN-only), compared with their 2.12 mag and 2.08 mag. All of these fits over-predict MIRI, so the tension is not limited to the published best fits. With MIRI, the models without hot dust match F770W and F1000W within 13%, but only with a different optical solution: the galaxy-only model needs lower attenuation ($A_V = 1.79^{+0.12}_{-0.11}$ mag) and $\log_{10}(M_\star\ [\mathrm{M}_\odot]) = 9.33^{+0.10}_{-0.09}$, while the AGN+galaxy posterior is bimodal, between an AGN-dominated mode with a minor stellar component ($\log_{10}(M_\star\ [\mathrm{M}_\odot]) \approx 7.5$–8) and the galaxy-only solution, with medians $\log_{10}(\lambda L_{3000}\ [\mathrm{erg\ s^{-1}}]) = 44.17^{+0.06}_{-0.82}$ and $\log_{10}(M_\star\ [\mathrm{M}_\odot]) = 8.21^{+1.06}_{-0.70}$. These two have similar evidence ($\Delta\ln(\mathcal{Z}) = -0.7$), while AGN-only is disfavoured ($\Delta\ln(\mathcal{Z}) = -5.4$). The hot-dust component of the Temple et al. (2021) template is disfavoured. The AGN-only model with hot dust is rejected ($\Delta\ln(\mathcal{Z}) = -19.5$, $\chi^2_{\rm red} = 3.66$). In the AGN+galaxy model with hot dust, the AGN is suppressed by ≈ 1.2 dex, so that the model reverts to galaxy-only ($\Delta\ln(\mathcal{Z}) = -2.4$). Fitted to NIRCam alone, the hot-dust models over-predict F1000W by up to a factor of 2.8. Fitted to NIRCam and MIRI, the galaxy-only and AGN+galaxy models are statistically acceptable ($\chi^2_{\rm red} = 0.94$ and 1.20), whereas the AGN-only model is not as good ($\chi^2_{\rm red} = 1.70$). All place δ close to the lower edge of its prior (-1). Removing the line contribution to MIRI (Section 4.2) would only increase the tension with the NIRCam-only fits.

H1 Comparison with accretion-flow envelope models

We used the 15 public continuum spectra of Liu et al. (2025), computed for luminosities $L = L_{\rm Edd}(10^l\ \mathrm{M}_\odot)$ with $l = 5, 6, 7$ and five reference densities $\rho_{\rm ref}$ for each l, over rest-frame 1250–13000 Å. We interpolated them linearly in $\log L_\nu$ over $(l, \log\rho_{\rm ref} - 0.5\,l)$, as in the notebook released by the authors, and extrapolated beyond

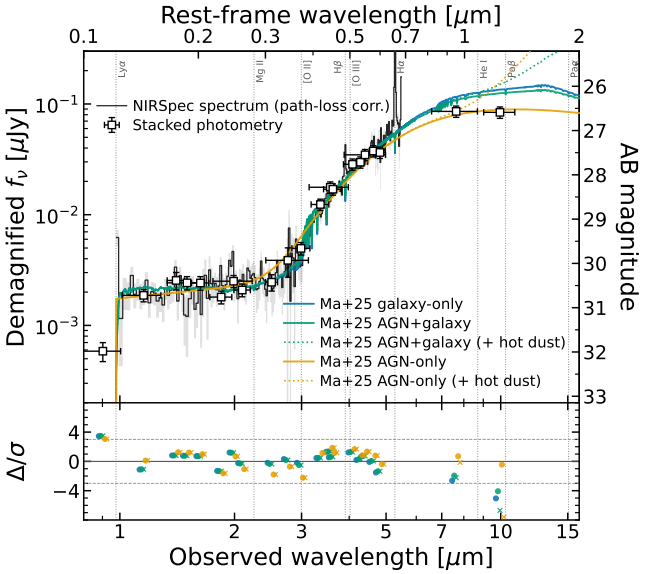


Figure H1. Best-fitting continuum models of Ma et al. (2025), rebuilt from their Table 2 and extended to the MIRI bands, compared with the stacked photometry (white squares) and the NIRSpec spectrum (black) of QSO1. Each model is rescaled by a single factor fitted to the NIRCam continuum bands (F115W–F480M, excluding F410M and F444W). Dotted lines include the hot-dust component of the Temple et al. (2021) quasar template. Unlike Figure 4, we show here the published solutions, not refits to our photometry. Bottom panel: residuals, $(f_{\rm obs} - f_{\rm model})/\sigma$, of the synthetic photometry of each model.

1.3μm with a power law, which affects F1000W by $\leq 1\%$. The models contain no emission lines and no flux below ≈ 2500 Å, so we added a power law for the UV continuum. We fitted the stacked photometry from F115W to F1000W (excluding F410M and F444W) with the photometric uncertainties, on a grid of l, $\rho_{\rm ref}$ and UV slope, solving for the two normalisations. The shape fixes $\log\rho_{\rm ref} - 0.5\,l \approx -14.75 \pm 0.05$, while l is degenerate with the normalisation. The solution whose luminosity matches the data without rescaling has $l \approx 5.2$ and $\rho_{\rm ref} \approx 10^{-12}$ g cm^{-3}.

APPENDIX I: SED MODELLING

I1 Stellar populations and stellar-ionised gas

For the stellar populations, we adopted the binary BPASS v. 2.2 models (Eldridge et al. 2017; Stanway & Eldridge 2018), with a Chabrier-like initial mass function extending to 300 $\mathrm{M}_\odot$, and stellar metallicities of 0.05, 0.5, 5 and 10% $Z_\odot$, bracketing the very low gas-phase metallicity of QSO1 (Maiolino et al. 2026). Each stellar population had a free formed mass ($\log_{10}(M_\star\ [\mathrm{M}_\odot]) \in [3, 12]$, or $[3, 7.5]$ in the test with the stellar-mass limit), its own colour excess and an age chosen from the native BPASS grid. In the family with two ordinary-density populations, both ages were drawn from $\log_{10}(t\ [\mathrm{Myr}]) = 0.0$–2.2 (1–160 Myr), with the second population older than the first. In the dense-gas families, both populations could take any age in the same range, without ordering. In the cocoon families a single stellar population in the same age range was combined with the AGN component (Appendix I3).

Each BPASS spectrum was then used as ionising source for a grid of CLOUDY (v25.00) photoionisation models to estimate the corre-

Table H1. Predicted-to-observed MIRI flux-density ratios for the best-fit continuum models of Ma et al. (2025), rebuilt from their best-fit parameters. Each model is rescaled by a single factor, either fitted to the NIRCam continuum bands (F115W–F480M, excluding F410M and F444W; "global") or matched to F480M. Numbers in parentheses give the deviation in units of the photometric uncertainty. Models labelled "+ hot dust" include the default hot-dust component of the Temple et al. (2021) quasar template.

Model	global		F480M-matched	
	F770W	F1000W	F770W	F1000W
Galaxy-only	1.31 (-2.6σ)	1.60 (-5.1σ)	1.11 (-0.9σ)	1.35 (-3.0σ)
AGN+galaxy	1.23 (-1.9σ)	1.48 (-4.1σ)	1.06 (-0.5σ)	1.28 (-2.4σ)
AGN+galaxy + hot dust	1.26 (-2.2σ)	1.79 (-6.7σ)	1.09 (-0.8σ)	1.55 (-4.6σ)
AGN-only	0.92 ($+0.7\sigma$)	1.05 (-0.5σ)	0.88 ($+1.0\sigma$)	1.01 (-0.1σ)
AGN-only + hot dust	1.02 (-0.1σ)	1.89 (-7.6σ)	0.97 ($+0.2\sigma$)	1.81 (-6.9σ)

Table H2. Posterior constraints for the Ma et al. (2025) model families fitted to the stacked photometry of QSO1, without and with the MIRI bands. Values are posterior medians with 16th–84th percentile ranges. Stellar masses and luminosities are de-magnified with the Ima-C-anchored stack adopted here (UNCOVER lens model v2, Furtak et al. 2025). They are 0.27dex lower than in the Ma et al. (2025) normalisation ($\mu_{\rm A} = 5.4$). $M_\star$ is the surviving stellar mass in $M_\odot$ and λL_{3000} is in ergs^{-1}. $\chi^2_{\rm red} = \chi^2_{\rm min}/(N_{\rm bands} - N_{\rm par})$ of the maximum-likelihood model, with $N_{\rm bands} = 16$ (NIRCam) or 18 (NIRCam+MIRI) and $N_{\rm par} = 6$, 8 and 4 for the galaxy-only, AGN+galaxy and AGN-only families. $\Delta\ln(\mathcal{Z})$ is the log-evidence relative to the best model fitted to the same bands, and values for different band sets are not comparable. The last two columns give the predicted-to-observed MIRI flux ratios (for the NIRCam-only fits, these are extrapolations).

Model	$\Delta\ln(\mathcal{Z})$	$\chi^2_{\rm red}$	$\log_{10} M_\star$	$A_V^{\rm gal}$	$\log_{10} \lambda L_{3000}$	$A_V^{\rm AGN}$	F770W pred/obs	F1000W pred/obs
Fit to NIRCam only (F115W–F480M)								
Galaxy-only	+0.0	0.91	$9.56^{+0.21}_{-0.16}$	$2.21^{+0.49}_{-0.29}$	–	–	$1.27^{+0.28}_{-0.20}$	$1.62^{+0.49}_{-0.33}$
AGN+galaxy	−0.7	1.19	$8.30^{+0.95}_{-0.56}$	$1.81^{+0.59}_{-0.85}$	$44.42^{+0.29}_{-0.20}$	$1.37^{+1.13}_{-0.88}$	$1.36^{+0.42}_{-0.25}$	$1.76^{+0.84}_{-0.42}$
AGN+galaxy (+hot dust)	−0.7	1.16	$8.39^{+0.94}_{-0.60}$	$1.86^{+0.54}_{-0.82}$	$44.38^{+0.29}_{-0.32}$	$1.34^{+1.11}_{-0.87}$	$1.44^{+0.40}_{-0.23}$	$2.78^{+1.36}_{-0.75}$
AGN-only	−5.9	1.77	–	–	$44.35^{+0.11}_{-0.09}$	$2.41^{+0.25}_{-0.18}$	$1.18^{+0.20}_{-0.15}$	$1.43^{+0.30}_{-0.21}$
AGN-only (+hot dust)	−5.9	1.77	–	–	$44.35^{+0.12}_{-0.09}$	$2.41^{+0.28}_{-0.18}$	$1.33^{+0.22}_{-0.17}$	$2.62^{+0.57}_{-0.40}$
Fit to NIRCam + MIRI (F115W–F1000W)								
Galaxy-only	+0.0	0.94	$9.33^{+0.10}_{-0.09}$	$1.79^{+0.12}_{-0.11}$	–	–	$0.95^{+0.06}_{-0.06}$	$1.13^{+0.08}_{-0.09}$
AGN+galaxy	−0.7	1.20	$8.21^{+1.06}_{-0.70}$	$1.61^{+0.29}_{-0.78}$	$44.17^{+0.06}_{-0.82}$	$1.00^{+0.98}_{-0.66}$	$0.96^{+0.06}_{-0.06}$	$1.13^{+0.09}_{-0.08}$
AGN+galaxy (+hot dust)	−2.4	1.20	$9.30^{+0.10}_{-0.10}$	$1.75^{+0.12}_{-0.12}$	$43.00^{+0.28}_{-0.19}$	$2.42^{+1.81}_{-1.65}$	$0.93^{+0.06}_{-0.06}$	$1.16^{+0.08}_{-0.08}$
AGN-only	−5.4	1.70	–	–	$44.22^{+0.04}_{-0.04}$	$2.17^{+0.10}_{-0.09}$	$0.97^{+0.06}_{-0.06}$	$1.13^{+0.09}_{-0.08}$
AGN-only (+hot dust)	−19.5	3.66	–	–	$44.03^{+0.03}_{-0.03}$	$1.86^{+0.07}_{-0.07}$	$0.76^{+0.05}_{-0.04}$	$1.38^{+0.09}_{-0.09}$

Note. For AGN+galaxy, $A_V^{\rm AGN}$ is the additional attenuation of the AGN on top of $A_V^{\rm gal}$, as in Ma et al. (2025). For AGN-only, it is the total attenuation. The Noll et al. slope δ lies close to the lower edge of its prior ($\delta \simeq -0.8$ to -1) in all fits. In the AGN+galaxy fits, the posteriors are broad or bimodal, and the quoted ranges span both the galaxy- and the AGN-dominated solutions.

sponding nebular emission. The BPASS models were set in a spherical, ionisation-bounded, dust-free cloud (calculation stopped at an electron fraction of 1%) with gas-phase metallicity tied to the stellar metallicity via the Galactic-concordance abundance pattern of Nicholls et al. (2017). The grid spanned $\log_{10}(n_{\rm H}\ [{\rm cm}^{-3}]) = 0.5$–12 and $\log_{10}(U) = -4$ to -1 in steps of 0.5 dex, and stored the transmitted stellar light $F_{\rm trans}$, the diffuse nebular continuum $F_{\rm diffuse}$ and the absolute luminosities of the main emission lines $F_{\rm lines}$.

During fitting, each SSP was assigned a covering fraction C_f such that its overall emission was $(1 - C_f)\ F_{\rm BPASS} + C_f\ (F_{\rm trans} + F_{\rm diffuse} + F_{\rm lines})$. In addition, stellar age and the pair $(\log_{10}(n_{\rm H}), \log_{10}(U))$ were kept as discrete parameters and no interpolation across the grid was performed. Nodes spanning both ordinary ($\log_{10}(n_{\rm H}) \leq 6$) and dense ($\log_{10}(n_{\rm H}) \geq 6.5$) gas were computed. Ordinary-density populations were restricted to the former and had a free covering fraction. In the dense-gas families (class ii in Section 4.3.2), the second population was restricted to the dense nodes, where forbidden lines are collisionally suppressed and the emission is dominated by permitted lines and by the Balmer continuum and absorption. Its covering fraction was free, and its lines had their own velocity dispersion, $\sigma_{v,\rm dense} \in [0, 3000]$ km s^{-1}, independent of that of the ordinary-density gas ($\sigma_v \in [20, 500]$ km s^{-1}). For emission lines in the range covered by the NIRSpec spectrum, we integrated them exactly over each pixel using a Gaussian of width equal to the quadrature sum of the fitted intrinsic velocity dispersion and the instrumental dispersion at the line wavelength.

I2 Dust attenuation and emission

The stellar light and its nebular emission were attenuated with the Calzetti et al. (2000) law, extended to the Lyman limit following Leitherer et al. (2002). The dust screen carried a free slope offset, $A_\lambda \propto E(B-V)\ k(\lambda)\ (\lambda/0.55\ \mu{\rm m})^\delta$, with $\delta \in [-1, 0.4]$, to permit steeper or shallower (*greyer*) attenuation laws (e.g. Noll et al. 2009). In the families with independent attenuation, each component (each stellar population with its nebular emission, or the AGN cocoon) had its own colour excess. In the shared-screen families, all components were placed behind a single foreground screen with a common $E(B-V)$ and δ. Re-emission by dust was modelled with a modified blackbody including CMB heating and the CMB contrast at $z = 7.04$ (da Cunha et al. 2013), plus a fixed-shape polycyclic aromatic hydrocarbons (PAH) template (Drude profiles, including the 3.3 and 3.4μm features) with a free total luminosity. The intrinsic dust temperature had a log-uniform prior, $T_{\rm dust,0} \in [15, 600]$ K, and the emissivity index and luminosity uniform priors, $\beta \in [1, 2.5]$ and $\log_{10}(L_{\rm dust}\ [L_\odot]) \in [4, 14]$. $L_{\rm dust}$ was integrated over rest-frame 1–1000μm, so that it includes the full emission of warm dust. The dust luminosity was tied through a Gaussian prior of width 0.3 dex in $\log_{10}(L_{\rm dust})$ to the luminosity absorbed by dust between 912 Å and

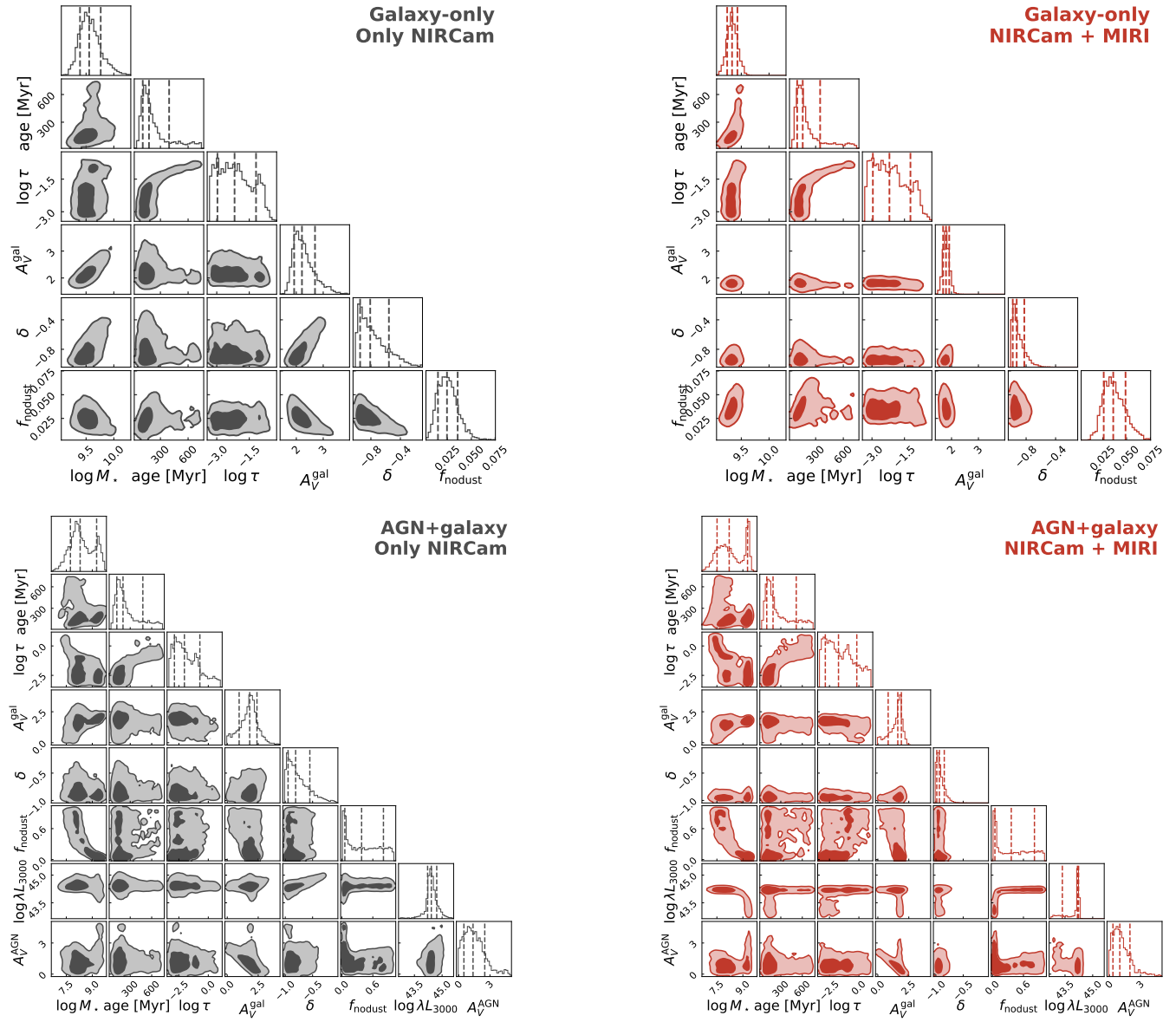


Figure H2. Posterior distributions of the galaxy-only (top) and AGN+galaxy (bottom) models of Ma et al. (2025), fitted to the NIRCam photometry only (left, grey) and to NIRCam and MIRI (right, red). Contours enclose 39% and 86% of the posterior mass (1σ and 2σ in two dimensions). Dashed lines in the 1D histograms mark the 16th, 50th and 84th percentiles (Table H2). $M_\star$ is the surviving stellar mass in $M_\odot$ and λL_{3000} is in ergs^{-1}, both in our normalisation. The age is measured from the onset of star formation, and τ is in Gyr. Axis ranges are the same in the two panels of each row.

3μm. The absorbed luminosity included the stellar light leaving the photoionised gas (uncovered and transmitted), the nebular continuum and lines and, in the cocoon families, the cocoon emission. The light absorbed by the gas itself is re-emitted as nebular emission and was therefore counted once. The PAH luminosity was tied to 0.045 L_{dust} with a Gaussian width of 0.3 dex (0.6 dex for the partially covering cocoon, since PAH emission is expected to be suppressed near AGN). These were soft priors, so the long-wavelength data could pull the solution away from strict energy balance.

Finally, intergalactic medium (IGM) absorption was set to follow Inoue et al. (2014) as implemented in EAZY.

I3 Accretion disc embedded in a dense cocoon

In the cocoon families, an accretion disc is surrounded by a dense, dust-free envelope of gas, whose emission we computed with a dedicated grid of CLOUDY (v25.00; Gunasekera et al. 2025) models. The intrinsic disc spectrum was the native, dust-free (transparent) accretion-disc component of the SKIRTOR models (Stalevski et al. 2012, 2016), a broken power law with $\lambda L_\lambda \propto \lambda^{1.2}$, λ^0, $\lambda^{-0.5}$ and λ^{-3} below 0.01, between 0.01 and 0.1, between 0.1 and 5, and above 5 μm, respectively. We did not use the torus component of SKIRTOR. The disc spectrum was extended to the extreme ultraviolet with a $T = 3.3 \times 10^5$ K blackbody joined at 8 nm (Zhang et al. 2026a), and to the X-rays with a coronal power law with photon index $\Gamma_X = 2.4$ and an exponential cut-off at 300 keV (Yang et al. 2020), joined at 0.1 keV and normalised through the optical-to-X-ray slope

$\alpha_{ox} = 0.3838\ \log_{10}[L_\nu(2\ \mathrm{keV})/L_\nu(2500\ \text{Å})] = -1.5$ (Tananbaum et al. 1979). The resulting spectrum was renormalised to the integrated luminosity of the SKIRTOR disc. In this continuum, $\approx 64\%$ of the luminosity is emitted below 912 Å ($\approx 14\%$ above 0.1 keV), and $\mathrm{BC}_{3000} = L_{\mathrm{AGN}}/\lambda L_{3000} \approx 9.6$.

The gas was modelled as a spherical, closed, dust-free shell fully surrounding the source, with constant hydrogen density $\log_{10}(n_{\mathrm{H}}\ [\mathrm{cm}^{-3}]) = 8, 9, 10, 11$ and 12, ionisation parameter $\log_{10}(U) = -4, -3, -2, -1$ and total hydrogen column $\log_{10}(N_{\mathrm{H}}\ [\mathrm{cm}^{-2}]) = 24.0, 24.5, 25.0, 25.5$, which spans the columns invoked by dense-envelope models of LRDs (Inayoshi & Maiolino 2025; Ji et al. 2025; Naidu et al. 2025). Each calculation was stopped at the requested $\log_{10}(N_{\mathrm{H}})$. The gas-phase metallicity was set equal to the stellar metallicity of each fit ($Z_{\mathrm{gas}} = 10^{-5}, 10^{-4}, 0.001, 0.002$ for `zem5`, `zem4`, `z001` and `z002`), with the Galactic-concordance abundance pattern of Nicholls et al. (2017). One node ($n_{\mathrm{H}} = 10^9$ cm^{-3}, $U = 10^{-1}$, $N_{\mathrm{H}} = 10^{25.5}$ cm^{-2}) did not pass our convergence checks at $Z_{\mathrm{gas}} = 10^{-5}$ and 10^{-4} and was excluded, leaving 79 nodes at these metallicities and 80 at the others. Each model was run at a reference bolometric luminosity of $10^{11}\ L_\odot$, with the corresponding ionising photon rate $Q(\mathrm{H})$ and the inner radius implied by $(Q(\mathrm{H}), U, n_{\mathrm{H}})$, so that the output is in absolute units. For each model we stored, per unit bolometric luminosity of the disc, the transmitted continuum F_{trans}, the outward diffuse continuum with the line emission removed (CLOUDY's outward diffuse continuum minus its outward-line contribution) F_{diffuse} and the emergent luminosity of each emission line F_{lines}. Lines were excluded from the saved diffuse continuum (CLOUDY's `set save line width suppress`), any residual outward-line contribution was subtracted explicitly, and duplicated and blended entries were removed from the line list, so that each line is counted exactly once.

In the fit, the cocoon emission was

$$L_\lambda = L_{\mathrm{AGN}}\left[(1-C)\,F_{\mathrm{inc}} + C\,(F_{\mathrm{trans}} + F_{\mathrm{diffuse}} + F_{\mathrm{lines}})\right], \qquad \text{(I1)}$$

where F_{inc} is the intrinsic disc spectrum and C the covering fraction, free in $[0, 1]$. The uncovered fraction thus reaches the observer as the unprocessed disc, while the covered fraction is replaced by the emission of the cocoon. The bolometric luminosity, $\log_{10}(L_{\mathrm{AGN}}\ [L_\odot])$, enters linearly and was solved for analytically at each likelihood evaluation. The cocoon node $(n_{\mathrm{H}}, U, N_{\mathrm{H}})$ was a discrete parameter without interpolation, and the lines were broadened with a free velocity dispersion $\sigma_v \in [200, 3000]$ km s^{-1}. The cocoon emission was attenuated by a foreground screen with the Calzetti et al. (2000) curve, a free colour excess and a free slope offset δ, as for the stellar populations. In the shared-screen families this screen was common to the stellar populations.

Limitations. CLOUDY solves the ionisation, thermal balance and non-LTE level populations of the gas self-consistently, including the $n = 2$ population of hydrogen that shapes the Balmer break and the Balmer absorption, at a cost that allows a grid of 80 nodes per metallicity to be fitted with nested sampling. It assumes spherical symmetry and computes the shell along the radial direction only, and it transfers the lines with escape probabilities. In the closed geometry adopted here, scattering opacities do not attenuate the incident continuum, and the frequency redistribution of scattered photons is not followed. The ionising continuum is fixed ($\alpha_{ox} = -1.5$, $\Gamma_X = 2.4$). Given the X-ray non-detection of QSO1, an X-ray-weaker continuum could change the thermal and ionisation structure of the gas. The electron-scattering optical depth computed by CLOUDY is $\tau_{\mathrm{es}} \lesssim 2.2$ for all nodes and $\lesssim 0.3$ for the nodes selected by the fits, because the gas beyond the thin ionised layer is only partially ionised ($x_e \lesssim 2\%$). Scattering by neutral hydrogen is instead large in the UV. For the node of the cocoon with the stellar-mass limit, CLOUDY gives a Rayleigh optical depth of 211 at 1300 Å, yet transmits 40% of the incident continuum at this wavelength. At 1 μm, both electron and Rayleigh scattering are negligible in this node ($\tau \lesssim 0.1$), and the continuum shape is set by the absorption and emission of the gas. These approximations affect the UV transmitted through the cocoon, the shape of the broad lines and the structure of optically thick gas. Monte Carlo radiative-transfer codes such as SIROCCO (Matthews et al. 2025; Sneppen et al. 2026) treat electron and resonance scattering in multi-dimensional geometries and should be used to test the regime selected by our fits.

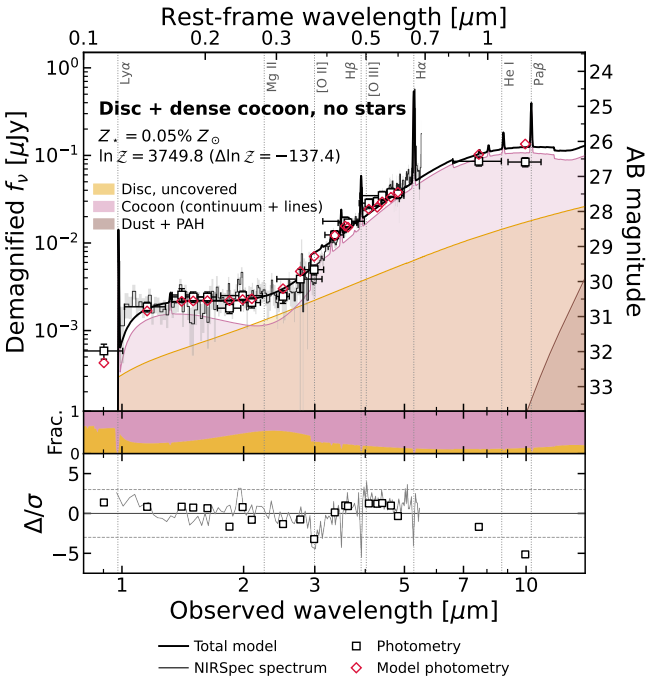


Figure I1. Maximum-likelihood solution of the model without stars (Appendix I4, `zem5`), in which an accretion disc is seen directly and through the dense cocoon. Panels as in Fig. 6, with $\Delta \ln(\mathcal{Z})$ relative to the highest-evidence model of Table I3. Without a separate UV component, the model misses the Balmer break (3σ in F300M) and over-predicts F1000W by 5σ.

I4 Test models

The last block of Tables I2 and I3 lists two models that test the components of the cocoon solution. In the model without stars, the stellar population was switched off by fixing its mass to $10^3\ \mathrm{M}_\odot$, its covering fraction to zero and its colour excess to zero, so that it contributes no measurable light. The disc then has to produce the UV continuum as well. The disc is seen both directly and through the cocoon, with a free covering fraction (Appendix I3). In the model with $E(B-V)_\star = 0$, the colour excess of the stellar population and of its nebular emission is fixed to zero, its mass is not limited, and the disc and cocoon keep their own screen. All other components, priors, data and sampler settings are those of the other families, so the evidences are directly comparable. Without stars, the cocoon solution (`zem5`) has $\log_{10}(L_{\mathrm{AGN}}\ [L_\odot]) = 10.71 \pm 0.06$ ($\approx 2 \times 10^{44}$ erg s^{-1}), a cocoon with $C = 0.49 \pm 0.04$, $n_{\mathrm{H}} = 10^{11}$ cm^{-3}, $U = 10^{-4}$ and $N_{\mathrm{H}} = 10^{25.5}$ cm^{-2}, lines with $\sigma_v \approx 910$ km s^{-1}, and a screen with $A_V = 1.6 \pm 0.1$ mag. Twice as much of the disc is covered as in

the solution with a young stellar population ($C \approx 0.22$), because the uncovered disc must now account for the UV alone.

I5 Fits to the individual images

The stacked photometry combines three epochs separated by up to ≈ 19 yr in the observed frame and depends on the relative magnifications of the lens model, while the spectrum samples Ima-B only. To test whether the model comparison of Section 4.3.2 depends on how the images are combined, we evaluated the posterior samples of the joint fits against the photometry of each image separately. For each of the six models in Table I1, we took the parameter sets sampled in the joint fit to the stacked photometry and the spectrum (up to 6000 per model, including the highest-likelihood points) and computed their synthetic photometry. We then compared it with the photometry of each image (Table B1), using the photometric uncertainties and the upper limits of that image and no spectrum. A free overall normalisation was solved for at each point, so that the test is sensitive only to the shape of the SED and not to the magnification. The best point of each model is the best solution for that image within the region of parameter space allowed by the spectrum. It is not a posterior of the photometry alone, which would explore a wider region.

For every model, the fitted normalisations reproduce the image ratios of the stack (1.77–1.86, 1.16–1.23 and 1.02–1.06 for Ima-A, B and C, against 1.87, 1.22 and 1), so the three images have the same SED shape and achromatic offsets. Without the magnification and inter-image terms of the stack, the uncertainties are smaller and the χ^2 values are larger than for the stack (Table I1). The largest residuals, however, are in the same bands for every model (F140M and F277W in Ima-A, F182M and F277W in Ima-B, F480M in Ima-C). They trace differences between the images, such as the varying broad-line equivalent widths and the residual contamination of Ima-B, rather than differences between the models, and do not affect their ranking.

In each image the ranking is the same as for the stack. The best solution with a massive stellar population fits better than the cocoon with the stellar-mass limit by $\Delta\chi^2 = 107$, 62 and 31 for Ima-A, B and C (13 for the stack). The cocoon over-predicts F1000W by 7.2, 8.8 and 4.6σ, while the stellar solutions reproduce it within $\approx 1\sigma$ in Ima-A and Ima-C. Without the MIRI bands, the difference drops to $\Delta\chi^2 = 51$, -6 and 9. The NIRCam photometry of Ima-B and Ima-C alone therefore does not separate the two classes, and the NIRCam-only cocoon fits predict F1000W fluxes 5–15σ above the observed ones. In Ima-B all models over-predict F1000W by 3–5σ, as expected from its lower MIRI-to-NIRCam ratio (Section 4.1). The cocoon with $E(B-V)_\star = 0$ behaves as the cocoon with the stellar-mass limit, and the model without stars gives the poorest fits in every image.

I6 Likelihood and sampling

The likelihood combined the photometry and the NIRSpec spectrum, which was rebinned to three pixels per resolution element and compared with models convolved to the instrumental resolution, without masking the emission lines. A fractional error floor (jitter) of 5% was added to the spectrum, the same for all families. For every combination of model family and stellar metallicity we ran the nested sampler Nautilus with 800 live points, a target effective sample size of 4000, a live-evidence fraction $f_{\rm live} = 0.01$ and at most 4×10^6 likelihood calls. Priors were uniform over the ranges above and over the allowed nodes for discrete parameters. The sampler returned the Bayesian evidence $\ln(\mathcal{Z})$ and posterior samples for each run.

All runs completed the exploration phase ($f_{\rm live} < 0.01$). The cocoon with the stellar-mass limit was run with the same settings, except for a lower target effective sample size. Figure I2 shows the posteriors of the four solutions in Fig. 6. The formal statistical uncertainty on $\ln(\mathcal{Z})$ returned by the sampler ($\lesssim 0.2$) does not include the run-to-run scatter. The NIRSpec spectrum was flux-calibrated with a smooth polynomial derived from the same photometry (Appendix C), whose uncertainty was propagated pixel by pixel. The covariance this introduces between spectral pixels and between the spectrum and the photometry is not included in the likelihood. We therefore regard differences of $\Delta\ln(\mathcal{Z}) \sim 100$ between classes as robust, and differences of $\Delta\ln(\mathcal{Z}) \sim 10$–$30$, such as those between the best stellar and cocoon solutions ($\simeq 13$) and between these and the cocoon with the stellar-mass limit ($\simeq 20$–33), as model-dependent rather than decisive, since they may be affected by spectral covariance, discrete-grid sampling and run-to-run variance. The latter difference is supported by the MIRI and emission-line residuals (Section 5.2). Several solutions sit at the edge of a grid or prior: the slope of the attenuation curve ($\delta \simeq -1$), the column of the cocoon in the solution with the stellar-mass limit ($N_{\rm H} = 10^{25.5}$ cm^{-2}), and, in the dense-gas and capped cocoon solutions, the photoionised gas of the UV-emitting population ($n_{\rm H} = 10^6$ cm^{-3} and $U = 10^{-1}$, the upper limits for ordinary-density gas).

This paper has been typeset from a TEX/LATEX file prepared by the author.

Table I1. χ^2 of the best solution of each model for the photometry of the individual images and of the stack, without the spectrum and with a free normalisation (Appendix I5), using all 21 detected bands and the upper limits ("all") or excluding F770W and F1000W (19 bands, "no MIRI"). The stack column uses the uncertainties of the stacked photometry. The lowest value of each column is in bold.

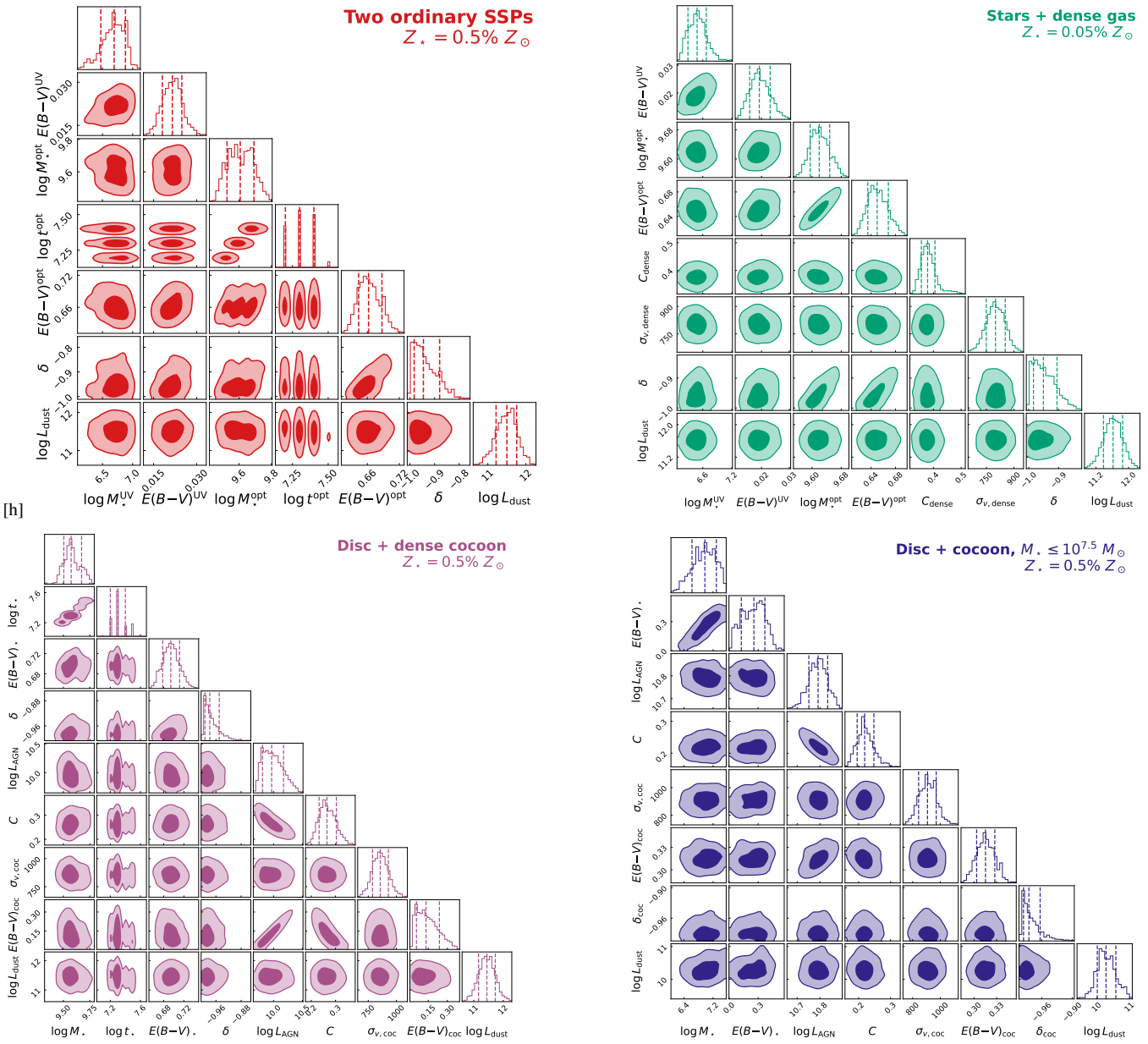
	Ima-A		Ima-B		Ima-C		Stack	
Model	all	no MIRI	all	no MIRI	all	no MIRI	all	no MIRI
`2ssp_nodense_independent` (`zem4`)	**95.1**	94.2	182.6	165.7	69.3	68.5	11.7	11.5
`normal_dense_independent` (`zem5`)	95.3	**91.9**	171.5	161.3	**62.5**	**60.1**	**10.9**	**10.5**
`normal_accretion_cocoon_independent` (`zem4`)	121.2	117.7	**169.3**	135.8	65.5	64.7	13.9	13.3
`accretion_cocoon_independent`, $M_\star \leq 10^{7.5}$ M$_\odot$ (`zem4`)	202.2	143.0	231.2	129.9	94.0	69.4	24.3	14.3
`accretion_cocoon_independent`, $E(B-V)_\star = 0$ (`zem4`)	196.1	145.6	253.5	142.6	92.6	68.5	24.0	15.4
`accretion_cocoon_only` (`zem5`)	319.5	270.2	240.2	**111.7**	116.4	70.6	33.9	19.9

Table I2. Model families fitted to QSO1. The family with $M_\star \leq 10^{7.5}$ M$_\odot$ is the cocoon fitted with the stellar mass limited to the upper limit on the host stellar mass. Every family except the one without stars contains a young, ordinary-density BPASS population for the UV continuum, with its own CLOUDY nebular emission and covering fraction. The second column gives the component added for the red optical continuum. In the highest-evidence unconstrained cocoon this role is taken by the stellar population, and the disc produces the UV (Section 4.3.2). "Independent" attenuation gives each component its own colour excess, "shared screen" places all components behind one foreground screen while "single screen" is for families with one single component. Each family was fitted at stellar metallicities of 0.05, 0.5, 5 and 10% $Z_\odot$ (`zem5`, `zem4`, `z001`, `z002`). $N_{\rm par}$ is the number of sampled parameters. In the cocoon families the AGN luminosity is solved for analytically and is not counted. The last block lists the test models of Appendix I4. For the model without stars, $N_{\rm par}$ counts only the parameters that affect the model.

Family	Red-continuum component	Attenuation	$N_{\rm par}$
`2ssp_nodense_independent`	ordinary-density SSP ($t \geq 10$ Myr)	independent	15
`normal_dense_independent`	dense-gas SSP	independent	16
`normal_dense_screen`	dense-gas SSP	shared screen	15
`normal_accretion_cocoon_independent`	accretion disc + dense cocoon	independent	15
`normal_accretion_cocoon_screen`	accretion disc + dense cocoon	shared screen	13
`accretion_cocoon_independent`, $M_\star \leq 10^{7.5}$ M$_\odot$	accretion disc + dense cocoon	independent	15
`accretion_cocoon_independent`, $E(B-V)_\star = 0$	accretion disc + dense cocoon	independent	13
`accretion_cocoon_only`	disc + cocoon, no stars	single screen	9

Table I3. Bayesian evidence, $\ln(\mathcal{Z})$, of every family–metallicity combination fitted to QSO1, with $\Delta\ln(\mathcal{Z})$ relative to the highest-evidence model (bold) in parentheses. The row with $M_\star \leq 10^{7.5}$ M$_\odot$ is the cocoon fitted with the stellar mass limited to the upper limit on the host stellar mass. The last block lists the cocoon with an unattenuated stellar population and no mass limit and the model without stars.

Family	`zem5` (0.05% $Z_\odot$)	`zem4` (0.5% $Z_\odot$)	`z001` (5% $Z_\odot$)	`z002` (10% $Z_\odot$)
`2ssp_nodense_independent`	3739.1 (−148.1)	3747.4 (−139.8)	3721.3 (−165.9)	3705.2 (−182.0)
`normal_dense_independent`	3874.5 (−12.7)	3858.2 (−29.0)	3866.6 (−20.6)	3857.1 (−30.1)
`normal_dense_screen`	3600.3 (−286.9)	3776.9 (−110.3)	3767.0 (−120.1)	3724.1 (−163.1)
`normal_accretion_cocoon_independent`	3873.4 (−13.8)	**3887.2 (0)**	3875.0 (−12.2)	3833.0 (−54.2)
`normal_accretion_cocoon_screen`	3776.4 (−110.8)	3769.4 (−117.8)	3750.3 (−136.9)	3738.7 (−148.5)
`accretion_cocoon_independent`, $M_\star \leq 10^{7.5}$ M$_\odot$	3853.2 (−34.0)	3854.4 (−32.8)	3840.2 (−46.9)	3833.4 (−53.8)
`accretion_cocoon_independent`, $E(B-V)_\star = 0$	3848.5 (−38.7)	3850.9 (−36.3)	3839.3 (−47.9)	3832.2 (−55.0)
`accretion_cocoon_only`	3749.8 (−137.4)	3731.8 (−155.4)	3706.8 (−180.4)	3693.2 (−194.0)



[h]

Figure I2. Posterior distributions of the main parameters of the four solutions in Fig. 6: two ordinary-density populations (`zem4`, top left), stellar populations with dense gas (`zem5`, top right), the accretion disc in a dense cocoon (`zem4`, bottom left) and the same model with $M_\star \leq 10^{7.5}$ $M_\odot$ (`zem4`, bottom right). Contours enclose 39% and 86% of the posterior, and dashed lines mark the 16th, 50th and 84th percentiles. Stellar masses are formed masses, $\log_{10}(M_\star\ [M_\odot])$, and ages $\log_{10}(t\ [\mathrm{yr}])$ on the 0.1 dex BPASS grid. Luminosities are $\log_{10}(L\ [L_\odot])$ and velocity dispersions in km s^{-1}. "UV" and "opt." denote the components dominating the rest-frame UV and optical continua. In the unconstrained cocoon, $M_\star$, $t_\star$ and $E(B-V)_\star$ refer to the stellar population that produces the optical continuum, and in the cocoon with the mass limit to the one that produces the UV. The subscript "coc" refers to the attenuation of the cocoon. In the dense-gas model the optical population has $\log_{10}(t\ [\mathrm{yr}]) = 7.2$ in more than 99.9% of the posterior and its age is not shown.